POLITECNICO DI MILANO

Doctoral Program in Physics - XXIX cycle

Nanostructured WO₃ Films for Photoelectrochemical Water-Splitting

PhD Candidate: **Alessandro Mezzetti**

Supervisor: **Dr. Fabio Di Fonzo**

Tutor: **Prof. Guglielmo Lanzani**

PhD Coordinator: **Prof.ssa Paola Taroni**

Ti voglio bene, mamma

Abstract

This doctoral research focuses on photoelectrochemical water-splitting devices for the solar hydrogen production. In photoelectrochemical water-splitting, the chemical energy required to cleave the water molecules is provided by solar photons, that are absorbed and converted by the photoelectrodes. Photoelectrodes are carefully designed semiconducting architectures that collect incoming photons and generate separated charges with the correct energy amount to drive the water oxidation and reduction reactions. Thermodynamic constraints impose an energy gap of at least 1.23 eV – experimentally increased due to overpotentials – and a proper alignment with respect of the reduction and oxidation potential of water. The process can be performed by a single photoelectrode, but in terms of optimization it is more reasonable to separate the two half-reactions and ascribe them to their specific device, photoanode for the oxygen evolution and photocathode for the hydrogen evolution. In this work is presented the fabrication, characterization and optimization of photoelectrodes made with WO_3 films: quasi-1D hyperbranched WO_3 photoanodes and amorphous WO_3 hole selective layer for hybrid organic photocathodes.

Quasi-1D hyperbranched WO_3 photoanodes are fabricated via pulsed laser deposition through a self-assembly process from the gas phase, obtaining arrays of tree-like nanostructures with strong directional growth, high crystallinity and improved long-range order. The photoelectrochemical characterization of these photoanodes exhibits an onset potential as low as 0.4 V_{RHE} and saturation current densities up to 1.85 mA·cm^{-2} at 0.8 V_{RHE}. While the saturation photocurrent values are similar to the state-of-the-art values for WO_3 photoanodes, both the onset and

saturation voltages are significantly lower than any other reported values. Further investigation attributes these low voltage values to the efficient charge generation, charge injection and charge transport. The hyperbranched morphology absorbs and converts incoming photons, up to wavelengths close to the WO_3 band-edge cutoff. Thanks to the nano-tree structure, holes have to travel only through the width of the crystallites to reach the electrolyte, a distance significantly lower than the hole recombination length in WO_3. At the same time, electrons have to travel along the whole nano-tree structure, but are facilitated in the process by the strong directional growth and high crystallinity, that provide few interfacial boundaries and lattice defects where the electrons might undergo trapping or recombination events. These effects are confirmed by comparing the characterization of the optimized hyperbranched morphology – labelled as HYP – with a similar hierarchical nano-tree structure – labelled as HIE – that lacks the improved long-range order and strong crystalline directional growth.

Hybrid organic photoelectrochemical devices exploit the use of organic semiconductors as photoactive materials, as already demonstrated by organic photovoltaics. To achieve high performances, the organic semiconductor needs to be coupled with selective contacts that efficiently extract the charges. Finding the correct material for the selective contacts is currently one of the main research topic in the field, since both the optoelectronic requirements of organic photovoltaics as well as the electrochemical constraints of standard photoelectrochemical devices need to be satisfied. Correct energetic alignment is fundamental to separate the photogenerated charges, as well as the capability to selectively inject only the correct type of charge to reduce recombination and parasitic currents. Furthermore, selective contacts need to be transparent to avoid shadowing the absorption of the organic photoactive material and must display strong electrochemical stability in order to perform durably in the electrolytic

environment. TiO_2 satisfies these requirements and is the materials of choice to cover the role of the electron selective layer. Conversely, finding the appropriate material for the hole selective layer have been proven to be much less straightforward. Based on previous hybrid organic photoelectrochemical architectures that use P3HT:PCBM blend as the photoactive material and an amorphous TiO_2 film as the electron selective layer, an amorphous WO_3 film deposited via reactive magnetron sputtering is employed as the hole selective layer in order to exploit of the strong chemical stability of WO_3 and thus obtain longer lifetimes while retaining adequate operational performances. The resulting photocathode achieves a photocurrent of 2.48 $mA \cdot cm^{-2}$ at 0 V_{RHE}, an onset potential of 0.56 V_{RHE} and a state-of-the-art operational activity of more than 10 hours.

Estratto

Questo dottorato di ricerca si concentra sui dispositivi per l'elettrolisi fotoelettrochimica dell'acqua finalizzati alla produzione di idrogeno tramite energia solare. Nell'elettrolisi fotoelettrochimica dell'acqua l'energia chimica richiesta per scindere le molecole d'acqua è fornita dai fotoni solari, che vengono assorbiti   e convertiti dai fotoelettrodi. I fotoelettrodi sono architetture semiconduttive attentamente sviluppate che raccolgono i fotoni in arrivo e generano una separazione di portatori di carica con energia sufficiente a pilotare le reazioni di ossidazione e di riduzione dell'acqua. I limiti termodinamici impongono un salto energetico minimo di 1.23 eV – sperimentalmente aumentato a causa dei sovrapotenziali – e un adeguato allineamento rispetto ai potenziali di ossidazione e di riduzione dell'acqua. Il processo può essere svolto da un singolo fotoelettrodo, ma in termini di ottimizzazione è più sensato separare le due mezze reazioni e assegnare ciascuna al suo specifico dispositivo, il fotoanodo per lo sviluppo di ossigeno e il fotocatodo per lo sviluppo di idrogeno. In questo lavoro viene discussa la fabbricazione, la caratterizzazione e l'ottimizzazione di fotoelettrodi fabbricati con film di WO_3: fotoanodi quasi-1D iper-ramificati di WO_3 e WO_3 amorfo come strato selettivo per le buche in fotocatodi ibrido-organici.

I fotoanodi quasi-1D iper-ramificati di WO_3 sono fabbricati con deposizione a laser pulsate tramite un processo di auto-assemblaggio da fase gassosa, ottenendo matrici di nanostrutture ad albero con una forte crescita direzionale, un'alta cristallinità e un elevato ordinamento sulla lunga distanza. La caratterizzazione fotoelettrochimica di questi fotoanodi mostra un potenziale di attacco pari a 0.4 V_{RHE} e una densità di corrente di saturazione di 1.85 mA·cm^{-2} a 0.8 V_{RHE}. Mentre i

valori della fotocorrente di saturazione sono comparabili con quelli dello stato dell'arte per i fotoanodi di WO_3, sia il potenziale di attacco che quello di saturazione sono significativamente più bassi di ogni altro valore riportato. Ulteriori indagini attribuiscono questi bassi valori di voltaggio a una efficiente generazione, iniezione e trasporto di carica. La morfologia iper-ramificata assorbe e converte i fotoni in arrivo, fino alle lunghezze d'onda vicino al limite massimo di banda del WO_3. Grazie alla nanostruttura ad albero, le buche devono viaggiare unicamente lungo la larghezza dei cristalliti per raggiungere l'elettrolita, una distanza significativamente più bassa rispetto alla lunghezza di ricombinazione per le buche nel WO_3. Al contempo gli elettroni devono viaggiare lungo tutta la nanostruttura ad albero, ma sono facilitate nel processo dalla forte crescita direzionale e dall'altra cristallinità che forniscono un numero ridotto di margini interfacciali e di difetti reticolari dove gli elettroni potrebbero subire eventi di ricombinazione o intrappolamento. Questi effetti sono confermati dalla comparazione fra la caratterizzazione dell'ottimizzata morfologia iper-ramificata – identificata come HYP – e quella di una simile nanostruttura gerarchica ad albero – identificata come HIE – a cui mancano l'elevato ordinamento sulla lunga distanza e la forte crescita cristallina direzionale.

I dispositivi fotoelettrochimici ibrido-organici utilizzano semiconduttori organici in qualità di materiali fotoattivi, come già dimostrato dal fotovoltaico organico. Per ottenere elevate prestazioni, i semiconduttori organici devono essere accoppiati con dei contatti selettivi che estraggono efficientemente le cariche. Trovare il materiale corretto per i contatti selettivi è attualmente uno dei principali argomenti di ricerca in quest'ambito, dal momento che devono essere soddisfatti sia i requisiti optoelettronici del fotovoltaico organico sia le limitazioni elettrochimiche dei dispositivi fotoelettrochimici tradizionali. Il corretto allineamento energetico è fondamentale per separare le cariche fotogenerate,

così come la capacità di iniettare selettivamente la corretta tipologia di portatore al fine di ridurre la ricombinazione e le correnti parassitarie. Inoltre i contatti selettivi devono essere trasparenti, per evitare di schermare l'assorbimento del materiale organico fotoattivo, e devono presentare un'elevata stabilità elettrochimica così da operare durevolmente nell'ambiente elettrolitico. Il TiO_2 soddisfa questi criteri ed è il materiale scelto per ricoprire il ruolo di strato selettivo per gli elettroni. Al contrario trovare il materiale adatto per lo strato selettivo per le buche si è dimostrato molto meno semplice. Basandosi su precedenti architetture di fotoelettrodi ibrido-organici che utilizzano una miscela di P3HT:PCBM come materiale fotoattivo e TiO_2 amorfo come strato selettivo per gli elettroni, un film di WO_3 amorfo depositato tramite magnetron sputtering reattivo è impiegato come strato selettivo per le buche al fine di sfruttarne l'elevata stabilità chimica e così ottenere una maggior durata del dispositivo mantenendo al contempo adeguate prestazioni operative. Il fotocatodo che ne risulta raggiunge una densità di fotocorrente pari a 2.48 $mA·cm^{-2}$ a 0 V_{RHE}, un potenziale di attacco di 0.56 V_{RHE} e un'attività operativa record di più di 10 ore.

Table of Contents

Chapter 1: Water-Splitting

1.1 Hydrogen Economy

Coined in 1970 by electrochemist John Bockris[1] and risen to global attention in the 2000s, hydrogen economy is a proposed economic system that employs hydrogen to deliver energy, acting both as a fuel for motive and stationary power, as well as a storable and transportable energy vector. The rationale behind the concept of a world-scale hydrogen economy relies on the unavoidable drawbacks of the current hydrocarbon economy. Burning hydrocarbon fuels releases several pollutants in the environment like fine particulate matter and emits carbon dioxide, currently one of the most dangerous greenhouse gases that is contributing to global warming. Furthermore, the availability of hydrocarbon resources like coal and petroleum is inherently limited and in constant decrease, whereas its demand is raising due to the rapid economic growth of countries like China and India. Hydrogen can be an efficient and environmentally clean source of energy, especially for end-user transport applications, thanks to its high-energy density and lack of pollutants released upon utilization (Figure 1.1). Both the combustion and the electrochemical conversion of hydrogen – respectively from internal combustion engine and from hydrogen fuel cell operation – release only water as the byproduct of its reaction to produce energy.
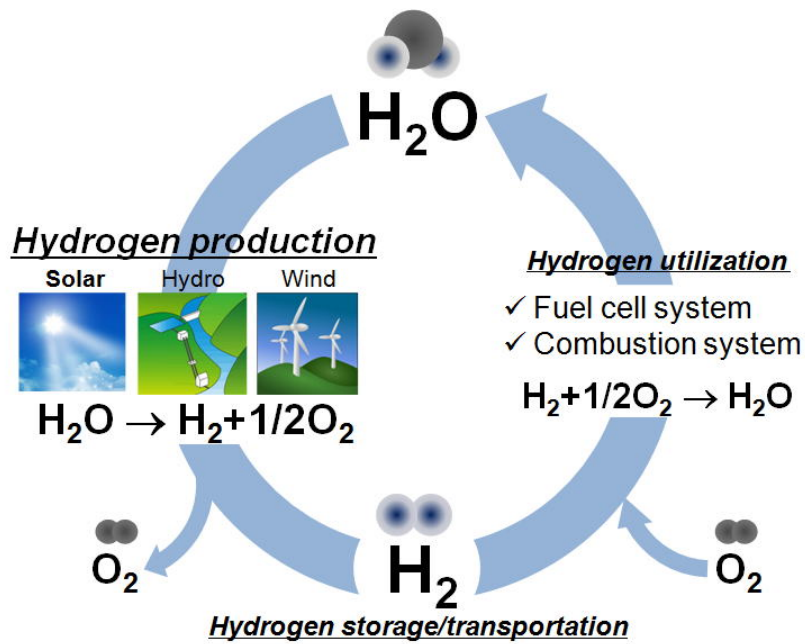
Figure 1.1 – Schematic of the closed cycle of the hydrogen economy. It starts with water, that is split into hydrogen and oxygen using a renewable energy source. The produced hydrogen can be stored and/or transported as traditional energy vector. Later, hydrogen is employed to power a fuel cell or a combustion system, where it releases energy in the process of combining with oxygen to form water.

Despite the good premise, 96% of the global hydrogen production[2] comes from processes that employ fossil fuels – as for the dominant steam reforming or Kvaerner CB&H methods – and its use is split between the synthesis of ammonia via the Haber process and the conversion of heavy petroleum into lighter fractions via hydrocracking. The remaining 4% of global hydrogen is produced with electrolysis, powered by electrical energy that is generated mostly via conventional methods. In order to completely cut the dependencies of hydrogen production from the hydrocarbon energy market, a renewable and sustainable process must be found.

1.2 Solar Water-Splitting

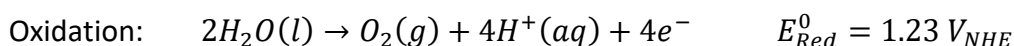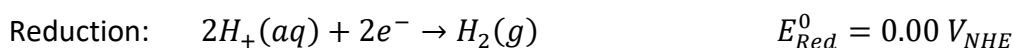Every year the sun irradiates Earth for a grand total of $3 \cdot 10^{24}$ J, about ten thousand times more energy than the current global consumption, thus making solar energy the most abundant and available energy resource available on the planet. While conversion of solar energy into electricity through photovoltaics has been under intense research in the past decades and has now reached such efficiencies as to become a serious alternative to fossil fuels, there is still no established technology for the production of a transportable and storable energy vector from renewable and sustainable sources, the necessary step for a successful future transition towards a hydrocarbon-free energetic economy.

The production of hydrogen through solar energy stands as a promising answer to the aforementioned request, with both consolidated and in-development technologies. The concept behind the process is to harness the energy of the incoming solar photons to drive the chemical reaction that splits water into its components, oxygen and hydrogen. This two-step process – solar energy capture and chemical cleaving of water – can be performed at separated stages or in single device. In the first case, a standard photovoltaic device provides the conversion from solar energy into electric power that is used by a separated electrolyser to drive the water-splitting reactions. On the other hand, single-device technologies – like photocatalytic or photoelectrochemical water-splitting – are designed to directly produce hydrogen upon solar illumination, exploiting the semiconducting and catalytic properties of the materials employed.

1.2.1 Electrolysis of Water

The process of water electrolysis dates back to the early 1800, when William Nicholson and Anthony Carlisle first produced oxygen and hydrogen using two electrodes immersed in water, powered by direct current from an external energy supply. To this day, the technology behind water-splitting stands as simple as that: two electrodes or plates (usually made from an inert, catalytic metal such as gold, platinum or iridium) are connected to an external direct current electric source and placed into water. As electric current flows, hydrogen appears at the cathode where electrons are injected into water and oxygen appears at the anode where electrons are given to the electrode thus completing the circuit. The whole process comprises a cathodic reduction reaction and an anodic oxidation reaction, respectively occurring at 0 V and 1.23 V versus the normal hydrogen electrode (NHE) potential reference:

Reduction: $2H_+(aq) + 2e^- \rightarrow H_2(g)$ $E^0_{Red} = 0.00\ V_{NHE}$

Oxidation: $2H_2O(l) \rightarrow O_2(g) + 4H^+(aq) + 4e^-$ $E^0_{Red} = 1.23\ V_{NHE}$

Combining the two half-reactions gives the overall water-splitting reaction:

Overall reaction: $2H_2O(l) \rightarrow 2H_2(g) + O_2(g)$
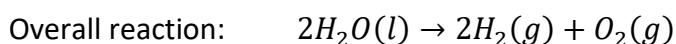
This reaction is not thermodynamically favorable and thus the reaction enthalpy is positive and equal to 237.2 kJ/mol of electric energy plus 48.6 kJ/mol of heat energy, calculated at standard conditions of temperature and pressure. Assuming the required amount of heat energy is externally supplied to the reaction, the corresponding reversible voltage is equal to 1.23 V. When both the electric and the heat contributions need to be provided, the voltage needed is equal to 1.48 V and is defined as the thermoneutral voltage.

When all the electrons transferred participate only in the water-splitting reaction and the reaction thus perform under full Faradaic efficiency, the amount of hydrogen generated is twice the amount of oxygen and both are proportional to the total electrical current flowing in the system. However, real systems always suffer from nonidealities that increase the thermodynamic potential required for the process, overpotentials that arise from activation barriers, concentration effects and potential drops due to resistances (Figure 1.2). Additionally, the Faradaic efficiency of the reaction can be lower than 100% as other ionic specimen present in the water solution can undergo reactions competing with hydrogen and oxygen evolution.
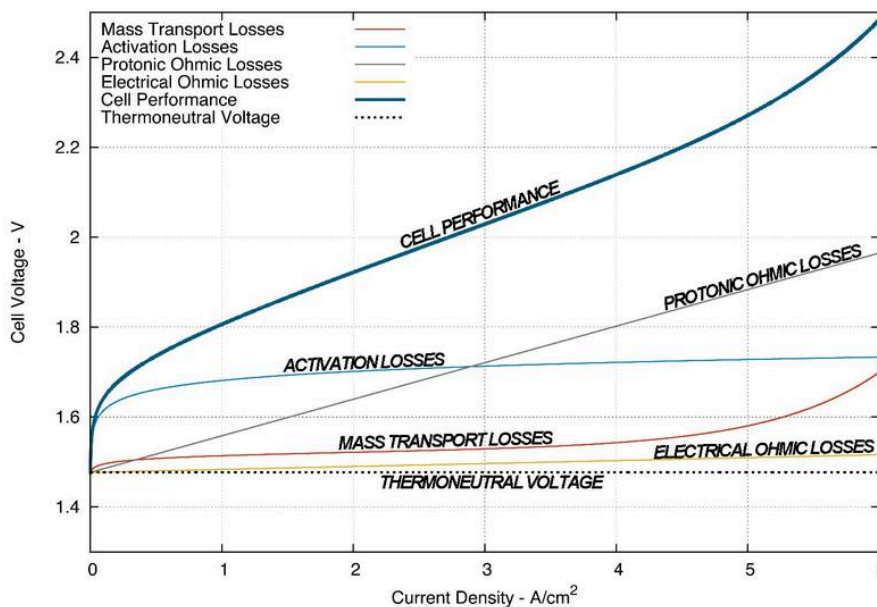
Figure 1.2 – Illustrative graph of the different nonidealities that affect the electrolysis of water, increasing the applied potential required to extract a given amount of current. The values on the graph are associated with the simulated operation of a PEM electrolyser.

Pure, de-ionized water has low autoionization and low conductivity at room temperature ($K_w = 10^{-14}$ and $0.055 \, \mu S \cdot cm^{-1}$) and thus behaves as a good insulator. This results in a very slow electrolysis process, limited by the overall conductivity unless a very large potential is provided in order to increase the autoionization. To solve this issue, a water-soluble electrolyte can be added to

considerably increase the overall solution conductivity. However, it is important to select an electrolyte that dissociates into anions and cations not in competition with the hydroxide and hydrogen ions, in order to avoid the establishment of parasitic reactions that would hinder the production of hydrogen and oxygen: an electrolyte anion with a greater standard electrode potential than hydroxide and an electrolyte cation with a lesser standard electrode potential than a hydrogen. Using an acid as the electrolyte ensures that there is no competition for the cathodic reaction as the dissolved cation is still H⁺ and leaves the optimization to the selection of a suitable anion. Sulfuric acid (H$_2$SO$_4$) is commonly used as electrolyte for water-splitting as its dissociated sulfate anion (SO_4^{2-}) oxidizes into peroxydisulfate ($S_2O_4^{2-}$) at a standard NHE potential of 2.05 V, much lower than the water oxidation potential of 1.23 V. Furthermore, a concentrated electrolyte provides enough charge-carriers in the solution to reduce the effects of concentration overpotential. In this case, the potential increment is caused by a different concentration of charge-carriers between the solution and the surface of the electrode that occurs when the electrochemical reaction is rapid or the ion diffusion rates are slow.

Since potential drops due to resistance can be severely limited with an optimized design of the electrochemical cell, the largest contribution to the nonideality of the real electrolysis process is the reaction overpotential. The oxidation of water to oxygen is a four-electron reaction and thus requires additional voltage to provide the correct activation energy and to enhance its kinetics. Using a suitable catalyst can help facilitate the reaction by reducing the activation energy of the process and iridium oxide is currently the state-of-the-art as a catalyst for the oxidation reaction. The much simpler two-electron reduction of water to hydrogen requires a less additional voltage and can be catalyzed with platinum for almost no overpotential or with other materials for a less effective reduction.

1.2.2 PV-Assisted Electrolysis

All types of electrolyser requires an external power source to function and, in order to keep the process sustainable and renewable, an adequate solution is to employ standard photovoltaic devices to provide the electrical energy needed. As of today, state-of-the-art photovoltaic devices have reached efficiencies in the range of 45%, whereas commercially available solar panel amount to 20%. Plenty of literature details both research and commercial development, but an in-depth study on recent photovoltaics is beyond the scope of this work. Still, for the sake of this explanation, the commercial efficiency value is taken as representative. For a system comprising an electrolyser powered by a solar panel, the overall efficiency is the product of the efficiency of each single component.
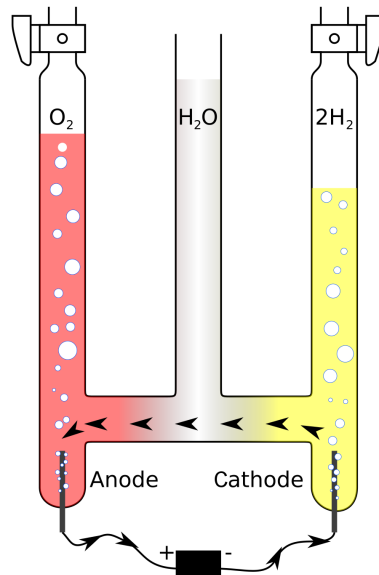

Figure 1.3 – Illustration of the Hofmann voltammeter and its basic working principle.

Modern electrolyser technology is roughly based on the concept of the Hofmann voltammeter (Figure 1.3), an electrochemical setup that dates back to 1866. The apparatus consists of three upright cylinders, connected at the bottom. The

cylinder in the middle is open on top and is designed for the intake of water and possible electrolytes, while the cylinders on the sides have a platinum electrode placed at the bottom and a gas collection system at the top. When the two platinum electrodes are connected to a source of electricity, electric current runs through Hofmann voltammeter and gaseous oxygen and hydrogen are formed at the anode and at the cathode respectively. The bubbles of each gas, generated in their respective confined cylinder, are collected with minimum mixing from the collection system at the top. Nowadays different types of electrolyser have been developed, each exploiting different materials and configurations to optimize the process efficiency and feasibility despite the ever-present limitations. The most commonly employed electrolysers are the alkaline water electrolyser and the polymer electrolyte membrane (PEM) electrolyser, with the possible technological variants of high-temperature electrolysis (HTE) or the high-pressure electrolysis (HPE). Regardless the pros and cons of each configuration, all these systems are grouped together by some key features: noble metals such as platinum and iridium oxide used as catalyst to improve the performance of the electrodes, a system lifetime above 10 years and a cell voltage efficiency of 52 – 69%, corresponding to a working potential of 1.75 – 2.40 V.

The resulting device for the production of hydrogen using a renewable energy source is a photovoltaic-assisted electrolyser, a series system where solar energy is converted into electricity by an array of solar panels and the electricity is driven through the catalytic electrodes to perform the complete water-splitting reaction. Using the average value of the quote efficiencies as the benchmark parameters for each respective technology, the described tandem system displays a maximum theoretical efficiency of 12%, calculated as the product of the photovoltaic efficiency times the electrolyser efficiency. Parasitic losses related to the wiring required for electrically connecting the two components are neglected for

simplicity reasons, but are still present nonetheless. These efficiency and lifetime numbers are kept as benchmark values when evaluating the feasibility of emerging technologies for hydrogen production via renewable sources. On the economic aspect, with an electricity cost of 0.063 $·kWh^{-1} and an electrolyser conversion efficiency around 70 kWh·kg^{-1} of hydrogen, modern electrolysers connected to the standard electric grid have an estimated production cost of 4 $·kg^{-1} of hydrogen. When the contribution of electricity via photovoltaic sources is taken into account, a lower cost of electricity can be achieved on the long run with adequate investments in the solar-powered infrastructure, resulting in slightly higher costs for the renewable production of energy and consequently of hydrogen.

1.2.3 Photocatalytic Water-Splitting

Photocatalytic water-splitting consists in producing hydrogen and oxygen from an aqueous solution, converting the incoming solar light into the chemical energy required to drive the redox reaction. A suitable semiconductor absorbs solar photons and photogenerates electron-hole pairs that separately reach the catalytic surface of the material and are used to perform the water oxidation and reduction reactions (Figure 1.4). Photocatalytic water-splitting was discovered in 1972 by Fujishima at el.[3] as they illuminated with strong solar light a transition metal oxide plate placed in an aqueous solution – that first time, TiO_2 – and noticed that it was developing gas bubbles on its surface. Once better investigated in later years, this phenomenon was called the Fujishima-Honda effect. To perform photocatalytic water-splitting, a given semiconductor needs to satisfy two mandatory electronic requirements: the energy gap between the conduction band and the valence band must be higher that the enthalpy of the reaction and the water-splitting redox potentials must be correctly aligned with the energy bands

of the semiconductor, with the conduction band positioned above the hydrogen evolution potential and the valence band positioned below the oxygen evolution potential. In this way, when the semiconductor absorbs an incoming photon, that energy is used to move an electron in the conduction band, leaving behind a hole in the valence band. Since the conduction band of the semiconductor is positioned above the hydrogen evolution potential, the promoted electron – also called photogenerated electron – is energetically allowed to participate in the water reduction process. The same discussion applies to the hole, generated in the valence band below the oxygen evolution potential and thus energetically allowed to participate in the water oxidation process.
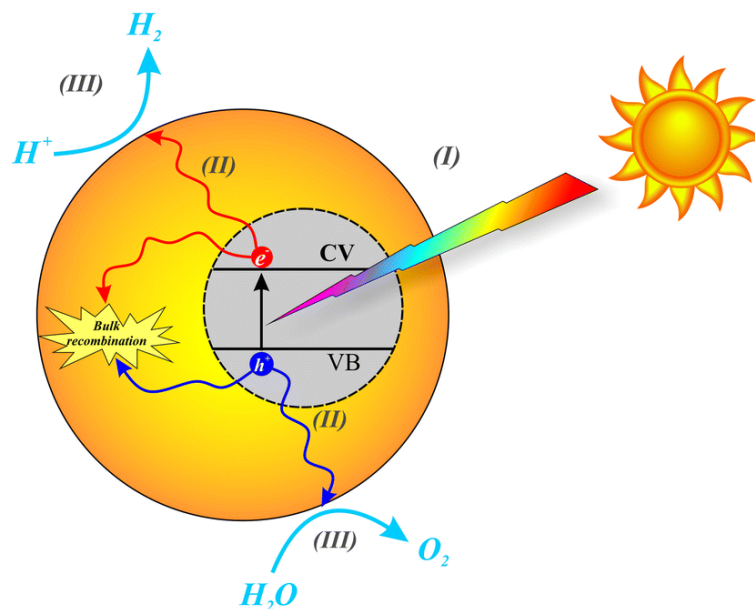

Figure 1.4 – Schematic of the fundamental mechanisms that occur in photocatalytic water-splitting: the semiconductor absorbs incident solar photons and photogenerates electron-hole pair (I); the photogenerated electrons and holes can migrate to the semiconductor surface or recombine in the material bulk (II); electrons on the surface can reduce protons to produce hydrogen and holes on the surface can oxidize water to produce oxygen (III).[4]

Furthermore, in order to improve the feasibility and efficiency of the photocatalytic water-splitting process, additional constraints are introduced. As the amount of oxygen and hydrogen evolved depends on the number of charges that contribute to the reactions, optical absorption should be maximized to

achieve strong photogeneration, using a semiconductor with a band-gap as narrow as possible. In the trade-off between thermodynamic activation and optical absorption, it is important to take into account the activation overpotentials due to the low kinetics of the process and the shape of the solar radiation spectrum, with a broad peak in the green-red visible spectral range. Altogether, the ideal range of optical band-gap for a single semiconductor is between 1.6 – 2.0 eV, always assuming a proper alignment of the energy bands. An additional requirement for durable performances is tied to the chemical stability of the semiconductor in the aqueous environment where the reaction takes place. If the material presents reduction or oxidation states within the energy gap of water-splitting, these reactions might compete with oxygen and hydrogen evolution, not only reducing the overall device efficiency but also deteriorating the material over time. Since its low conductivity is detrimental for the reaction kinetics, pure water is frequently substituted with an alkaline or acidic electrolyte with additional anions and cations dissolved, which might cause concurrent reactions with the photocatalytic materials and thus implies a careful choice based on compatibility between all the substances involved.

In an actual photocatalytic water-splitting system the selected semiconductor is mainly fabricated as a nanopowder, which is then dispersed in the electrolytic solution. The nanometric size of the particles is exploited to minimize the distance travelled by the photogenerated charges within the material and thus improve the transport efficiency towards the interfaces. On the other hand, strong spatial confinement is responsible for higher recombination rates. Efficient charge extraction is a key aspect to obtain good performances and can be achieved by sensitizing the nanoparticle surface with specific catalytic materials. These materials harvest the charges at the interfaces and reduce the activation energy of the water-splitting half-reactions; currently, the best-performing catalyst for

oxygen evolution is iridium oxide and for hydrogen evolution is platinum. In standard systems with a single material, the semiconductor used to fabricate the nanoparticles is either p-type or n-type in terms of relative position of the Fermi level within the energy gap, resulting in a band-bending at the electrolytic interface that favors the injection respectively of electrons or holes; the opposing charges instead feel a potential barrier and are driven towards the material bulk, where recombination occurs with a higher rate. Since a single photocatalytic material cannot develop a built-in potential that can efficiently separate and inject both holes and electrons, heterostructures with two or more materials have been developed to overcome this limitation (Figure 1.5). Depending on the relative position and amplitude of the semiconductors band-gaps, different configurations and architectures are possible, using full or partial core-shell nanostructures, functionalization of the surface or interfacial ligands between two nanoparticles of different materials.
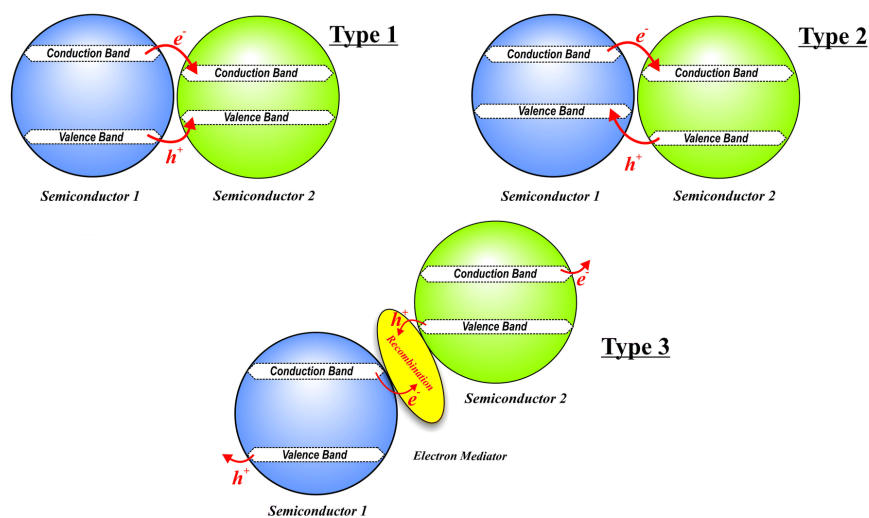

Figure 1.5 – Schematic of different types of heterostructures for photocatalytic water-splitting, defined by the relative position of the conduction and valence band of the two comprising materials.[4]

On a technological and economical point of view, photocatalytic water-splitting systems benefit from the rather simplistic configuration and fabrication of its

components: nanopowders can be produced in large quantities using wet processes with contained costs and more complex structures or specific functionalization can be performed likewise in solution, with the reagents cost being the main expense contribution. As the nanopowders are simply dispersed in the electrolytic solution, there is no need for specific infrastructures to support the system, that just need solar irradiation to perform the water-splitting process and the oxygen and hydrogen gas production. On the other hand, since the production of both gasses occurs on the same nanoparticle surface, there is currently no actual way to isolate hydrogen from hydrogen other than a gas separator device to be put downline of the photocatalytic system. A possible solution is to design a photocatalytic system that only performs a single reaction of water-splitting, specifically only the hydrogen evolution process. However, the other half reaction needed to balance out the charge exchange in alternative to oxygen evolution would be an oxidation reaction involving a sacrificial agent to be added in the electrolyte. The resulting electrolytic solution would undergo a gradual consumption of the sacrificial agent and a concurring increase in the pH since the hydrogen ions are consumed by the water reduction, thus achieving single gas production at the expense of a more complex and chemically unstable system. Additionally, as the nanopowder are dispersed in aqueous solution without any wiring or electrical connection, the process can only work unbiased and no external contribution might be employed to boost the performances, the whole optimization process having to focus on the material choice and on possible sensitization or functionalization. Since the amount of charges involved in the catalytic process cannot be quantitatively measured, the benchmark efficiency parameter is related to the amount of hydrogen generated, converted into an energy value via the enthalpy of the reverse reaction and divided by the input power of the illuminating solar light.

1.2.4 Photoelectrochemical Water-Splitting

Photoelectrochemical water-splitting shares all the requirements previously discussed for photocatalytic water-splitting, but differs in terms of operative architecture, having its own optimization strategies and expedients to improve the overall performances of the working device. A system for photoelectrochemical water-splitting is similar in design to a standard electrolysis system as it comprises two electrodes immersed in an electrolytic aqueous solution; the essential difference resides in the photoactive behavior of the electrodes, that are semiconducting structures with catalytic surfaces, designed to harvest solar energy and convert it into chemical energy to drive the water-splitting reactions without the need of an external power source (Figure 1.6).
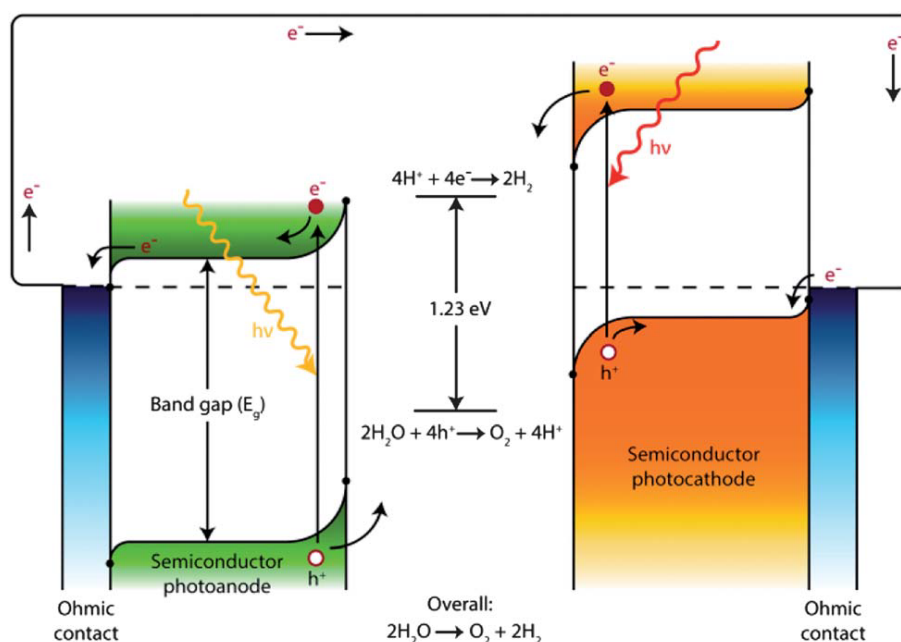

Figure 1.6 – Schematic of the band diagram for a photocathode and photoanode system, showing the phenomena of photon absorption, charge separation due to the semiconductors band-bending, as well as the hydrogen and oxygen evolution reactions occurring at the interfaces.[5]

There are three possible configurations for a photoelectrochemical water-splitting system: a photoanode coupled with a catalytic cathode, a photocathode couple with a catalytic anode and a photoanode coupled with a photocathode. Photoanodes are fabricated with n-type semiconductors and photocathodes are fabricated with p-type semiconductors, so that the built-in potential resulting from the band-bending can separate the charges and transport each carrier towards its designed interface. In the first two cases, the specified photoelectrode has to single-handedly satisfy the energetic requirements of the process, with the comprising semiconductor – or semiconducting heterostructure – having the correct level alignment for both photogenerated carriers: electrons in the conduction band above the hydrogen evolution potential and hole in the valence band below the oxygen evolution potential.
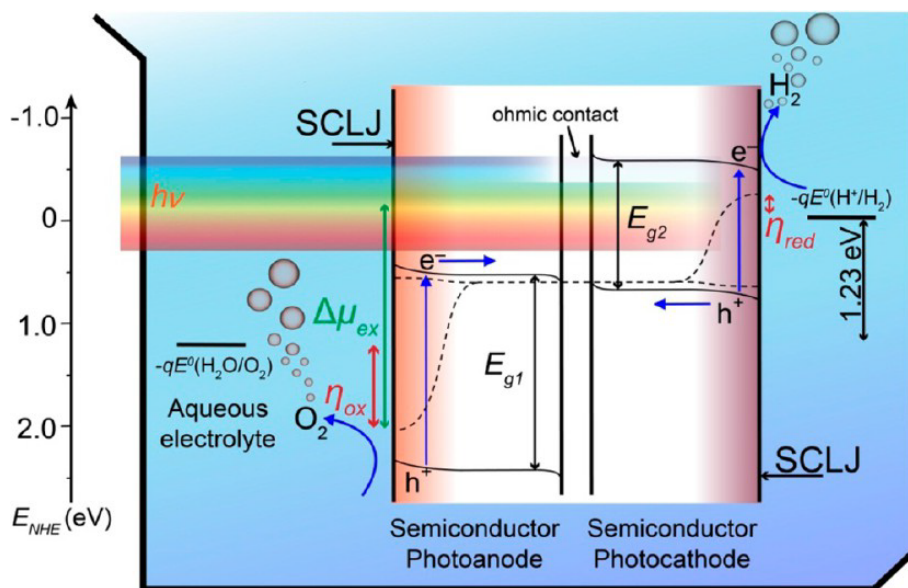

Figure 1.7 – Electron energy scheme for a PEC water-splitting system using a back-to-back tandem configuration with two absorbers. Photon absorption generated an electron–hole pair within the semiconductor that is separated by the space charge layer (indicated by the formation of two quasi-Fermi levels, broken lines) and thus generate a built-in potential. The combined photogenerated potential of the two stacked absorbers provides an increase in the available free energy $\Delta\mu_{ex}$. When the free energy available is greater than water splitting enthalpy of 1.23 eV (plus the anodic and cathodic overpotential losses, respectively η_{ox} and η_{red}), evolution of hydrogen and oxygen can occur at the semiconductor-liquid junction (SCLJ).[6]

In the last configuration (Figure 1.7) both the electrodes are photoactive components and the energetic requirements of the two half-reactions can be decoupled and each assigned to the suitable photoelectrode, relaxing the optimization constraints on the employed semiconducting structures. The valence band of the photoanode must be lower than the water oxidation potential and the conduction band of the photocathode must be higher than the water reduction potential, with the requirement for a minimum band-gap energy of 1.23 eV no longer necessary, thus allowing for semiconductors with higher optical absorption to be successfully used. Since both photoelectrodes have to absorb solar energy in order to photogenerate carriers, positioning relative to the illumination source plays an important aspect in the overall device performances. A side-by-side positioning allows both photoelectrodes to receive the full extent of the solar spectrum and thus exploit the entire absorption range of the materials employed, but it doubles the effective surface area of the device and thus effectively halves the efficiency per unit of surface. The other solution – currently the most investigated and studied – involves having the two photoelectrodes placed in a back-to-back tandem configuration. Concerning the illumination of the system, the tandem configuration entails an optical screening of the back absorber performed by the top absorber and implies a mutual calibration of the absorption range of the two photoelectrodes. Adopting a conservative value for the overall energetic losses in a tandem system, the optimal band-gap values for the two absorbers is calculated to be 1.89 eV and 1.34 eV for the top and back semiconductor respectively (Figure 1.8). The resulting system is able to achieve a maximum theoretical solar-to-hydrogen efficiency of 21.4%.[6]
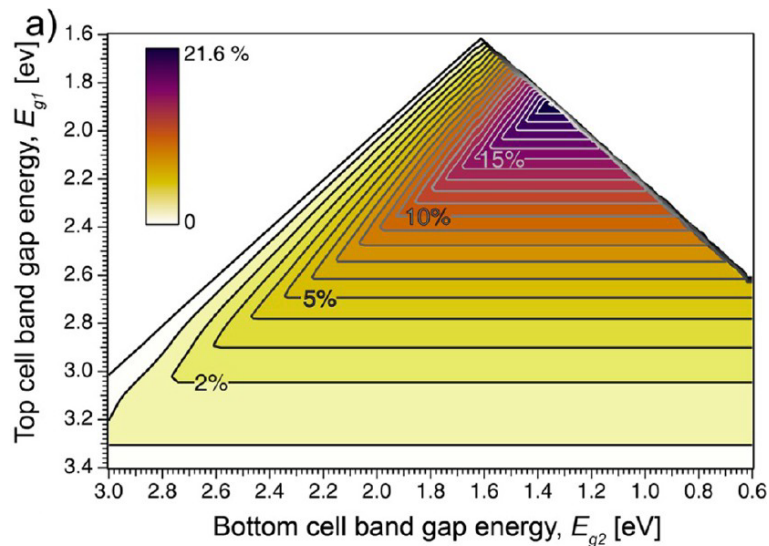
Figure 1.8 – Colored contour plot of the maximum theoretical STH efficiency (overall energetic losses set at 2.0 eV and AM1.5G solar irradiance) as a function of the band-gap energies of the two semiconductors.[6]

In all its possible configurations, a photoelectrochemical water-splitting system requires a direct connection of the two electrodes with a wiring in order to close the electrical circuit of charge transfer. In the configurations where a single photoactive electrode is connected to a simple catalytic counter electrode, the overall device operates without any external bias and circulates an amount of current dictated by the working photoelectrode yield. When two photoelectrodes are operating and each one is supplying a defined amount of current, the working point of the overall device correspond to the internal potential where both photocurrent values are equal; if the photoanode and photocathode were to be measured individually, the working point of the tandem system is the intersection point between the two current-voltage profiles, adequately changed in sign. An external bias can be provided to all photoelectrochemical systems in the form of a solar junction connected in line with the electrodes or a similar source of electromotive force, improving the amount of photocurrent generated as the working point of the photoelectrodes is no longer the zero-bias voltage, but doing

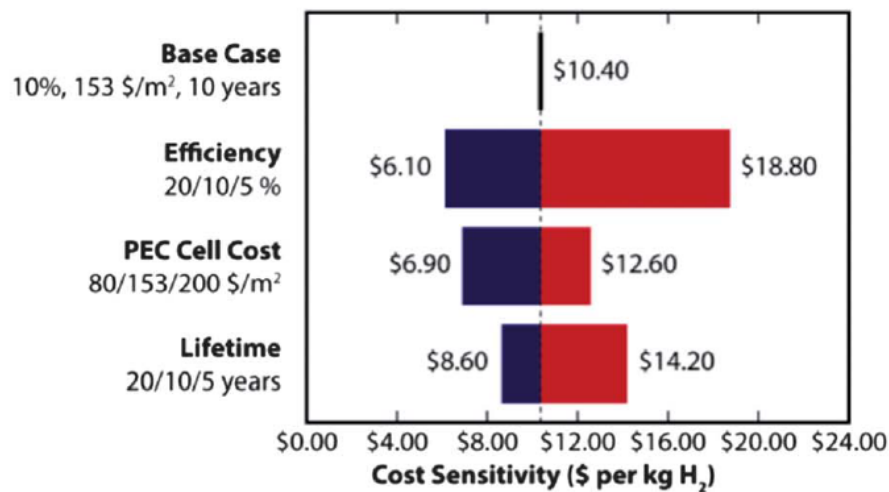so theoretically reduced the efficiency as an external energy contribution is implemented in the system.

Figure 1.9 – Cost sensitivity analysis for a PEC tandem system, showing the effects of a positive and negative change in the key operational parameters (efficiency, panel cost and lifetime) on the production cost of hydrogen.[5]

Techno-economic analyses conducted on solar production of hydrogen via photoelectrochemical water-splitting have defined the benchmark parameters for the feasibility of the process on large scales.[5,6] Production of hydrogen via PEC systems, contextualized in the current hydrocarbon-based energetic economy, starts to approach economic feasibility when the final production cost is below 10€ per kilogram of hydrogen. Translating this cost into operational parameters for a working system, an ideal PEC device needs a 10% solar-to-hydrogen efficiency, a 10-year-long lifetime and a fabrication cost of $150€·m^{-2}$. The efficiency threshold has already been surpassed by complex architectures employing III-V group semiconductors carefully deposited via epitaxial growth, while architecture made by nanoparticle films can be fabricated via wet processes that have an easy industrial scalability with expected costs far below the target value. However, no device has been yet developed satisfying both these requirements at the same time and the stability aspect is still far from the 10-year threshold. In order to

improve the performances towards the outlined direction, current research on photoelectrochemical water-splitting devices is focusing on new materials and architectures, designed to exploit each component to its optimal limit, with an eye of regard towards fabrication costs and working lifetime. According to the cost sensitivity analysis,[5] reducing the costs of PEC cells production and reaching a device lifetime in the range of $5 - 10$ years has a positive effect on the cost of hydrogen production that is comparable to a two-fold improvement on the device efficiency (Figure 1.9). This suggests a research direction focused on producing reliable and cheap PEC systems with adequate performances, rather than pushing the efficiency limit with complex and costly architectures that frequently lacks long-term stability.

1.3 Objective of the Work

The objective of this work is the fabrication, characterization and optimization of working electrodes for photoelectrochemical water-splitting applications. In accordance with the techno-economic analyses mentioned, simple fabrication techniques are employed to deposit inexpensive material in order to obtain efficient and lasting devices, optimizing the performances within the intrinsic experimental boundaries set by the materials themselves.

Concerning the photoanode architecture, a rather simple structure is employed, comprising a single nanostructured film of tungsten trioxide, fabricated with a plasma-assisted physical vapor deposition technique in a hierarchical morphology. The optimization process aims at improving the charge transport properties of the film, in order to facilitate charge extraction even at low applied biases. These enhanced performances are obtained by carefully tuning the deposition

parameters, obtaining a final morphology with high crystallinity and improved long-range order, defined as hyperbranched. Furthermore, the easy availability and high chemical stability of tungsten trioxide allow to obtain a durable and inexpensive photoanode.

A hybrid organic architecture is employed for the photocathode, belonging to the developing field of hybrid organic photoelectrochemical (HOPEC) water-splitting. The selected structure uses an organic blend as the photoactive material and two enclosing inorganic layers as the selective contacts that helps achieving separation and extraction of the photogenerated carriers. Recent publications on the topic present devices with high photocurrent yields and low onset potentials, even though lacking operational stability, mainly due to a degradation of the hole selective layer. This work tackles the open issue of material choice for the hole selective layer, proposing amorphous tungsten trioxide deposited via reactive sputtering. Tungsten trioxide satisfies the requirements of optical transparency and electronic alignment of its energy level with respect of the adjacent polymer bands, as well as providing in improved chemical stability that shifts the operational duration by one order of magnitude.

Chapter 2: Tungsten Trioxide

2.1 WO₃ Properties

Tungsten trioxide (WO₃) is a semiconducting transition metal oxide containing oxygen in the -2 oxidation state and tungsten in the +6 oxidation state. At room temperature, monoclinic γ-WO₃ is the most common and stable configuration, with other crystal phases occurring at different temperatures (Table 2.1).[7–10]

WO₃ Phase	Space Group	Temperature [K]
ε-monoclinic	P_c	< 230
δ-triclinic	$P_{\bar{1}}$	230 – 300
γ-monoclinic	$P_{21/n}$	300 – 623
β-orthorhombic	P_{nma}	623 – 1020
α-tetragonal	$P_{4/ncc}$, $P_{4/nmm}$	1020 – 1746

Table 2.1 – Classification of WO₃ crystal phases with their respective space ground and temperature range of formation.

All WO₃ stereoisomers present a perovskite-like atomic configuration with the ideal ABO₃ cubic crystal structure (Figure 2.1), where tungsten is the A atom at cube corner positions (0, 0, 0), oxygen atoms stay at face centered positions $(\frac{1}{2}, \frac{1}{2}, 0)$ and the B cation sits at body centered position $(\frac{1}{2}, \frac{1}{2}, \frac{1}{2})$. As the B cation is absent in tungsten trioxide, the ideal cubic cell undergoes distortions – such as antiferromagnetic displacements of W atoms, variations of the W-O bond length and mutual rotations of the WO₆ octahedra – that result in the aforementioned different crystal phases of WO₃. Monoclinic WO₃ consists in planar arrays of

corner-sharing WO_6 octahedra, placed perpendicular to the [001] hexagonal axis and held together along the z axis by Van de Waal's forces. In this structural configuration, the site of the missing cation B is empty and easily accessible through tunnels present between the octahedra, thus allowing for ionic transport and intercalation within the structure in case of an external force.
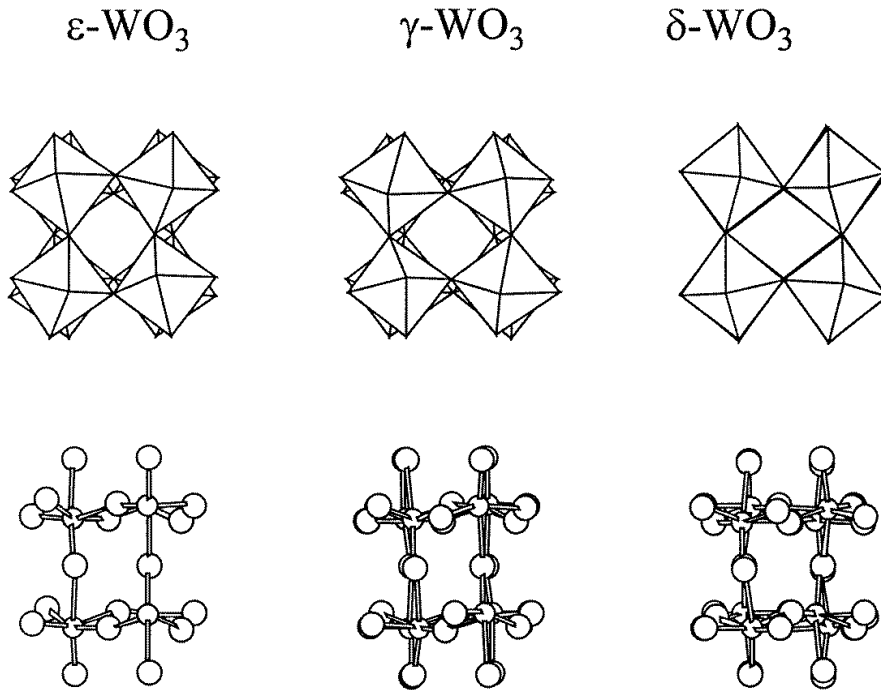
$$\varepsilon\text{-}WO_3 \qquad \gamma\text{-}WO_3 \qquad \delta\text{-}WO_3$$

Figure 2.1 – Crystal structure of the three low-temperature phases of WO_3 (ε-monoclinic, δ-triclinic and γ-monoclinic phases), showing the tilting of the WO_6 octahedra (top) and the configuration of the W–O bonds (bottom). The empty space within the octahedra is the vacant B site of the perovskite structure.[7]

Concerning the electronic band structure, group theory applied to the octahedral cell of WO_3 – oxygen atoms at the vertices and a tungsten atom at the center – delivers that the degenerate $5d$ orbital of tungsten is split by the octahedral crystal field of the neighboring oxygens into a low energy level t_{2g} that points into empty space and a higher energy level e_g that points toward the oxygen ion. Likewise, the oxygen $2p$ orbital is separated into a high-energy level $2p_\sigma$ that points into empty space and a lower energy level $2p_\pi$ that point toward the tungsten ion. As the approximation of the single octahedral unit is removed in favor of a real crystal,

the energy levels are substituted by energy bands. In an ideal crystal structure, the position of these energy bands result in a band-gap of 2.6 eV, but distortions of the crystal lattice due to strain and defects increase this value. In crystalline WO_3, the valence band (VB) is made by oxygen $2p_\pi$ states, the conduction band (CB) is made by tungsten $5d\ e_g$ states with a contribution of oxygen $2p$ states and the Fermi energy level lies in the region in-between. Conduction band energy E_{CB} is influenced by the degree of symmetrical arrangement the WO_6 octahedra have in the structure of a given crystal phases: conduction band energy is lower for high-symmetry octahedra since the electron in the conduction band are more delocalized.

For photoelectrochemical water-splitting applications, the optical band-gap around 2.6 eV allows to absorb light in the visible spectrum up to 480 nm and to achieve a maximum theoretical conversion efficiency of approximately 4.8%.[11] Due to the unavoidable oxygen vacancies present in the crystal lattice, WO_3 is considered a n-type semiconductor and thus it is mainly employed as a material for photoanodes. The valence band of WO_3 is located at 3 V_{NHE} and is positive enough to perform the water oxidation reaction. On the other hand, the conduction band lies above 0 V_{NHE} and is not negative enough to perform the water reduction reaction. In a photoelectrochemical device using WO_3 as a photoanode and platinum as the cathode, the full water-splitting reaction can only occur upon application of an external bias. The photoanodic performances are aided by a moderate hole diffusion length of approximately 150 nm and good electron transport properties,[12] which helps achieving good charge extraction and low recombination rates. In its stable monoclinic phase, WO_3 exhibits high resistance against photocorrosion and strong chemical stability in acidic solutions, as reported by the Pourbaix diagram of tungsten.

2.2 Bare WO₃ for PEC Photoanodes

After the discovery of the Fujishima-Honda effect in 1972,[3] the properties of WO3 as a viable material for photo-assisted water electrolysis are studied by Butler in 1977.[12] The first work about WO_3 employed as a photoanode for photoelectrochemical water oxidation appeared in 1987, published by Desilvestro and Grätzel.[13] Based on their previous work that investigated the properties of tungsten trioxide nanoparticles for photocatalytic water-splitting, the reported photoanode is fabricated with polycrystalline WO_3 nanoparticles sintered on a titanium foil substrate through a calcification process at 750°C under nitrogen stream, resulting in a compact film with a thickness between 10 – 20 μm. Despite the non-optimized morphology, the device shows an onset potential of 0.52 V_{RHE} and a photocurrent density in the order of 1 mA·cm⁻² under visible light illumination with an incident power of 630 mW·cm⁻². The number of publications regarding WO_3 photoanodes and its photoelectrochemical properties increased over the years, reaching a peak in the early 2000s, when the concept of hydrogen economy rose to public interest. A wide range of synthesis methods has been employed to investigate the capabilities of bare WO_3 as a photoanode material and achieve different morphologies and structures: spray pyrolysis,[13–17] sol-gel method (Section 2.2.1),[18–27] hydrothermal method (Section 2.2.2),[28–33] anodization (Section 2.2.3),[34–38] electrodeposition,[39–41] chemical vapor deposition (Section 2.2.4)[42–45] and physical vapor deposition (Section 2.2.5).[46–49] Morphological modifications are performed in order to enhance the performances of the photoanode, either by increasing the photogeneration yield or the charge extraction and charge transport processes. Dense nanoparticle and mesoporous nanoparticle films present high surface and strong internal light scattering, which in turn provide enhanced chemical reactivity at the extended electrolyte interface

and improved light absorption and conversion of photons into photogenerated charges. Its degree depending on the fabrication process, the main limiting factor in a nanoparticle film photoanode is the high density of interfacial boundaries between the grains that strongly increase the external bias required to efficiently extract the charges due to high recombination rates and poor charge transfer resistance. Nanostructured films with directional morphologies – such as nanowires, nanoflakes – or hierarchical structures exploit the resulting charge confinement to obtain preferential charge transport pathways with reduced resistance and lower recombination rates. Nanostructuring is usually paid at the expense of film density and thus optical absorption, resulting in lower photocurrents with better onset potentials.

2.2.1 Sol-Gel Method

Sol-gel is the most common synthesis route for WO_3 films. This chemical procedure consists in the preparation of a colloidal solution containing the metal oxide precursor and additional reagents to control the aggregation and nucleation of particles in the solution. Once the solution is adequately deposited on a given substrate via spin coating, dip coating or similar techniques, the remaining liquid solvent is removed in a drying process. The rate of solvent removal, governed mainly by the solvent type and the drying temperature, strongly determined the distribution of porosity in the resulting gel. Afterwards, a high-temperature thermal treatment is usually performed to further favor densification and promote transition towards the crystalline phase.
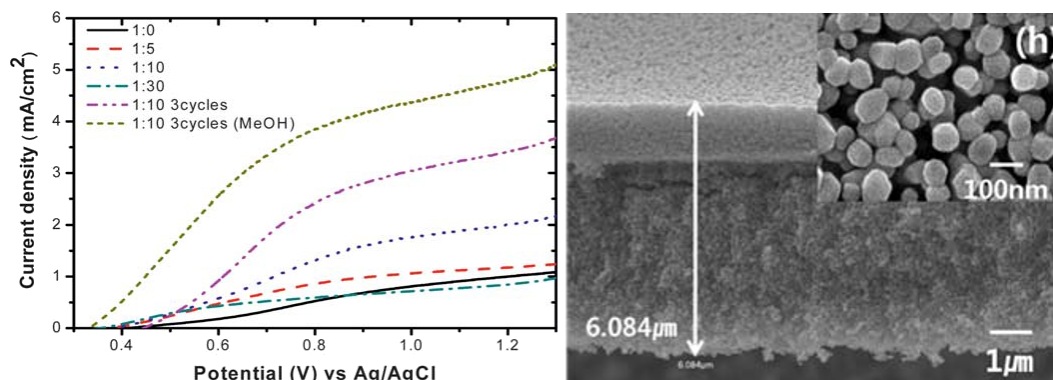
Figure 2.2 – Linear sweep voltammetry curves (left) of devices fabricated using tungstic acid with different weight ratio of W:PEG, performed under AM1.5 solar light in a 1 M sulfuric acid solution. SEM cross-sectional images (right) and high-resolution magnification (inset) of the "1:10 3cycles" device.[20]

Using an optimized sol-gel fabrication process where polyethylene glycol (PEG) is added to the peroxy-tungstate precursor to control the film porosity, Kim et al.[20] fabricated mesoporous nanoparticle films (Figure 2.2 right) that exhibit a photocurrent density around 3 mA·cm^{-2} at 1.23 V_{RHE} for the best-performing device (Figure 2.2 left). The onset potential occurs at 0.57 V_{RHE} and 1 mA·cm^{-2} is achieved after 200 mV, indicating poor charge extraction properties despite the efficient photon absorption and conversion manifested at high applied biases. The addition of methanol – a sacrificial agent with hole scavenging properties – to the electrolytic solution not only increases the overall photocurrent yield thanks to the current doubling effect, but also reduce the photocurrent onset potential by improving the hole extraction efficiency.

Employing a similar sol-gel method with poly-tungstic acid and polyethylene glycol, Brillet et al.[19] obtained mesoporous nanoparticle films that sacrificed the photocurrent yield for an improved charge extraction. The photocurrent density is 2.5 mA·cm^{-2} at 1.23 V_{RHE} and the onset potential is 0.51 V_{RHE}, with a current profile that reaches 1 mA·cm^{-2} approximately 150 mV after the onset. The IPCE of the device biased at 1 V_{RHE} shows a conversion efficiency above 80%. The current yield at low voltages – currently the state-of-the-art for mesoporous nanoparticle

WO$_3$ films – is exploited to efficiently couple the photoanode with a dye-sensitized solar cell (DSSC), obtaining a PEC-PV tandem cell with a 3% solar-to-hydrogen efficiency.

2.2.2 Hydrothermal Method

Hydrothermal synthesis is a chemical method that allows for the precise control over the size, shape distribution, and crystallinity of the nanoparticles fabricated, achieved through control of operational parameters, such as reaction temperature, reaction time, solvent type, surfactant type, and precursor type. The synthesis of crystals depends on the solubility of their minerals within the solvent under high pressure and high temperature. The precursor compound and water are supplied to a pressurized autoclave, with a controlled temperature gradient between its opposite ends. At the hot end the precursor dissolves, whereas at the cold end it deposits on a seed crystal, growing into the desired structure. A high-temperature sintering procedure is usually performed on the synthesized structures.

Biswas et al.[29] fabricated hierarchical flower-like structures using a single-step solvothermal process with ammonium metatungstate hydrate and hydrochloric acid (Figure 2.3 right). The flower-like hierarchical nanostructures are constructed by self-organized single-crystalline nanoscales, grown along the (001) direction. Increasing the amount of hydrochloric acid produces structures with a higher surface area, which helps obtaining improved photocatalytic performances. The fabricated nanostructures are deposited and sintered onto a conducting substrate, to obtain a working photoanode. The high crystallinity and directional growth of the flower-like structures enable efficient charge extraction, with an

onset potential of 0.42 V_{RHE} for the best-performing device (Figure 2.3 left). The reported photocurrent is 1.45 $mA \cdot cm^{-2}$ at 1.23 V_{RHE}, the yield limited by photon absorption and conversion, as the nanostructured film presents ample voids within the arrays of flower-like structures.
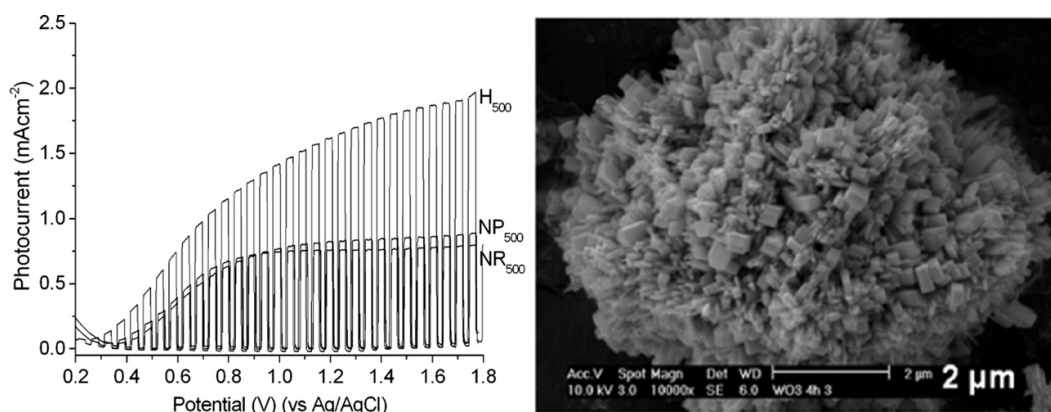

Figure 2.3 – Linear sweep voltammetry curves (left) of the hierarchical flower-like nanostructures H_{500} compared to nanoparticles NP_{500} and nanorods NR_{500}, performed under chopped AM1.5 solar light in a 0.5 M sulfuric acid solution (pH ≈ 0.3). High-resolution SEM image (right) of a single flower-like structure, prepared with 1.26 mL of HCl at 180°C for 4h.[29]

2.2.3 Anodization Method

The anodization is an electrochemical procedure that grows a film of metal oxide out of metal plate of the same material. The film is grown by passing a current between two electrodes immersed in an electrolytic solution, thus causing oxidation reactions at the metal surface. Tungsten plates or foils act as the anode where oxygen generation occurs, while hydrogen is formed at the counter electrode. The electrolyte is usually an acidic solution – used to balance the formation and porosity of the oxide layer – while additional reagents are employed to achieve further nanostructuring. Controlling the chemical nature of the electrolyte and the operational parameters of the electrochemical procedure influences the resulting film morphology.
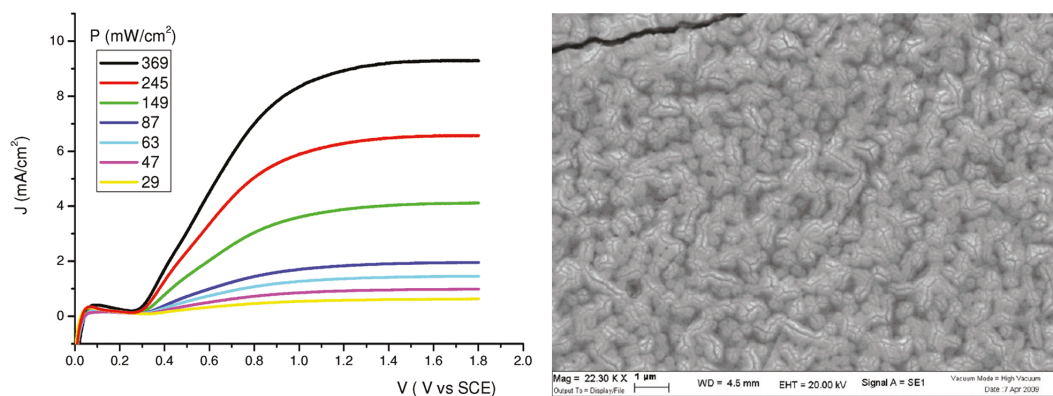
Figure 2.4 – Linear sweep voltammetry curves (left) of the device fabricated in NMF/H_2O 8:2 with 0.05% of NH_4F, performed in a 1 M sulfuric acid solution under different solar incident power. SEM top image (right) of the anodized worm-like nanostructure obtained in the optimal electrolyte.[34]

Cristino et al.[34] obtained worm-like WO_3 nanostructured photoanodes using anodization of tungsten foils in different organic solvents with high dielectric constant (Figure 2.4 right). The optimal electrolyte, in terms of electrochemical performances of the nanostructured photoanodes, is a mixture 8:2 of N-methyl-formamide (NMF) and water with the addition of a 0.05% in weight of ammonium fluoride (NH_4F). The optimized photoanode has an onset potential of 0.55 V_{RHE} and a photocurrent density of approximately 3.5 mA·cm^{-2} at 1.23 V_{RHE} under a solar incident power of 150 mW·cm^{-2} (Figure 2.4 left) This value, adequately rescaled for a standard AM1.5 incident power, is top-tier for WO_3 photoanodes fabricated via anodization, closing the performance gap with the devices produced via sol-gel or hydrothermal methods.

2.2.4 Chemical Vapor Deposition

Chemical vapor deposition (CVD) is a family of deposition processes used to produce high-quality thin films. During the deposition process the substrate is exposed to one or more volatile precursors that produce the desired film by reacting and decomposing on the substrate surface.
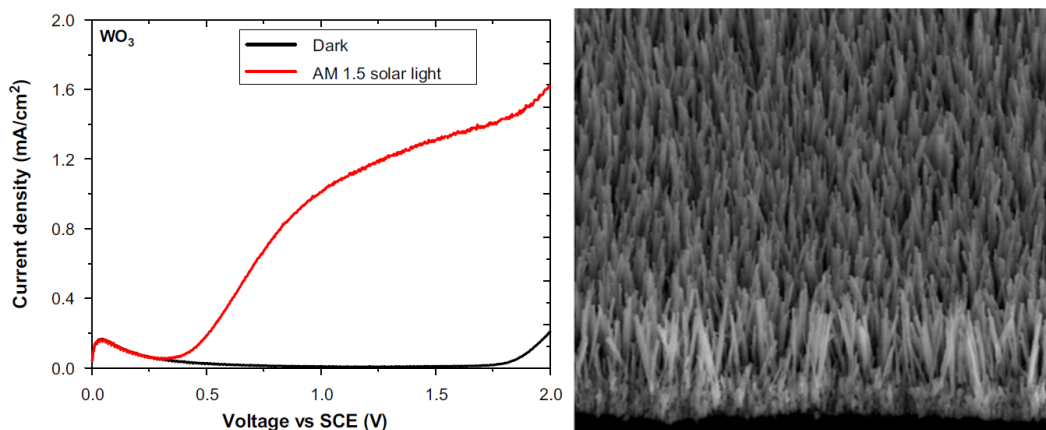
Figure 2.5 – Linear sweep voltammetry curves (left) of the nanowire structure, performed under AM1.5 solar light in a 0.5 M sulfuric acid solution (pH ≈ 0.3). SEM tilted-top image (right) of the nanowire arrays deposited on a FTO substrate.[42]

Chakrapani et al.[42] fabricated WO_3 nanowire arrays using a hot-wire chemical vapor deposition in a specifically designed reactor setup (Figure 2.5 right). The technique involves flowing oxygen gas over a hot tungsten filament, to produce vapors of the respective metal oxide which then diffuse within the reactor chamber and deposit on the substrate surface at a cooler temperature. The deposited films are then annealed in air in order to fully oxides the nanowire structures and achieve the complete, correct stoichiometry. The device has an onset potential of 0.55 V_{RHE} and photocurrent density of 1 mA·cm^{-2} at 1.23 V_{RHE} (Figure 2.5 left). The nanowire structure shows a remarkable conversion efficiency, with an IPCE value of 85% at 370 nm, despite the spectral extent of photon conversion is limited by the band-gap of 2.9 eV.

2.2.5 Physical Vapor Deposition

Physical vapor deposition (PVD) is a family of vacuum deposition methods to produce thin films. The film growth involves a physical process such as heating,

sputtering or laser ablation to produce a vapor phase of the material that is deposited on the substrates.
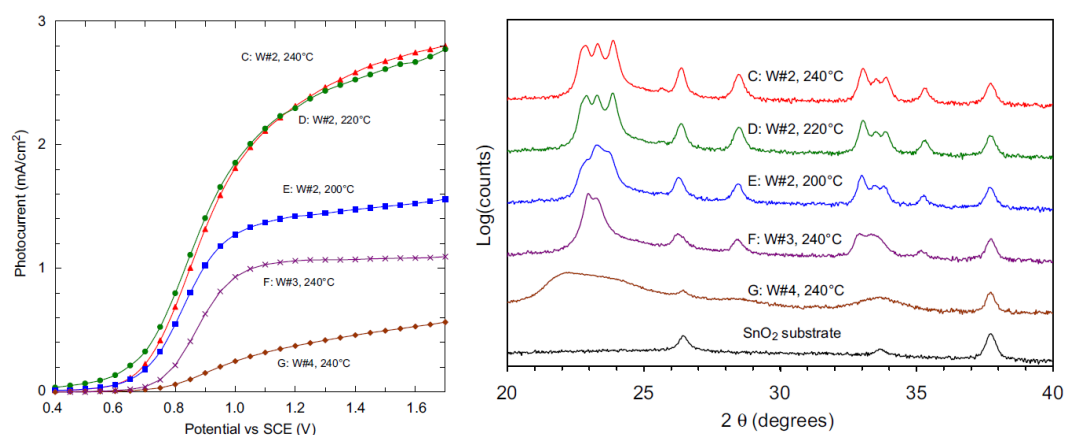

Figure 2.6 – Linear sweep voltammetry curves (left) of the nanostructures grown with different temperatures of the substrate and different sputtering targets, performed under AM1.5 solar light in a 0.33 M phosphoric acid solution (pH ≈ 1.3). XRD spectra of the different nanostructures, showing the effect of temperature in the peak pattern.[48]

Marsen et al.[48] employed reactive sputtering of a tungsten target in an oxygen/argon atmosphere to deposit WO_3 nanostructured films, characterized by a dense morphology with columnar growth. The crystallinity of the deposited films depends strongly on the substrate temperature, with bigger crystals having a beneficial effect on the photoelectrochemical performances (Figure 2.6). Above 220°C of temperature, the grain size reaches 27 nm and 49 nm along the (002) and (200) direction respectively. The photoanode exhibits a photocurrent density of 1.45 mA·cm^{-2} at 1.23 V_{RHE}, with an onset potential of 0.72 V_{RHE}.

As reported by Balandeh et al.[47] and discussed in this work, nanostructured devices are fabricated via pulsed laser deposition under carefully optimized conditions. The deposited films present a hyperbranched quasi-1D nanostructure comprised of highly crystalline nano-tree arrays with strong directional growth and efficient light harvesting properties. These features combine the efficient optical conversion of mesoporous nanoparticle film with the improved charge

transport properties of hierarchical directional nanostructures. The photoelectrochemical performances reflect these features, with an onset potential as low as 0.4 V_{RHE} and a saturation of the photocurrent already achieved at 0.8 V_{RHE} with a value of 1.85 mA·cm^{-2}. In the voltage range between the onset and the saturation potential, these hyperbranched nanostructured devices represent the current state-of-the-art for WO_3 photoanodes for photoelectrochemical water-splitting.

2.3 WO_3 Films for HOPEC Photocathodes

As a n-type semiconductor, WO_3 cannot be successfully employed as the photoactive material in a photocathode architecture. However, strong chemical stability in acidic environments, good charge transport properties and limited optical absorption in the visible range are prominent characteristics of an efficient transparent contact. Specifically, the energetic alignment of the conduction band and the adequate density of charge carrier make WO_3 a viable candidate for the role of hole selective material in the developing field of hybrid organic photocathodes.

2.3.1 Organic Photoelectrochemical Systems

The research field of organic photoelectrochemical (OPEC) water-splitting sprouts from the consolidated knowledge that the more mature field of organic photovoltaics (OPV) has acquired throughout the years. The concept is to draw from the conspicuous list of organic semiconductors employed for OPV and find the correct materials that adequately satisfy the water-splitting application

requirements. However, the transferability of organic semiconductors from photovoltaic applications to photoelectrochemical applications is not straightforward and depends on the inherent stability and proper functioning of a given material when immersed into aqueous electrolytic environments. Degradation mechanisms involve π-conjugation reduction, chain scission and cross-linking mainly caused by photo-oxidative reactions and photosensitization.[50] To assess the chemical stability, several organic semiconductors have been tested while operating in aqueous electrolytes, showing no sign of degradation in terms of spectral responsivity after photoelectrochemical operation.[51] The chemically stable organic semiconductors include P3HT, F8BT, MEH-PPV, PCDTBT and PCPDTBT from the donor family and PCBM, $PC_{70}BM$ and ICBA for the acceptor family, all already vastly investigated in OPV and with large commercial availability. For a photocathode system, many organic polymers appear as excellent candidates: the semiconducting p-type nature and the positive position of their LUMO levels with respect of the water reduction potential satisfy the energetic requirements to effectively perform the hydrogen evolution catalytic reaction,[52] while the optical band-gap energies between 1.6 – 2.1 eV allow for an efficient exploitation of the solar visible spectrum.

Preliminary studies concerning the use of organic semiconducting polymers to perform photoelectrochemical water-splitting began in the mid-80s and the first polymer-liquid junctions to evolve hydrogen displayed photocurrent densities in the range of $\mu A \cdot cm^{-2}$.[53–56] Following the development of OPV materials in the early 90s, the field of OPEC introduced P3HT as a donor material and understood the critical importance played by stereochemistry in order to improve charge conductivity[57,58] and the use of an acceptor material – like C_{60} fullerenes – to form a bulk heterojunction (BHJ) that severely mitigates electron-hole recombination.[59] After these preliminary results, research on OPEC applications significantly

decreased and the field was practically ignored for the next 15 years, due to the low absolute performances of the initial devices and the bigger expectation placed on inorganic materials like oxides, silicon and group III-V alloys.

2.3.2 Hybrid Organic Photoelectrochemical Systems

Interest on the topic of organic semiconductors for water-splitting applications resurfaced in recent years, thanks to several studies that obtained a deeper understanding of the mechanisms behind organic-liquid junctions.[60–63] Despite the improved charge separation provided by an organic bulk heterojunction comprising a photoactive polymeric donor material such as P3HT and a fullerene acceptor such as PCBM, charge extraction at the interfaces still represented a limiting factor for the device performances. The consequent introduction of catalytic layer to lower the water-splitting reaction activation energy and interfacial layer to favor the rapid extraction of the photogenerated carriers enabled a drastic increase in both the photocurrent yield – still stuck in the range of few $\mu A \cdot cm^{-2}$ – and the photocurrent onset potential – developing stacked junctions with a more favorable energy level alignment.[64–72] Despite PEDOT:PSS can be employed as an adequate selective contact for hole harvesting, the new materials for selective contacts are metals and oxides, inorganic materials. The photoelectrode architecture obtained with the introduction of inorganic interfacial layer becomes a hybrid organic photoelectrochemical (HOPEC) system, where the organic bulk heterojunction provides for the photogeneration of carriers and the inorganic layers promote charge extraction and transport, thus approaching the performances of only inorganic devices with comparable absorption.

2.3.3 HOPEC Photocathodes for Water-Splitting

Examining the performance trend of HOPEC photocathode for water-splitting applications, a simple roadmap can be compiled with the important milestones achieved in the last years.
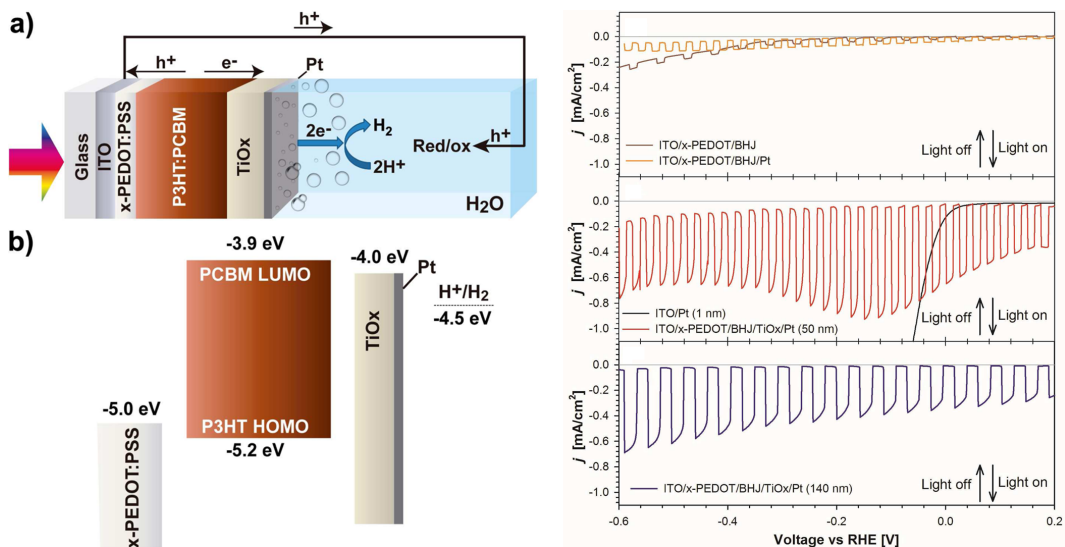

Figure 2.7 - Device architecture (left, a) and energy diagram (left, b) of the optimized HOPEC cell. Linear sweep voltammetry curves (right) of different configuration of the HOPEC cell, performed under chopped AM1.5 solar light in a 0.1 M sodium sulfate solution (pH ≈ 2).[66]

Haro et al.[66] in 2015 developed an architecture where the P3HT:PCBM bulk heterojunction is enclosed between a thin PEDOT:PSS hole selective layer (HSL) and a TiO$_x$ electron selective layer (ESL), covered by a sub-nanometric film of platinum as the hydrogen catalyst (Figure 2.7 left). With the designed energy level alignment, photogenerated electrons favorably move from the LUMO of the donor P3HT to the LUMO of the acceptor PCBM and then migrate towards the ESL interface where they are finally injected in the conduction band of TiO$_x$. Simultaneously, the hole photogenerated in the HOMO level of P3HT are extracted by the electrons coming from the PEDOT:PSS quasi-conduction band. The tangible effect introduced by the selective layers is observed in the transition of the photocurrent yield from the few μA·cm^{-2} obtained by the BHJ alone to the several

hundred µA·cm^{-2} achieved by the complete architecture (Figure 2.7 right). Additionally, chronoamperometry measurements show that devices with a thicker TiO$_x$ layer have better stability and longer lifetimes, but give a lower photocurrent yield, since a thicker ESL provide more charge transport resistance and a possible higher rate of defect recombination.
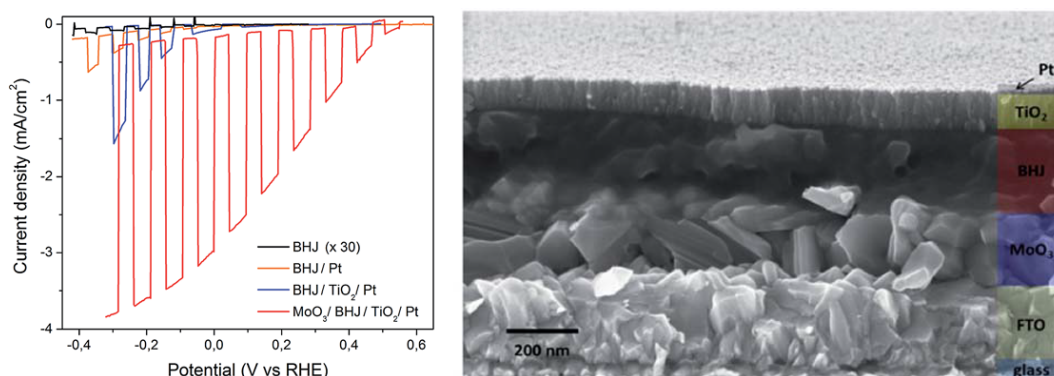

Figure 2.8 – Linear sweep voltammetry curves (left) of different configuration of the HOPEC photocathode, performed under chopped AM1.5 solar light in a 0.1 M sulfuric acid–sodium sulfate solution (pH ≈ 2). SEM cross-sectional image (right) of the different layers comprising the complete architecture.[68]

In the early 2016, Fumagalli et al.[68] presented a photocathode architecture with both the selective contacts made of inorganic materials: TiO$_2$ as the electron selective layer and MoO$_3$ as the hole selective layer (Figure 2.8 right). The photoelectrochemical performances – collected also for incomplete architectures – clearly show the impact on both the photocurrent density and the onset potential provided by a properly designed selective contacts, thanks to the improved charge extraction efficiency. The complete device has an onset potential of 0.67 V$_{RHE}$ and photocurrent density of 3.1 mA·cm^{-2} at 0 V$_{RHE}$ (Figure 2.8 left). Unfortunately, when place in an electrolytic solution under cathodic potentials, MoO$_3$ undergoes intercalation and reduction reactions, eventually converting into its reduced phase of MoO$_2$ that easily dissolve in water. This unwanted feature negatively affect the stability and durability of the photocathode performances.
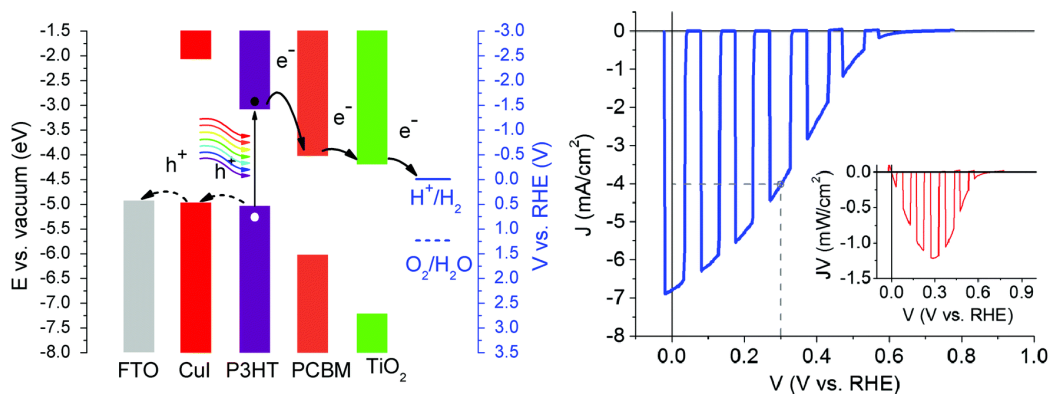
Figure 2.9 – Energy diagram (left) of the photocathode architecture, with all the charge transfer processes occurring during operation. Linear sweep voltammetry curve (right) of the device, performed under chopped AM1.5 solar light in a 0.1 M sulfuric acid solution (pH ≈ 1). Output power density curve as a function of the applied voltage (inset), with the maximum power point identified by the dashed grey lines.[71]

Later that same year, Comas-Rojas et al.[71] further improved the performances of the architecture proposed by Fumagalli et al. by using copper iodide (CuI) as the hole selective layer instead of MoO_3. Thanks to its low work-function and wide band-gap, the valence band of CuI lies slightly above the HOMO level of P3HT and thus can easily extract the photogenerated holes (Figure 2.9 left) without the need for a high density of majority carriers in the conduction band like in the case of MoO_3 or PEDOT:PSS. The favorable energy alignment, coupled with the nanometric thickness of the CuI layer that strongly reduce the charge transport resistance in the HSL, allows the photocathode to achieve an onset potential of 0.7 V_{RHE} and a photocurrent density of 7.1 mA·cm^{-2} at 0 V_{RHE} (Figure 2.9 right). The downside of CuI is the high solubility in water that result in the rapid failure of the photoanode after less than 2 hours of operation. To prevent this rapid degradation, a protective layer of polyethyleneimine (PEI) is deposited over the complete device, effectively increasing the overall lifetime but failing to prevent the gradual decrease of the photoelectrochemical performances.

The photocathode architecture presented in this work and recently published by Mezzetti et al.[72] proposes amorphous WO_3 as a viable material for the role of HSL,

thanks to its widely-demonstrated stability in acidic environments. As a stable electrochromic material,[73] the behavior of amorphous WO_3 is investigated while under cathodic working conditions, probing the shifts in energetic level alignment and carrier density caused by proton intercalation. Being a transition metal oxide with a crystalline structure and an electronic level alignment similar to MoO_3, the resulting performances are in line with the photocathode architecture presented by Fumagalli et al.,[68] only with an improvement in operational lifetime of one order of magnitude, from less than one hour to tens of hours, currently among the best performances in terms of hybrid photocathode operational stability.

Chapter 3: Experimental Methods

3.1 Photoanode Fabrication

3.1.1 Substrate Preparation

In the field of photoelectrochemical water-splitting, working electrodes are usually fabricated on glass substrates covered with a thin compact layer of transparent conductive oxide (TCO). These substrates are industrially made and commercially available with different materials, film thickness, optical and electrical properties. Nevertheless, all substrates share common properties that are required for their application: high transparency in the visible range and low surface resistivity.

For the fabrication of nanostructured WO_3 photoanodes, Solaronix TCO22-15 glass substrates are employed, consisting in a 2.2-mm-thick glass sheet covered with a 200-nm-thick fluorine-doped tin oxide (FTO) conducting layer. The substrates have a transmittance over 80% in the spectral range between 400 nm and 700 nm, a sheet resistance of 15 Ω/sq and a root-mean-squared surface roughness of 20 nm. Additionally, FTO can withstand high-temperature annealing treatments without any significant degradation of the film conductive properties that are exhibited by other TCOs due to a loss of the dopant from the oxide lattice. The square glass sheets are cut into 15-mm-by-20-mm samples with a glass-cutter, the proper size to appropriately fit both the fabrication and the measuring setups. The cut substrates are carefully cleaned through a series of ultra-sonication baths in different solvents for 30 minutes each. First, a 2% Hellmanex® – an alkaline liquid

detergent designed for quartz and glass cleaning – water solution in order to remove traces of industrial contaminants; then, distilled water in order to wash away any residual trace of the detergent. Lastly, Acetone followed Isopropyl Alcohol to further remove organic contaminations and residual particles from the substrates. The last step is the Oxygen Plasma Cleaning, performed for 10 minutes with a power of 100W to completely clean the surface from any possible contaminant, right before the substrates are placed on the holder inside the deposition chamber.

3.1.2 WO$_3$ Nanostructured Film

Fabrication of the WO$_3$ nanostructured films is performed using the pulsed laser deposition technique. The fabrication setup comprises two main components: the deposition chamber and the laser source (Figure 3.1). The deposition chamber is connected to a vacuum system that allows to reach pressures in the order of 10^{-3} Pa with the combined work of a rotary scroll pump for the high-pressure regimen and a molecular turbo pump for the low-pressure regimen. A multi-axis motorized system is connected to the chamber flanges and is employed to independently move the target material holder and the substrate holder. The laser source employed for the deposition is a krypton fluoride excimer laser (Coherent, COMPexPro 205) with a wavelength emission of 248 nm, a pulse duration of 15 ns and a pulse repetition rate of 20 Hz. The laser beam enters the chamber through a transparent quartz window, is aligned with the aid of mirrors and is collimated on the target using a plano-convex lens place on a moving stage. The energy of the laser pulses and the dimension of the laser spot on the target material – modified by changing the focusing of the lens – are chosen concordantly in order to obtain a specific value of laser fluency. Type and pressure of the background gas, distance

and relative motion between target material and substrates also influence the deposition process and thus the resulting morphology of the film.
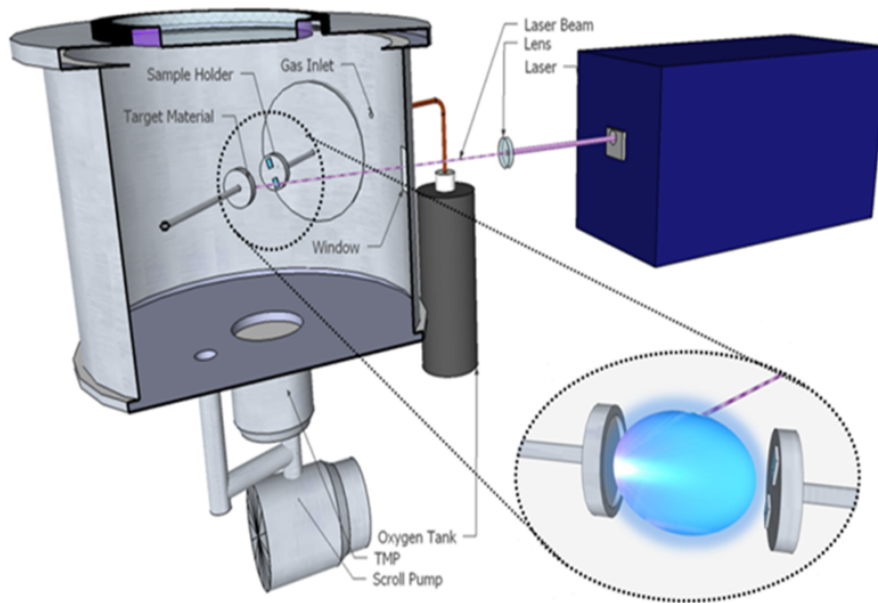

Figure 3.1 – Schematic of the pulsed laser deposition setup comprising the deposition chamber and the laser source.

The pulsed laser deposition is a particular physical vapor deposition technique and the process can be briefly summarized as follows. When a laser pulse impinges on the surface of the target material, the first part of the pulse is absorbed by the target material. Due to the high concentration of energy, the target material is locally vaporized and the ablated particles – ranging from single atoms, to molecules or large clusters – are ejected in a supersonic plume, caused by the strong pressure difference between the chamber and the bulk material. As these processes occurs on a rapid timescale, the second part of the laser pulse interacts with the supersonic plume, ionizing it into a plasma. The plasma plume expands supersonically along the direction perpendicular to the target material surface and towards the intended substrates, where the deposition of the ablated specimens occurs. The deposition dynamics depend on the characteristics of the plasma plume and the degree of interaction with the substrates. Moving away from the

target material, the ionized particles of the plasma plume interact with the background gas atoms though collisions and gradually lose their kinetic energy. It is possible to select the kinetic energy of the particles arriving on the substrates by placing the substrate holder at a specific position within the plasma plume and thus changing the deposition regimen. High-energy particles result in compact, dense films thanks to the enhanced surface restructuring and reorganization due to the increased residual energy possessed by the deposited particles; on the other hand, low-energy particles result in porous, aerogel-like structures with ample voids between the particle aggregates. Between these two diametrical conditions, a wide range of intermediate morphology can be obtained by appropriately tuning the deposition parameters. Within a narrow processing window that differs for each deposited material, it is possible to induce nucleation of clusters in the gas phase of the plasma plume. Upon interaction with the background gas, the clusters are strongly scattered and reach the substrate surface in soft-landing conditions, thus obtaining the self-assembly of mesoporous quasi-1D nanostructures with a peculiar tree-like shape. Since the deposition rate and the angular distribution of particle impacts change along the width of the plasma plume with a centrosymmetric profile, the substrate holder is kept in rotation slightly off-axis with respect of to the central direction of the plasma plume, in order to improve the homogeneity of the deposited film and to remove any spatial-related effect on the film growth. The target material is also moved in a rotatory-translational pattern in order to expose the whole material surface to the laser pulses and thus obtain a uniform usage of the target.

To obtain quasi-1D nanostructured films, the pulsed laser deposition process is performed ablating a WO_3 sputtering target (Testbourne, 99.9% pure) in an atmosphere of pure oxygen (Rivoira, 6.0 purity) to help maintaining the correct stoichiometry of the material inside the ionized plasma plume. Hierarchical

nanostructures are obtained within a pressure range between 10 – 60 Pa, but the optimized hyperbranched morphology develops only at 20 Pa of pressure, given the correct ablation of the material. The optimal value of laser fluency that induces gas-phase nucleation in the plasma plume is 3.4 $J \cdot cm^{-2}$, carefully calculated dividing the incident power – net of all the optical losses – by the laser spot size on the target. The substrate holder, given the shape of the plasma plume resulting from the background pressure and the ablation energy, is place at 50 mm from the target material and continuously rotates at 10 rpm. Under these specific parametric conditions, quasi-1D hyperbranched WO_3 nanostructures are homogeneously grown over FTO-covered glass substrates, the film thickness linearly scaling with the deposition time and resulting in a 2.4 $nm \cdot s^{-1}$ growth rate. The hierarchical morphology used for comparison throughout the whole photoanode characterization is deposited employing a slightly modified laser fluency.

3.1.3 Thermal Treatment

The WO_3 films deposited by PLD are amorphous, but already display the distinctive tree-shaped structure. To obtain the transition towards a crystalline nanostructure, the deposited samples undergo a careful thermal treatment in an annealing muffle furnace. Annealing temperature, duration of the thermal treatment and the slope of the heating/cooling ramps are optimized according to literature studies in order to obtain a high degree of crystallinity and to avoid damaging the nanostructure with uncontrolled thermal stresses. The process is performed in a Lenton muffle furnace and consists in a 2-hour annealing in air at 500°C, with controlled heating/cooling ramps of 4°C per minute. The selected temperature – within the formation range of orthorhombic WO_3 – is used to

facilitate a full phase transition of the amorphous film. Both the heating and the cooling ramps are tuned to reduce strains related to thermal expansion and compression, but the slow cooling time is also exploited to allow crystallite reorganization within the nanostructure as it approaches and crossed the formation temperature of monoclinic WO_3, the stable phase at room temperature.

3.2 Photocathode Fabrication

3.2.1 Substrate Preparation

For the fabrication of the hybrid organic photocathode, Solaronix TCO22-15 glass substrates are employed, consisting in a 1.2-mm-thick glass sheet covered with a 100-nm-thick indium-doped tin oxide (ITO) conducting layer. ITO-covered substrates present the same optical transparency and electrical conductivity of FTO-covered ones, but the root mean squared surface roughness is only 3 nm. The lower roughness, not need for the micrometer-thick photoanodes, is important for the successful fabrication of the photocathode architecture, where the thickness of the different layers is in the order of hundreds of nanometers. Furthermore, the work function of ITO better suits the energy level alignment of the amorphous WO_3 layer deposited on top. The cut dimensions, cleaning procedure and plasma treatment of the ITO-covered glass substrates are the same ones described in Paragraph 3.1.1 for the photoanode substrates.

3.2.2 Amorphous WO$_3$ Hole Selective Layer

Fabrication of the amorphous WO$_3$ hole selective layer is performed using the pulsed-DC magnetron sputtering deposition technique in reactive environment. The process is performed in the same deposition chamber of Section 3.1.2, placing the sputtering source in front of the substrate holder, instead of the target holder for pulsed laser deposition. Sputtering is a well-known physical vapor deposition technique that exploits the ionized atoms within a plasma to erode a target material and deposit the ejected particles on a given substrate. The gaseous plasma is generated by applying a strong voltage – in this case from a pulsed-DC generator – between the sputtering target and the substrate holder, respectively the cathode and the anode of the system: free electrons present in the chamber are immediately accelerated towards the anode, thus positively ionizing the neutral gas atoms encountered along their path. The ionized gas atoms are therefore accelerated by the electric field toward the cathodic target material, impacting on its surface with high kinetic energy and releasing neutral particles of the target material toward the substrate holder placed oppositely. The energetic distribution of the deposited particles can be tuned by adjusting the relative position of the substrate holder and the intensity of the electric field, that translates into the kinetic energy of the ionized gas atoms. In a magnetron sputtering, permanent magnets placed behind the cathodic electrode generate a magnetostatic field in the proximity of the target material (Figure 3.2). In this way, free electrons are trapped in spiral trails along the magnetic flux lines and the plasma is confined near the target material, increasing the sputtering rate and reducing electron bombardment on the deposited film, which might cause over-heating and unwanted structural modification. In a standard sputtering process the deposition chamber is filled with few Pascals of an inert gas like argon. In a

reactive sputtering process, the inert background gas is mixed with a small percentage of reactive gas, that is activated by the plasma and can react with the sputtered material.
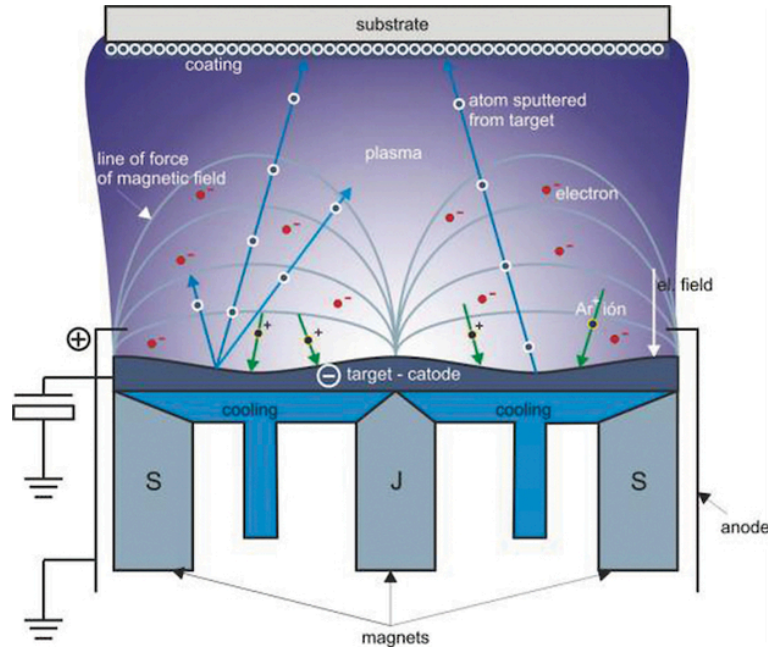
Figure 3.2 – Schematic of the working principles behind magnetron sputtering deposition.

To obtain the amorphous WO_3 layer, the reactive magnetron sputtering process is performed using a W metal target (Testbourne, 99.95% pure) in a 1.2 Pa mixture of pure argon (Rivoira, 6.0 purity) and pure oxygen (Rivoira, 6.0 purity), in order to oxidize the surface of the sputtered material and the ejected particles inside the plasma discharge, thus depositing the desired oxide material on the substrates. Reactive sputtering of the metal target in an oxidizing atmosphere is preferred to standard sputtering of the respective oxide since it can be performed with a simple pulsed-DC power source instead of a radio frequency generator and the sputtering yield for a metal target is much higher than for an oxide material. Argon and oxygen are mixed with an optimized value of 70:30 volumetric ratio. At higher concentrations, oxygen competes with argon in the ionization process, drastically reducing the argon plasma density and its sputtering efficiency. Furthermore,

oxygen atoms get negatively ionized by the interaction with free electrons and are consequently accelerated towards the anodic contact, bombarding the deposited film surface and causing an unwanted process of re-sputtering. On the other hand, lower oxygen concentrations fail to completely oxidize the sputtered material and produce sub-stoichiometric WO_x films. Despite the sub-stoichiometric WO_x phases are characterized by an improved conductivity, they also present moderate optical absorption in the visible spectral range and are thus detrimental within the proposed architecture where high transparency of the hole selective layer is mandatory to avoid shadowing the organic blend absorption. In order to deposit stoichiometric WO_3 on the substrates, the surface of the W target is conditioned beforehand, operating the magnetron sputtering for several hours alone in the reactive atmosphere. This conditioning creates an initial oxide layer on top of the metal target, which is the actual sputtered material during the deposition on the substrates. The deposition of the compact film of amorphous WO_3 is performed using a generator power of 50 W – working point 85 mA and 590 V – and with the substrate holder in front of the sputtering target at 50 mm of distance. The substrate holder rotates in axis with the sputtering plasma profile, obtaining a wide central area of uniform deposition. Films with different thickness are obtained by calibrating the process growth rate and regulating the deposition duration accordingly.

3.2.3 P3HT:PCBM Bulk Heterojunction

The bulk heterojunction of the photocathode architecture is an organic blend between a polymeric donor and a fullerene acceptor. The polymer employed is poly(3-hexylthiophene-2,5-diyl) and the fullerene is [6,6]-phenyl C61 butyric acid methyl ester, respectively known with the abbreviation P3HT and PCBM. The

blend is obtained dissolving P3HT (Sigma Aldrich, regioregular, electronic grade, 99.995% pure, average molecular weight 15000 − 45000) and PCBM (Nano-C, 99.9% pure) in a 1:1 weight ratio inside chlorobenzene (Sigma Aldrich, electronic grade) with a final density of 25 mg·mL^{-1} for each component. The obtained solution is stirred more than 24 hours on a hotplate at approximately 60°C, in order to completely dissolve and intermix the two powdered constituents. The deposition of a thin film of organic blend is performed via spin-coating technique. Before the spin-coating procedure, the ITO-covered glass substrates with the amorphous WO_3 layer undergo a 10-minutes Oxygen Plasma Cleaning treatment at 100 W of power. This treatment is performed to both clean the surface from contaminants and break the superficial bonds of WO_3, thus improving the surface wettability versus the solvent. A small amount of organic blend – approximately 80 µL, enough for the chosen substrate size – is pipetted to homogeneously cover the whole surface of the sample and the spin-coating program is started immediately after, rotating for 60 s at 1600 rpm with maximum acceleration. A brief time to let the residual solvent evaporate is required after the spin-coating process. By calibrating the solution density, the spin-coating rotation speed and duration, a thin film of organic blend around 200 nm in thickness is homogeneously deposited of top of the amorphous WO_3 layer. To activate and properly segregate the fullerene acceptor and the polymer donor, the organic blend need to undergo an annealing treatment. However, the thermal activation of the organic blend is postponed after the completion of the full photocathode, since the presence of the blend/TiO_2 interface helps the correct segregation of PCBM toward the electron selective layer and P3HT toward the hole selective layer, as desirable for the selected architecture.

3.2.4 Amorphous TiO$_2$ Electron Selective Layer

After the amorphous WO$_3$ hole selective layer via reactive magnetron sputtering and the P3HT:PCBM bulk heterojunction via spin-coating, the amorphous TiO$_2$ electron selective layer is fabricated via pulsed laser deposition. The experimental setup employed is the same one described in Section 3.1.2 for the fabrication of the WO$_3$ photoanodes. The process is performed ablating a TiO$_2$ sputtering target (Testbourne, 99.9% pure) in a 15 Pa reducing atmosphere of argon-hydrogen (Rivoira, 6.0 purity, 5% hydrogen in volume). The background gas pressure of 15 Pa and the laser fluency tuned to 2.1 J·cm^{-2} are within the operational window that allows to grow TiO$_2$ into hierarchical nano-trees. The reactive atmosphere of argon-hydrogen is instead exploited to reduce the clusters in the plasma plume and thus achieve slightly sub-stoichiometric films with an improved conductivity, as widely reported in literature for the different TiO$_x$ phases. The deposition duration is calibrated to obtain 100-nm-thick amorphous TiO$_2$ nanostructured films, replicating the upper configuration of previous photocathode architectures. During the aforementioned PLD process and the subsequent platinum sputtering, the samples are protected with a patterned mask that defines to deposited area to a 10-mm-by-10-mm square placed in the center of the substrate, in order to intrinsically define the active are of the final device.

3.2.5 Platinum Catalytic Layer

The platinum layer is deposited on top of the amorphous TiO$_2$ film with the same technique employed for amorphous WO$_3$ – described in Section 3.2.2 – only in a non-reactive environment. The pulsed-DC magnetron sputtering deposition is performed using a power of 22 W – working point 56 mA and 390 V – on a platinum

sputtering target (Kurt J. Lesker, 99.9% pure) in an inert atmosphere of pure argon (Rivoira, 6.0 purity). The background gas pressure is set at 15 Pa, in order to operate in a soft-landing regimen and obtain a dispersed distribution of platinum particles over the nanostructured TiO_2 surface, with no risk of deep implantation or formation of a dense capping layer. Since the amount of platinum required to have an efficient catalytic layer is very small, the dispersed platinum particles deposited on top of the device only amounts to 15 nm in thickness. The same mask employed for TiO_2 pulsed laser deposition is employed for platinum sputtering, in order to clearly define an area where all the layers comprising the photocathode architecture are present.

3.2.6 Thermal Activation

Once the device is complete, a thermal procedure is performed on the samples in order to activate the organic blend. Upon heating up to a certain temperature, the bulk heterojunction starts segregating its comprising P3HT and PCBM towards the appropriate selective contacts. The polymeric donor P3HT segregates towards the interface with the amorphous WO_3 hole selective layer and the fullerene acceptor PCBM segregates towards the interface with the amorphous TiO_2 electron selective layer, thus helping the correct separation and injection of photogenerated charges. For the procedure, the complete photoanodes are place on a hotplate at 130°C for 10 minutes inside a nitrogen glove-box with no oxygen content. The inert environment is fundamental to avoid degrading the organic blend, which can withstand atmospheric oxygen at room temperature, but can be easily oxidized by the oxygen radicals that are thermally excited at higher temperatures. Once the photocathode has undergone its thermal activation, the device is considered completed and it is ready to perform photoelectrochemical

water-splitting once connected as the working electrode in the electrochemical cell.

3.3 Electrochemical Cell

The electrochemical cell is the complete working system that actually performs the photoelectrochemical water-splitting process. The configurations adopted in this work are the ones involving the use of a single photoelectrode – whether an anode or a cathode – coupled with a catalytic counter electrode, immersed in an aqueous electrolyte that acts as the ionic conductor. As the electrochemical measurements are performed in a three-electrode configuration, a reference electrode is also used in the cell, placed in close proximity of the working electrode. The container is a transparent glass cell with airtight openings to connect electrodes or other external components and has two quartz sides where solar illumination can pass through without any detrimental absorption in the UV spectral range. Each component is carefully cleaned with distilled, deionized water before being assembled in the final electrochemical cell, in order to avoid any contamination of the experimental setup. During operation, the cell is sealed and the internal environment is kept inert by continuously flowing nitrogen through an inlet/outlet gas system, that also allows to bubble gas inside the liquid solution and thus perform the degassing process of the electrolyte.

3.3.1 Illumination System

The illumination system consists in a solar simulator (Lot Oriel, model LS0306) that uses a filtered 300 W xenon arc lamp to reproduce the solar spectrum with the

correct spectral densities in both the ultraviolet, visible and infrared range of emission. The spectral emission adopted, in accordance with the international standards for solar energy applications, is the AM1.5G solar spectrum (Figure 3.3). The AM1.5G standard describes the intensity and spectral density of solar photons reaching the Earth surface with a 48.2° zenith angle, which corresponds to a 1.5 atmospheric thickness and results in an incident power density of 100 mW·cm^{-2} or 1000 W·m^{-2}. The selected standard is the most appropriate spectrum for solar applications as it represents the solar irradiance during springtime/summertime of the latitude area where all the major modern countries lie.
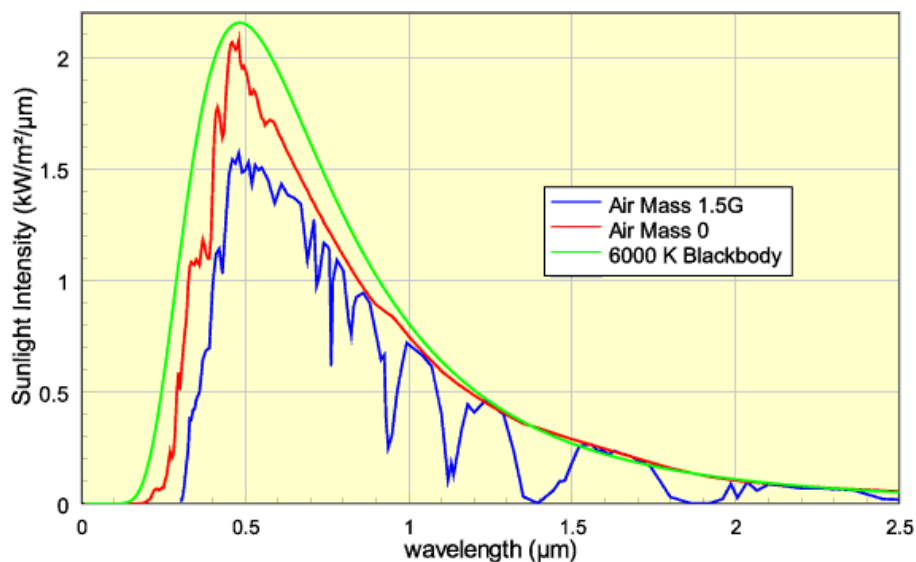
Figure 3.3 – Spectral irradiance profile of the AM1.5G and AM0 (zero-atmosphere) solar standards. The black-body radiation of an object at 6000 K is used to approximate the emission from the Sun surface.

3.3.2 Counter and Reference Electrodes

The counter electrode used in the electrochemical setup consists in a thin platinum wire, arranged as a coiled spring. Platinum is used as the counter electrode for both the photoanodic and photocathodic devices, as it is the best

performing catalyst for hydrogen evolution and is second only to ruthenium oxide as a catalyst for oxygen evolution. The coiled wire presents a large surface area that allows for an efficient charge exchange with the electrolyte and ensures that the reaction at the working electrode surface is not limited by the counter electrode. The thinness of the wire reduces the stickiness of gas bubbles on the surface of the counter electrode, thus avoiding their unwanted accumulation during the water-splitting process.

The reference electrode used in the three-electrode configuration is a silver/silver chloride redox couple in saturated potassium chloride (Ag/AgCl in saturated KCl) and is the most convenient choice for measurements performed in acidic solutions. The selected reference electrode has a potential of +0.1976 V with respect of the Standard Hydrogen Electrode (SHE) potential. This offset value, together with the correction due to the pH of the electrolytic solution, is added to the recorded potential values in order to express the measurements according to the reference scale of the Reversible Hydrogen Electrode (RHE) potential.

3.3.3 Electrolytic Solutions

The electrolyte used for the electrochemical measurements is a highly acidic sulfuric acid solution, with a pH range between 0 – 1. The acid solution is made by pouring an adequate quantity of sulfuric acid (Sigma Aldrich, 95-98% concentrated) into distilled and deionized water. The solution is then stirred extendedly to ensures both the first and second dissociation of the diprotic acid have reached their equilibrium. Lastly, the solution is measured with the aid of a pH-meter and is possibly corrected to the desired acidity value by adding small amount of water or single drops of acid, repeating the pH measurement

afterwards. The precise pH value of the electrolytic solution is important to understand the chemical environment where the device operates and to correctly report the potential range according to the Reversible Hydrogen Electrode reference scale. Together with the offset tied to the reference electrode employed, the electrolyte pH value generates a correction factor to be added, calculated using Nernst equation. The overall equation to calculated the RHE potential from the reference electrode potential is the following:

$$E_{RHE} = E_{REF} + E^0_{REF} + 0.0591 \cdot pH$$

where E_{REF} is the desired potential value in the RHE potential reference, E_{REF} is the potential value measured with respect of the reference electrode, E^0_{REF} is the offset correction value related to the particular reference electrode employed. Before each session of measurements, the electrolytic solution undergoes a degasification process in order to remove the dissolved reactive gases from water. The procedure involves flowing nitrogen through a gas bubbler immersed in the solution for approximately one hour. The intended purpose of the process is to remove dissolved oxygen from the electrolyte, since its oxidation is a competing reaction that might occur at the photoelectrode surface, especially in the case of photocathodes. After oxygen removal, the cell is kept airtight in nitrogen atmosphere, to avoid the eventual reabsorption of oxygen from air.

3.3.4 Three-Electrode Configuration

The complete electrochemical characterization of the fabricated photoanodes and photocathodes is performed in a three-electrode configuration, in order to focus on the interfacial behavior of the single working photoelectrode employed. In a two-electrode configuration, the counter electrode has to provide the charges

required by the working electrode reactions and concurrently has to gauge the working electrode potential. In this way, the potential drop measured is related to the whole electrochemical cell, including the contributions of the counter/electrolyte interface and the electrolyte itself. While this is viable measurement setup, it does not investigate precisely the electrochemical reactions occurring at the working electrode surface. Furthermore, it is experimentally difficult for a single electrode to maintain a constant potential while flowing conspicuous amount of charges to balance redox reactions. In a three-electrode configuration, the counter electrode has the sole task of supplying charges to the system and the reference electrode has the sole task of providing a reference potential for the measurement. In fact, the reference electrode acts as a half cell with a well-known potential, with no current flowing through it. In a three-electrode configuration, the charge current flows between the working electrode and the counter electrode, in accordance with the applied potential. This potential is measured between the working electrode – kept at a fixed, stable potential – and the reference electrode in close proximity with it, so that the potential at the working electrochemical surface can be finely controlled. In fact, this configuration only measures the half-cell related to the working electrode, neglecting the contribution of the counter electrode.

For stand-alone, photoelectrochemical water-splitting devices that are measured in a two-electrode configuration, the benchmark efficiency parameter adopted is the solar-to-hydrogen (STH) efficiency, which is defined as the ratio between the output chemical energy stored in the evolved hydrogen gas and the solar energy input.

$$\eta_{STH} = \frac{r_{H2}[mol/s] \cdot \Delta G^0[J/mol]}{P_{sun}[mW/cm^2] \cdot A[cm^2]}$$

The output power is calculated as the molar rate of hydrogen production r_{H2} times the molar change in Gibbs free energy for the reaction ΔG^0, whereas the input power is intended as the incident illumination power density P_{sun} times the active area of the photoelectrochemical device A. However, the same parameter cannot be employed to express the efficiency of a photoelectrochemical water-splitting device that is measured in a three-electrode configuration, since the behavior observed only describes the half-call and the single half-reaction involved.[74] Since three-electrode measurements are the most prevalent form of experimentation employed in the field, recent works have introduced an adequate figure of merit for that experimental configuration, called ratiometric power-saved Φ_{saved}.[75,76] The ratiometric power-saved can be qualitatively defined as the advantage of employing an active photoelectrode to drive a given water-splitting half-reaction instead of a dark electrode, for the current value measured at the photoelectrode maximum power point. To calculate the ratiometric power-saved under the most conservative assumptions, the dark electrode adopted in comparison is an ideally non-polarizable dark electrode, meaning that it acts as an ideal diode with a voltage threshold equal to the potential of the appropriate half-reaction. The ratiometric power-saved Φ_{saved} adopted in this work is calculated as the difference between the dark electrode voltage V_{dark} and the photoelectrode voltage at the maximum power point V_{MPP}, multiplied by the photocurrent density at the maximum power point J_{MPP}, divided by the incident illumination power density P_{sun}.

$$\Phi_{saved} = \frac{(V_{dark}[V] - V_{MPP}[V]) \cdot J_{MPP}[mA/cm^2]}{P_{sun}[mW/cm^2]}$$

This figure of merit is employed for both the photoanodes and photoelectrodes characterization, using a positive photocurrent sign and the oxygen evolution potential of 1.23 V$_{RHE}$ as the dark electrode potential for the former case, whereas

a negative photocurrent sign and the hydrogen evolution potential of 0 V_{RHE} as the dark electrode potential for the latter case.

3.4 Electrochemical Measurements

The electrochemical measurements are performed connecting the electrode of the electrochemical cell to a potentiostat (Autolab PGSTAT 30) and controlled with a dedicated software. The potentiostat measures and controls the electrochemical behavior of the connected system, performing different procedures that allows to assess the properties and probe the performances of the working electrode.

3.4.1 Linear Sweep Voltammetry (LSV)

Linear sweep voltammetry is an electrochemical procedure that measures the electrical current flowing through the working electrode while the applied potential is linearly swept in time with a fixed scan rate. For the photocathode measurements, the potential sweep starts at the open circuit potential of the device and move towards cathodic potentials, usually stopping a few hundred millivolts after the hydrogen evolution potential at 0.00 V_{RHE}. Concordantly, the potential sweep for photoanode measurements starts at the open circuit potential of the device and move towards anodic potentials, usually stopping a few hundred millivolts after the oxygen evolution potential at 1.23 V_{RHE}. The voltage scan rate is another important parameter, since it influences the output current of the measurement. The magnitude of the measured current is proportional to the flux of ions towards the working electrode. When polarized, the working electrode develops a diffusion layer above its surface where the concentration of ions is

severely lower than the bulk concentration in the bulk electrolyte. As the size of the diffusion layer grows, the ions flux towards the electrode lowers and so does the measured current. When the scan rate is low, the working electrode spends more time polarized at a given potential and the diffusion later grows larger, thus resulting in a lower measured current. This occurs when the reaction at the electrode surface is considered reversible with respect of the potential scan rate, meaning that the charge transfer occurs with a faster time scale than the change of potential. When the reaction is slower than the potential scan rate, it is considered quasi-reversible or irreversible and the entire shape of the photocurrent changes with the potential scan rate. Peaks or slopes in the current profile are shifted to higher potentials, as the reaction equilibrium is not established fast enough in comparison with the potential scan rate. All the measurements in this work are performed with a scan rate of 20 mV·s^{-1}, which is the usual value adopted for photoelectrochemical water-splitting, since it provides enough while remaining in the reversible reaction regimen and the measured current is not limited by the kinetics of the reactions. Since the analyzed devices have a photoactive response, the linear sweep voltammetry measurements are performed under chopped illumination – with the light source shuttered closed for fixed amounts of time – in order to present both the response of the photoelectrode with and without solar light illumination, respectively called the photocurrent and the dark current. The dark current of photoelectrochemical system need to be practically zero – in the order of few microamperes – as it corresponds to the leakage current of an ideal photodiode. If the dark current exceed the few microampere threshold, it means that chemical redox reactions are occurring without any photon absorption or there is some short-circuit within the device structure. The first reason is related to the unwanted degradation of the materials in the solution, whereas the second is attributed to defects in the

fabrication process or in the design of the architecture. Since the physical quantity measured by the potentiostat is a current, the recorded current values are divided by the active area of the working photoelectrode in order to obtain the respective current density values, which more accurately describes the yield of the devices and can be easily compared with other results present in literature.

Several important electrochemical parameters are identified within or extrapolated from the measured voltammograms. Since current does not flow between the working and the reference electrode due to a high impedance, when no potential is externally applied by the potentiostat the system in equilibrium at the open circuit voltage V_{OC}. As already mentioned, this voltage is chosen as the starting point for the linear sweep voltammetry measurements for all devices. As soon as all the electrical connection in the cell are completed and all the electrodes are placed in the electrolytic solution, it is necessary to wait a certain amount of time to ensure the system has reached its equilibrium point and the open circuit voltage is the correct and stable value. This amount of times depends on the material and design of the photoelectrode, but stay in the range of tens of seconds. When the cell is polarized by the potentiostat, photogenerated current starts flowing between the working and the counter electrode. The photocurrent onset potential V_{OP} is defined as the applied voltage where a photocurrent density of at least 10 µA·cm^{-2} first occurs in the measurement. Concerning the photocurrent, a frequently reported value is the photocurrent density obtained at the half-reaction potential, that is 0 V$_{RHE}$ for the photocathodes and 1.23 V$_{RHE}$ for the photoanodes. Furthermore, elaborating the linear sweep voltammetry data it is possible to plot the ratiometric power-saved Φ_{saved} as a function of voltage and thus extrapolate the maximum power point of the system.

$$\Phi_{saved}(V) = \frac{[V_{dark} - V] \cdot J(V)}{P_{sun}}$$

The graph shows the ratiometric power-saved values for all voltage-current density data points collected during the linear sweep voltammetry measurements; the curve maximum is the actual ratiometric power-saved figure of merit and the voltage and current density values of that maximum are respectively the maximum power point voltage V_{MPP} and the maximum power point current density J_{MPP}.

3.4.2 Cyclic Voltammetry (CV)

Similar to linear sweep voltammetry, cyclic voltammetry is an electrochemical procedure that measures the electrical current flowing through the working electrode while the applied potential is linearly swept in time with a fixed scan rate, back and forth between to voltage values for a given amount of cycles. The range where the forward anodic and the backward cathodic potentials are chosen can vary widely and depends on the intended purpose of the voltammetry and the material investigated. The purpose of cyclic voltammetry measurements is to highlight and identify redox reactions occurring between the working electrode and the electrolytic solution, measured as peaks in the current profile during the forward or backward potential scan. The cyclic scan is performed several times to monitor the trend of the current profile and the behavior of the material. Modification in the current intensity – both for the possible peaks or the general shape of the curve – are usually related to an irreversible modification of the material upon degradation within the electrolyte. In fact, cyclic voltammetry is a key measurement to probe the chemical stability of a given material within a certain potential range and with respect of the electrolyte composition and pH. As already detailed in Section 3.4.1, the potential scan rate has a strong influence on the values measured during a cyclic voltammetry and the value adopted in this

work is 20 mV·s^{-1}. The measurements are usually performed without any illumination on the device, as the inspected redox peaks occur due to the chemical reactions; however, when the reactions are mediated or activated by the photogenerated carriers, the device are illuminated with the solar simulator.

3.4.3 Chrono-Amperometry (CA)

Chrono-amperometry is an electrochemical procedure that measures the electrical current flowing through the working electrode at a fixed potential, as a function of time. The values of the fixed potential can be chosen arbitrarily, but usually are selected between representative values of interest for the measured device: the hydrogen evolution potential for the photocathodes, the oxygen evolution potential for the photoanodes – respectively 0 V_{RHE} and 1.23 V_{RHE} – or the maximum power point potential V_{MPP}, as extrapolated from the linear sweep voltammetry curves. The chrono-amperometry measurements are performed to probe the behavior of the photoelectrochemical system under continuous operation. A steady current profile over time means that the measured device is stable, whereas a degradation of the photocurrent yield is related to degradation phenomena. Depending on the materials and architectures probed, the time scale can vary from minutes to day. Similar to the linear sweep voltammetry measurements, the illumination is chopped at certain intervals in order to show the dark current, whose low value is a sign of good chemical stability and efficient structural design.

3.4.4 Incident-Photon-to-Current Efficiency (IPCE)

Incident-photon-to-current efficiency is an important diagnostic figure of merit for photoelectrochemical devices, that describes the number of photogenerated charges per number of incident photons as a function of the photon wavelength. This parameter describes the combined efficiency of the device in absorbing the incoming photons, converting the photon energy into an electron-hole pair, separating, extracting and transporting the photogenerated charges. The efficiency values are obtained measuring the current photogenerated by the device when illuminated by a monochromatic light, divided by the calibrated photon flux of the source at that specific wavelength. The procedure is carried out for all the different wavelength in a range of interest, obtaining the spectral profile of the efficiency. For the actual measurement, the solar simulator light is filtered with a monochromator (Applied Photophysics, 1200 lines·mm^{-1}, band-pass 10 nm) and the emitted spectral irradiance is measured with a calibrated silicon photodiode (Centronic OSD 7Q). The photocurrent density of the device illuminated with monochromatic light is recorded with the potentiostat, that operates the electrochemical three-electrode cell under a constant applied bias. The incident-photon-to-current efficiency is then calculated multiplying the spectral current density J_λ per $1240 V \cdot nm$ – a conversion factor obtained by the multiplication of Plank's constant h and the speed of light c – and dividing the obtained numerator by the calibrated spectral power density P_λ times the pertinent wavelength.

$$IPCE = \frac{J_\lambda[mA \cdot cm^{-2}] \cdot 1240[V \cdot nm]}{P_\lambda[mW \cdot cm^{-2}] \cdot \lambda[nm]}$$

From this measured efficiency parameter, a secondary figure of merit can be calculated, called the absorbed-photon-to-current efficiency (APCE). This

parameter is obtained dividing the incident-photon-to-current efficiency spectral profile by the absorptance spectral profile of the photoactive material and thus describes the internal conversion efficiency of the device, removing the contribution related to photon absorption.

3.4.5 Electrochemical Impedance Spectroscopy (EIS)

Electrochemical impedance spectroscopy is a spectroscopic procedure that measures the frequency response of an electrochemical system. The output current of the system is collected upon application of sinusoidal potentials with different frequency values. The sinusoidal potential comprises a fixed component that is arbitrarily selected for the given measurement and a varying component with small amplitude, in order to remain within the boundaries of the perturbation theory. The impedance is then extrapolated by the potentiostat software as the complex ratio between the applied voltage and the measured current. The acquired data is usually plotted in two ways, the Nyquist plot and the Bode plots. The Nyquist plot is the graphic representation of a transfer function in polar coordinates, where the abscissa and ordinate axis are respectively the real and the imaginary parts of the impedance and each data point is a different sinusoidal frequency. The Bode plots are the graphic representation of a transfer function in Cartesian coordinates, where the abscissa is the sinusoidal frequency and the ordinate is either the modulus or the phase of the impedance. Since the extrapolated impedance is a complex function of frequency that describes the response of the measured electrochemical system, its raw representation is hard to read and advanced data treatment must be performed in order to extract useful information. The experimental data is fitted with a theoretical model that is constructed to accurately describe the real working system through a combination

of physical parameters. For electrochemical devices, the data is fitted using the equivalent circuit method, where physical aspects of the device – like interfacial layers, bulk transport and ion diffusion – are translated into electrical components, made of resistances and capacitors and arranged in series or in parallel. The electrochemical impedance spectroscopy measurements of this work use a sinusoidal amplitude of 20 mV and cover the frequency range of 0.01 Hz – 10 kHz.

3.5 Morphological & Structural Characterization

3.5.1 Scanning Electron Microscopy (SEM)

A scanning electron microscope (Zeiss SUPRA40) is employed to probe the morphology of the deposited samples on the micro- and nanoscale. Placed in high vacuum with a pumping system, the instrument generates an electron beam with energies between 0.2 – 40 keV using exploiting the thermionic emission of a heated tungsten filament. The electron beam passes through focusing condenser lenses and through deflector plates that are used to control and move the beam trajectory. After the final aperture, the electron beam impinges on the samples surface and interacts with the material. The topographical images used in this work are obtained elaborating the detected information from the secondary electrons, that are ejected from the sample due to the inelastic scattering interaction between the atoms of the material and the electrons of the beam. Imaging parameter like magnification and resolution are controlled by adjusting the electron beam properties like energy, focusing and distance of the sample from the aperture. In order for the instrument to operate properly and obtain worthy images, the probed samples must have a conductive substrate to be connected with the instrumental setup. Measured films are usually deposited on

conductive silicon substrates, but the TCO layers coating the glass substrates are conductive enough to produce detailed images. Top views are easily obtained imaging the surface of the samples, whereas cross-sectional views require to carefully cleave the samples in half and fit the now exposed internal surface toward the beam.

3.5.2 Transmission Electron Microscopy (TEM)

A high-resolution transmission electron microscope (JEOL 4000EX) is employed to probe the nanometric details of ultra-thin specimen of the deposited morphologies. Depending on the imaging mode employed, crystallography diffraction patterns can be also collected. Similar to scanning electron microscopy described in Section 3.5.1, an electron beam is here generated with a LaB_6 filament at 400 kV and collimated on the sample via condenser lenses and deflector planes. Instead of the secondary electrons emitted by the material upon scattering events, the image is formed by the transmitted electrons that have passed through the ultra-thin film and interacted with the material, collected with a sensing apparatus such as a CCD camera or a phosphorescent screen. In the bright field imaging mode – one of the most commonly used mode – the topographic image is formed by the different occlusion and absorption of the electrons by the material, in first approximation modelled like Lambert-Beer's law. Thickness of the film and atomic number of the atoms in the probed region influence the contrast of the image on the bright background field. In high-resolution measurements, the image is reconstructed from the different phases of the transmitted electrons through complex data manipulation and information retrieval techniques. In the diffraction imaging mode, the back focal plane of the focusing lens is place onto the detection apparatus instead of the imaging plane, thus collecting a diffraction pattern. This

imaging mode produce a pattern of dots for a single crystal specimen or a series of rings for an amorphous or polycrystalline material.

3.5.3 Atomic-Force Microscopy (AFM)

An atomic-force microscope (Agilent 5500) is employed to measure the surface morphology of thick samples with resolution in the order of fractions of a nanometer. Atomic-force microscopy is a type of scanning probe microscopy that uses a mechanical probe to interact with the sample surface and collect information about its morphology. The system is composed by a cantilever with a nanometric silicon tip at the extremity, that is placed in close proximity with the sample surface. Due to the electrostatic and van der Waals forces acting between the probing tip and the sample surface, the cantilever undergoes small deflections from its rest state, that can be quantitatively measured and reconstructed into a topographical image. The spatial displacement of the cantilever is measured using interferometry, optical levers or piezoelectric methods, depending on the instrumental setup. To avoid damaging the probing tip with a direct collision against the sample surface, an electronic feedback is usually adopted to maintain constant the force between tip and surface, correcting the height of the sample with a piezoelectric actuator to avoid any collision. The recording process is performed as a raster scan on a specified area, carefully moving the sample stage with other piezoelectric actuators. In this work, the measurement mode adopted is the tapping mode, where the cantilever is kept oscillating near its resonance frequency and the probed parameter is not the deflection of the cantilever but the change in oscillation frequency due to the interactions between the tip and the surface. The phase of the cantilever oscillation with respect of the driving signal can also be recorded and it is related to the energy dissipated by the cantilever

interactions at each oscillation cycle, containing useful information about the variation of surface properties.

3.5.4 X-ray Diffraction Spectroscopy (XRD)

An X-ray diffractometer (Bruker D8 Advance) is employed to perform crystallographic measurements on the samples, probing the crystalline growth of the deposited films. The acquired data give accurate information concerning the primitive crystalline cell of the material and the structural growth of the film. The instrument employs a cathode ray tube to generate X-rays from a copper target and then filters the emitted spectrum with a monochromator to obtain only the copper K_α radiation, corresponding to 1.54 Å of wavelength. The emitted radiation is collimated through slits and shined upon the sample surface, recording the intensity of the diffraction signal with an X-ray detector as a function of the incident angle θ. The signal acquired corresponds to a count rate of the diffracted contribution at each angle, resulting from the constructive interaction of the X-rays with the sample crystalline structure of the material, obtained only under a certain condition. The diffraction peaks occur when a multiple n of the exciting wavelength λ is equal to twice the interplanar distance between lattice planes d, times the sine of the incident angle θ, as per Bragg's law.

$$n\lambda = 2d\sin\theta$$

The measured peak pattern is compared with reference spectra present in crystallography databases to precisely assess the crystalline phase of the materials. Single peak analysis can be also performed, identifying the crystalline lattice plane generating each contribution with its correct Miller indexes, thus understanding the Bravais lattice of the material. The intensity of the peaks

relative to a standard isotropic material can be used to estimate the directional growth of the film along preferential crystalline directions.

3.6 Optical & Electronical Measurements

3.6.1 UV-Vis-nIR Spectrophotometry

The optical properties of the devices are assessed via transmittance and reflectance measurements, collected using a UV-Vis-nIR spectrophotometer (Perkin Elmer Lambda 1050) equipped with an integrating sphere. The integrating sphere allows to selectively and efficiently collect the diffuse component of transmittance and reflectance, which is especially conspicuous for high scattering films. The spectral range of measurement can be arbitrarily chosen within the instrumental wavelength range of 250 – 2000 nm, achieved via two different light sources. The broadband illumination is filtered by an internal monochromator and then shined on the sample with a single wavelength at a time. Depending on the sample position with respect of the detectors inside the sphere and the incoming light beam, the instruments record the transmitted or the reflected light. The total absorptance of the measured device is calculated using the optical relationship $A = 1 - T - R$, where T is the normalized total transmittance and R is the normalized total reflectance.

3.6.2 Kelvin Probe Force Microscopy (KP)

A Kelvin probe force microscope (KP Technology, KPSP020) is employed to measure the work function of the deposited materials and substrates. Kelvin

probe microscopy is a non-contact mode of atomic force microscopy, that operates in a similar way to tapping mode, only with the tip further away from the surface as it oscillates widely at its resonant frequency. In kelvin probe measurements, the cantilever acts as a reference electrode, forming a capacitor with the sample surface. A direct current voltage plus an alternating current voltage at the cantilever resonance frequency is applied between the tip and the surface, causing the cantilever to oscillate and thus create an oscillating capacitor. To obtain the work function, the resonant contribution of the electrostatic force between the tip and the sample surface is minimized towards zero. This condition is obtained when the applied direct current voltage is set equal to the contact potential difference, that is the difference between the work function of the tip and the material surface. The actual measurements require to calibrate the instrument using a material of known work function – like a clean gold surface with a work function of 4.8 eV – in order to assess the current work function of the probing tip. Once calibrated, the work function of the probe material is obtained subtracting the tip offset from the acquired contact potential difference.

Chapter 4: Results and Discussion

4.1 Quasi-1D Hyperbranched WO₃ Photoanodes

4.1.1 Introduction

Arrays of nanostructures with high aspect ratio and strong directional growth are grown via pulsed laser deposition (PLD) through a self-assembly process from the gas phase. These mesoporous films are successfully used as photoanodes for photoelectrochemical splitting of water, exhibiting an onset potential as low as 0.4 V_{RHE} and saturation current densities up to 1.85 mA·cm^{-2} at 0.8 V_{RHE}. While the saturation current is similar to the state-of-the-art values for WO₃ photoanodes, both the onset and saturation voltages are significantly lower than any other reported values. This peculiar features are attributed to the morphology of structure – called hyperbranched – and to its excellent optical and electronic properties.

4.1.2 Structural & Morphological Analysis

Based on previous works that successfully employ the PLD setup for the fabrication of nanostructured film of transition metal oxides,[77–82] the operational parameters for the photoanodes fabrication are herein optimized in order to obtain WO₃ films with the hyperbranched morphology. In order to highlight the inherent improvements of the hyperbranched structure in comparison to a less ordered configuration, two different types of samples are fabricated and

characterized for this study: hyperbranched WO_3 nanostructures (HYP) and hierarchical WO_3 nanostructures (HIE), similar structures that lack the enhanced long-range crystalline order and strong directional growth. The HIE samples are fabricated by slightly modifying the deposition operational parameters from the optimized value employed the growth of the HYP samples. Both morphologies share the distinctive tree-shaped growth that characterizes mesoporous nanostructured films fabricated via PLD with an intermediate background gas pressure (10 Pa in the case of WO_3) and a laser fluency of approximately 2 J·cm^{-2}.
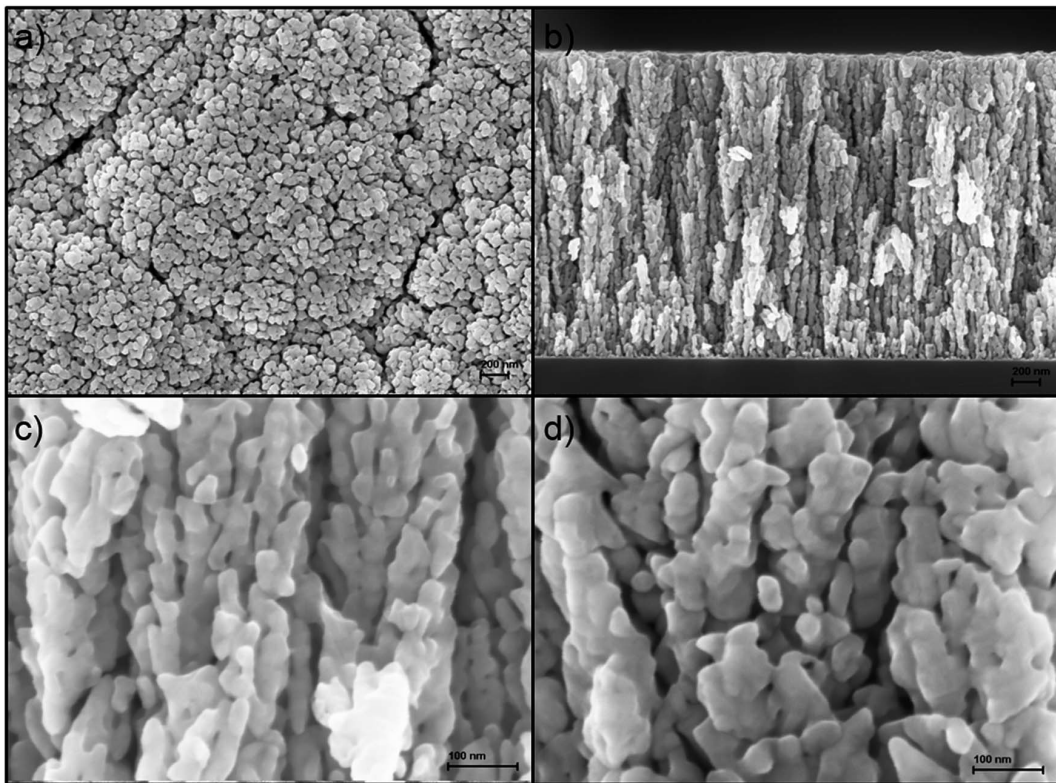
Figure 4.1 – SEM images of the top view (a) and cross-sectional view (b) of the nano-tree morphology. High-magnification SEM images of cross-sectional views for the HYP (c) and HIE (d) samples.

Top and cross-sectional SEM images (Figure 4.1a and b) show in detail these nano-tree structures, comprising a main stem perpendicular to the sample growth surface and numerous branches that develop throughout the stem height, the branches themselves having their own ramifications in a similar fashion. These

complex structures are defined within a conical envelope that forms a 15° − 20° angle with the main growth axis. The nano-trees are arranged in closely packed arrays that homogeneously cover the whole sample surface, resulting in a mesoporous film with percolative pathways in the order of 10 nm that travel through the entire structure thickness. High-resolution SEM images (Figure 4.1c and d) clearly show the differences between the HYP and HIE morphology: the hyperbranched structure displays longer crystallites arranged preferentially along the conical envelop around the main stem, whereas the hierarchical structure is characterized by smaller crystallites bound together in a less ordered fashion.
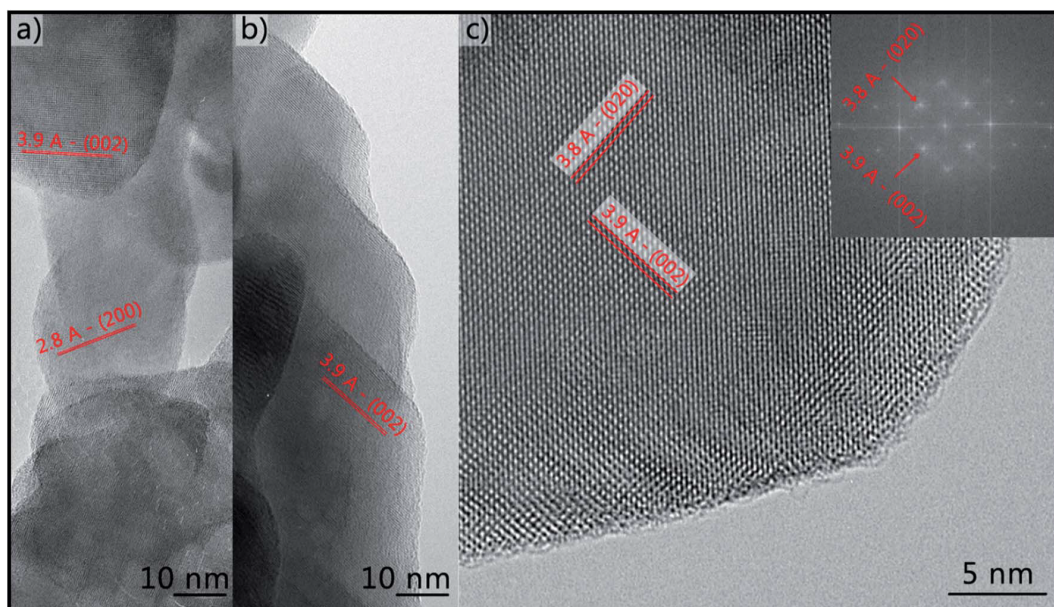
Figure 4.2 – High-resolution TEM images of the HIE (a) and HYP (b, c) samples. The HYP sample imaged from the [100] zone axis (c) shows high crystallinity and clean surface terminations. The Fast Fourier Transform of the lattice (c, inset) highlights the main lattice spacing.

High-resolution TEM images (Figure 4.2a and b) display the preferential growth of the nano-trees branches along the *b* direction of the primitive cell – corresponding to the crystallographic [020] direction – and highlight the lattice fringe spacing of the crystals that matches the parameters for monoclinic γ-WO$_3$. TEM image with further magnification (Figure 4.2c) confirms the high degree of crystallinity that characterize the HYP morphology, with an extremely low density of defects and

well-defined lattice fringes up to the crystal edges. The fast-Fourier transform of the image (Figure 4.2c, inset) is performed to precisely measure the lattice spacing values and its clear pattern ratifies the assumptions of high crystallinity and low defect density.
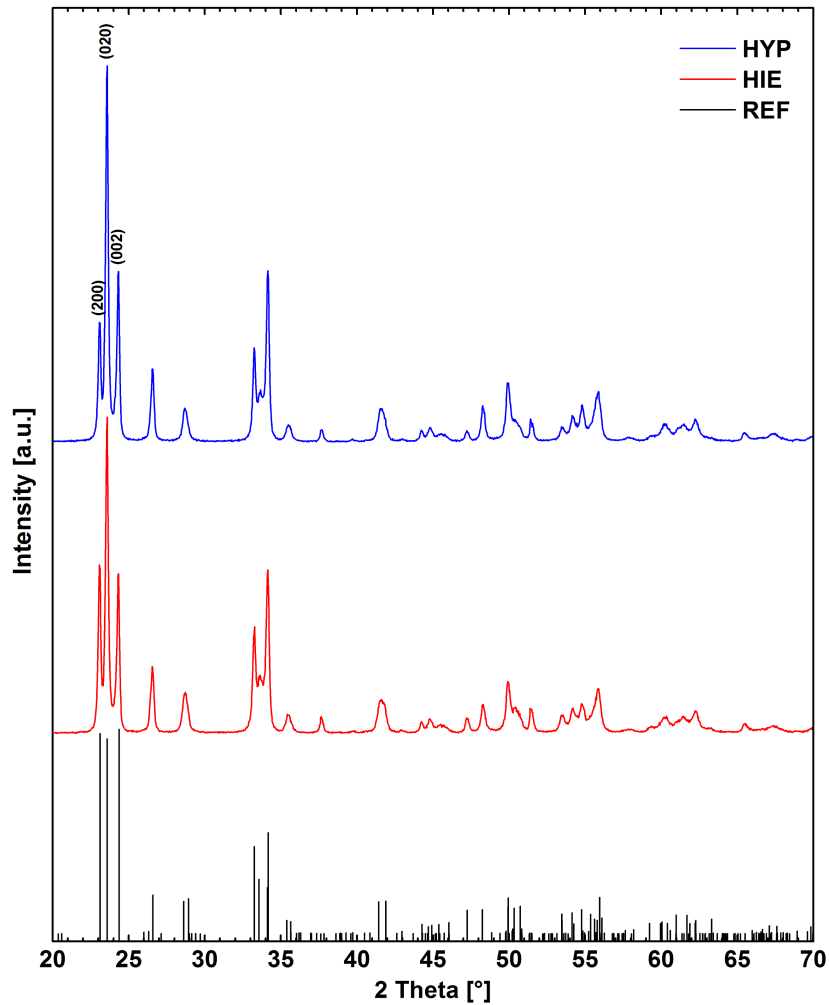
Figure 4.3 – XRD spectra of the HYP and HIE samples, together with the reference peaks of monoclinic WO$_3$ powder. The three, main crystallographic direction [200], [020] and [002] are reported.

The preferential growth along the [020] direction hinted by the TEM images is experimentally confirmed by the XRD measurements (Figure 4.3) performed on the HYP and HIE samples, together with a monoclinic WO$_3$ powder – labelled REF – as a reference for pristine WO$_3$ without nanostructuring. Monoclinic WO$_3$ has its three main diffraction peaks – the peaks related to the three main crystallographic

directions of the primitive cell – in region between 23° and 25° of incident angle. For the REF sample, the intensity of these three peaks is almost identical and normalized to the single unit, suggesting a full isotropic growth of the crystallite in the powder, as predictable for a pristine reference. On the contrary, the nanostructured films show a stronger signal for the (020) peak, with a normalized intensity with respect of the adjacent (200) peak equal to 1.9 for the HIE sample and 3.4 for the HYP sample. A stronger contribution from the (020) peak implies that a high number of [020] crystallographic planes are probed during the measurements and therefore the crystallites have a preferential growth along that axis. This effect is already present in the hierarchical samples due to the directional shape of the nano-trees, but it is even more stressed for the hyperbranched ones, as the high degree of crystallization provides additional long-range order along the main growth axis. The quasi-1D morphology of these nano-tree structures amounts to an effective compromise between 1D nanostructures – like nano-rods and nano-wires – with a strong directional growth that helps charge transport and dense nanoparticle films with a high optical density and photocurrent yield despite the internal defectiveness.
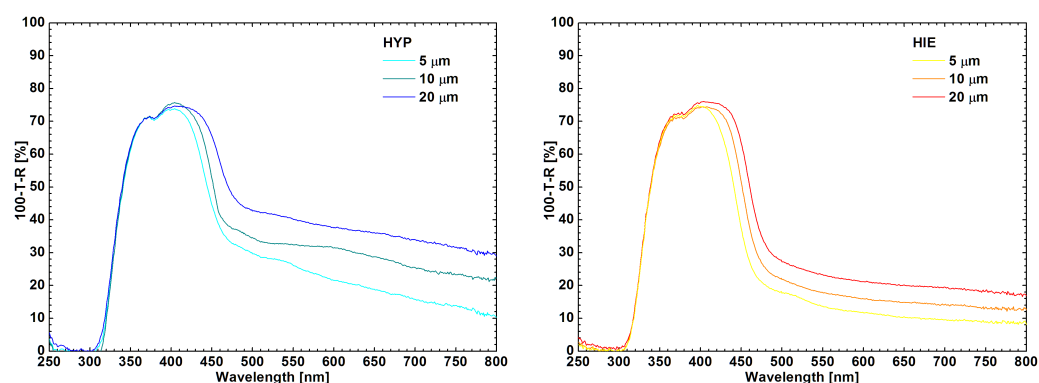
Figure 4.4 – Absorptance spectra of the HYP (left) and HIE (right) samples as a function of film thickness. The spectra are obtained removing the contribution of the FTO-covered glass substrate.

The optical properties of photoanodes fabricated with both HYP and HIE morphologies are probed as a function of film thickness. The transmittance

spectra T and reflectance spectra R of the samples are collected using a spectrophotometer with an integration sphere and then elaborated to obtain the absorptance spectra A (Figure 4.4) using the formula $A = 100 - T - R$. Following the same procedure used for the photoelectrochemical characterization, the optical measurements are performed illuminating the devices from the substrate sides and thus the contribution of the nanostructured WO_3 film alone is obtained by subtracting the spectrum of a clean FTO-covered glass from the experimental data. The 2-mm-thick glass substrate is enough to completely absorb all photons in the near-UV range, thus screening the absorption of the WO_3 film from photons below 320 – 330 nm of wavelength. The compact FTO film accounts for the small dimple in the absorption curve present below 380 nm, corresponding to the band-edge cutoff of a semiconductor with an optical band-gap energy of approximately 3.2 eV, an estimated value in good accordance with the literature. The WO_3 films alone absorb photons in the visible spectral range up to 470 nm, equal to the optical band-gap energy of 2.65 eV proper for the monoclinic phase. The absorptance below the band-edge cutoff is nearly the same for all the samples regardless of morphology and thickness and its value reaches approximately 70% for the sole WO_3 film and 90% with the substrate contribution. This implies the total absorption of the available photons, since over 8% of the incident light is reflected at the two glass interfaces, in accordance with Snell's law. On the other hand, absorptance near the band-edge cutoff increases with increasing thickness for both morphologies to approach full absorption values. This behavior is attributed to the indirect nature of WO_3 optical band-gap and the necessity of phonon-mediated absorption process for photons with an energy comparable to the material band-gap. For photons with energies higher than the WO_3 optical band-gap it is possible to be absorbed without the contribution of energy from the crystal lattice, since the vertical transition is high enough to reach unoccupied

states in the conduction band. For photons with energies comparable to the WO_3 optical band-gap, the absorption phenomenon has to be phonon-mediated and the absorption rate near the band-edge is severely diminished, thus requiring higher material thicknesses to reach saturation of the optical density. In all the spectra is also present a significant absorption tail that starts from the WO_3 band-edge cutoff and reach into the infrared range. This abnormal contribution – since it is related to any physical absorption event – is attributed to incident photons lost by the measuring setup that cannot fully collect light scattered at very high angles. The constant part of the absorption tail is due to the FTO-covered glass substrate, whereas the part dependent on morphology and thickness is due to the WO_3 film. Both hyperbranched and hierarchical nanostructures have strong light-scattering properties, as the sub-micrometric crystallites comprising the nano-trees act as efficient scattering points for light with a comparable wavelength. This feature is exploited to increase the light path length within the film and thus the overall optical density of the device within its absorption range.

4.1.3 Electrochemical Properties & PEC Performances

The photoelectrochemical characterization of the working photoanodes is performed in a three-electrode configuration, using a 1M of sulfuric acid solution (pH ≈ 0) as the aqueous electrolyte, a Pt coil as the counter electrode, an Ag/AgCl in saturated KCl as the reference electrode and the photoanode illuminated from the substrate glass side as the working electrode. The potential in the graphs is referred to the reversible hydrogen electrode (RHE) for the sake of comparison and clarity.
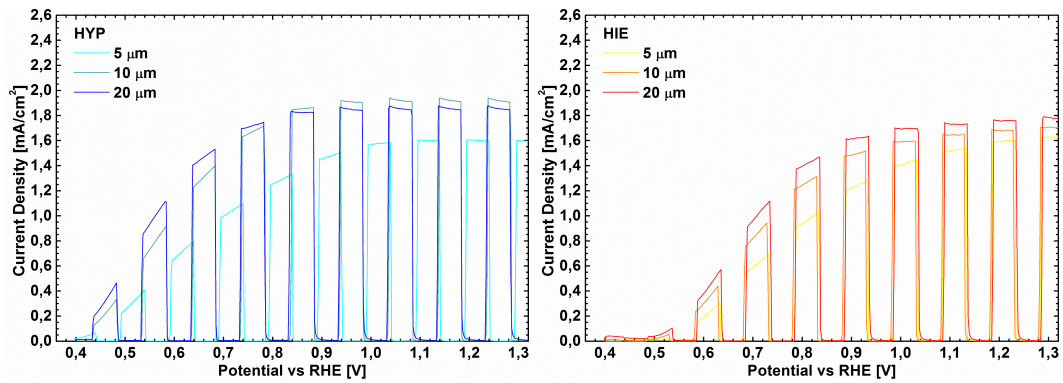
Figure 4.5 – LSV curves of the HYP (left) and HIE (right) samples as a function of film thickness, performed under chopped AM1.5 solar light in a 1 M sulfuric acid solution at pH 0.

Linear sweep voltammetry (LSV) curves are collected for both the HYP and HIE samples as a function of film thickness (Figure 4.5), scanning the potential range from the open circuit voltage V_{OC} of each sample up to 1.4 V_{RHE} and chopping the illumination every 500 mV of scan in order to present also the dark current of the devices and the light-dark transitions. The saturation photocurrent for both morphologies increases with the film thickness and reach its maximum value for the 20-μm-thick samples. The HIE one achieves a photocurrent of 1.77 mA·cm^{-2} with an applied bias of 1.1 V_{RHE}, whereas the HYP one reaches 1.85 mA·cm^{-2} with a lower applied bias of 0.8 V_{RHE}. The saturation currents of the two morphologies only differ by a small amount, while the photocurrent slope profile for the HYP samples is consistently shifted of 100 – 150 mV towards lower potentials with respect of the less optimized morphology, with a photocurrent onset potential of 0.4 V_{RHE} for the HYP samples and 0.5 V_{RHE} for the HIE ones. In order to probe the chemical stability of WO_3 under working conditions and confirm the non-transitive nature of the low potential photocurrent yield, an uninterrupted chronoamperometry measurement at 0.45 V_{RHE} is performed on the 20-μm-thick HYP device while immersed in the pH 0 sulfuric acid electrolyte (Figure 4.6). During the first five minutes, no illumination is provided and the dark current of the photoanode is collected. The constant values below the microampere threshold

confirm that no parasitic chemical reactions occur when the photoanode is polarized while immersed in the electrolytic solution. As the device is illuminated with the solar simulator, the photocurrent density immediately rises and matches the same value reported in the linear sweep voltammetry curve (Figure 4.5 left) for the selected applied bias. As the measurement continues, the photocurrent density shows no sign of degradation even after hours of uninterrupted photoanode operation. This result confirms the inherent stability of WO_3 while operating in acidic environments and under anodic biases.
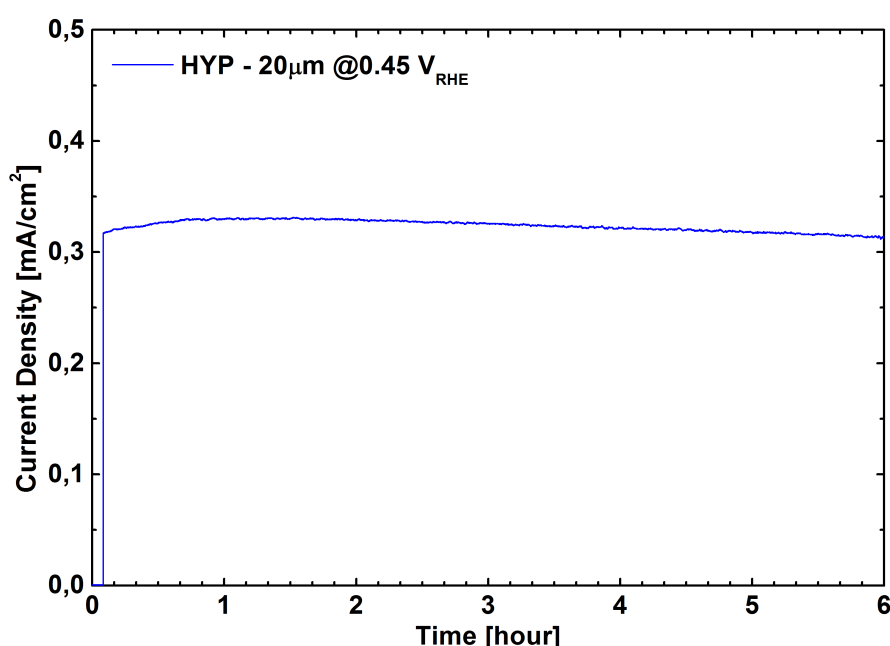
Figure 4.6 – Chronoamperometry curve of the 20-µm-thick HYP device, performed at 0.45 V_{RHE} under AM1.5 solar light in a 1 M sulfuric acid solution at pH 0. During the first five minutes no illumination is provided and the measured photocurrent density correspond to the dark current.

The photocurrent yield of a photoelectrode is related to its absorption and conversion efficiency. Since absorptance graphs (Figure 4.4) show no significant variance between the two morphologies, the difference must reside in the charge conversion efficiency of each morphology. To probe this photoelectrochemical property, incident-photon-to-current (IPCE) measurements are performed on both the HYP and HIE samples as a function of film thickness (Figure 4.7), in the

same three-electrode configuration as the LSV measurements and with an applied bias of 1 V_{RHE}, so that all measured samples are in the saturation plateau of their photocurrent curve.
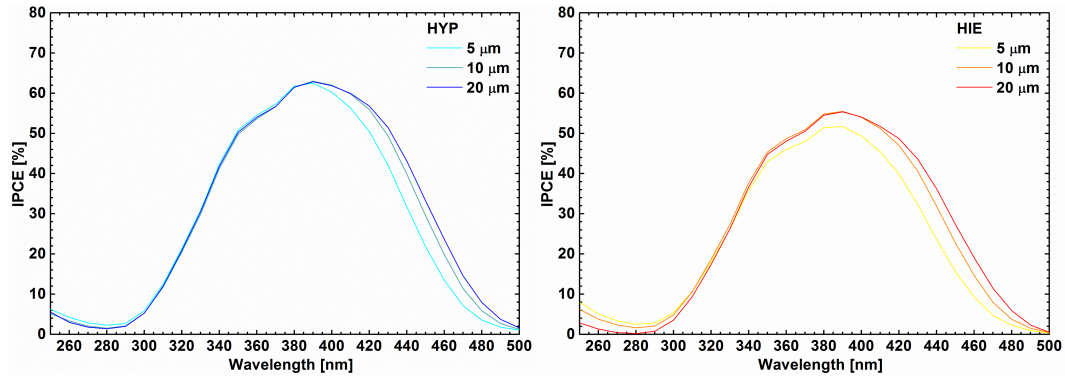
Figure 4.7 – Incident-photon-to-current (IPCE) curves of the HYP (left) and HIE (right) samples as a function of film thickness, measured with an applied bias of 1 V_{RHE}.

The spectral profile of the IPCE curves shows an onset of photon conversion approximately at 500 nm and a maximum around 400 nm, for a peak value of conversion efficiency equal to 56% and 64% for the HIE and HYP samples respectively. Conversion efficiency in the spectral range around the band-gap energy increases with sample thickness, following the same trend of light absorption. Thicker samples have an enhanced optical density and improved light-harvesting properties thanks to internal scattering, thus achieving higher values of photon conversion to photogenerated charges, especially for energies near the band-edge cutoff. The absorption and conversion improved performances are not hindered by charge transport losses related despite the increased thickness, thanks to the employed nano-tree morphology.
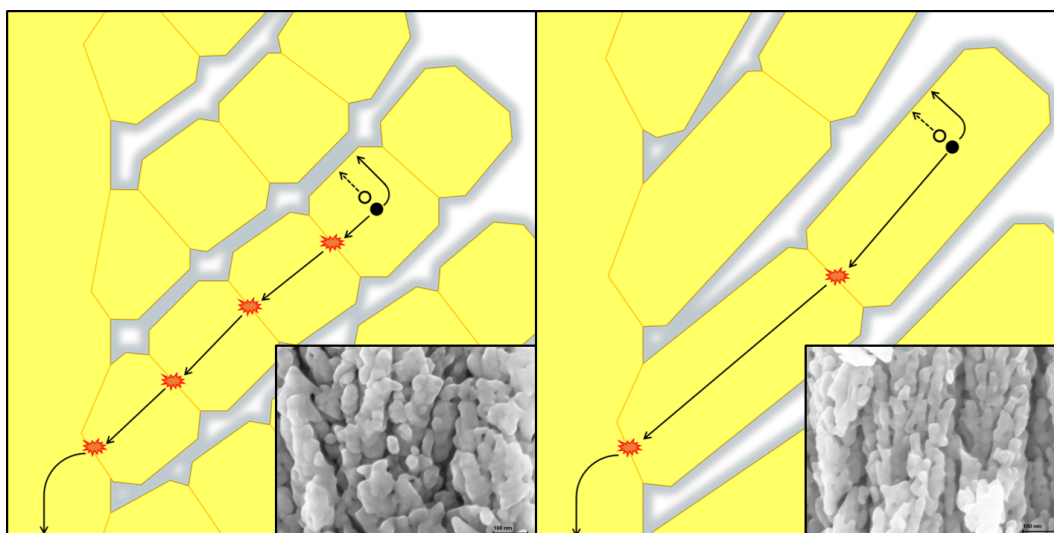
Figure 4.8 – Schematic of the electron (full dot) and hole (empty dot) extraction process within the nano-tree structure, with the different crystallinity of the HIE (right) and HYP (left) morphology.

For compact nanoparticle films, thick samples benefit from high optical density and efficient light absorption, but the photocurrent yield is limited by transport-related issues, as the charges photogenerated in depth have a higher chance to undergo recombination events along the path. Both the hierarchical and hyperbranched morphologies – characterized by strong directional growth into quasi-1D structures – are capable of overcoming this detrimental effect by decoupling light absorption from charge diffusion and transport (Figure 4.8). Nano-tree arrays are mesoporous structures with fine percolation pathways separating the nano-branches, resulting in a high effective surface area of the photoanode in contact with the electrolyte. In this way, while photogenerated electrons have to travel through the entire length of the nano-tree to reach the FTO layer at the bottom and be extracted into the external circuit, photogenerated holes diffuse perpendicularly to the nano-branch axis, reach the material/solution interface and are injected into the electrolyte. Studies in literature have estimated the hole diffusion length for monoclinic WO_3 to be approximately 150 nm, which is one order of magnitude higher than the average crystallite width in both HIE and HYP nano-trees, thus leading to a rapid and efficient hole injection mechanism

that is not related to the thickness of the film. On the other hand, electron diffusion occurs along the growth axis of the nano-tree and nano-branch and toward the selective contact at the bottom, the effective diffusion distance related to the depth where the given photon is absorbed and charges are thence photogenerated. As illumination comes from the glass side of the sample, incoming photons are mainly absorbed in the spatial region within the first micrometers of the film and the majority of photogeneration thus occurs very close to the FTO interface. In this way, film thickness can be increase in order to improve the overall optical density of the device, without lengthening the effective diffusion length for the electrons photogenerated in the first spatial region and thus preventing losses in the overall conversion efficiency due to charge transport issues. The higher conversion efficiency of the HYP morphology in the whole spectral range of absorption and photogeneration is attributed to the improved crystallinity and long-range order of the structure. Bigger crystallites with a more ordered structure result in fewer grain boundaries and defects that are potential recombination centers for photogenerated electrons and holes. Normalizing the IPCE spectra with the effective absorptance of the device it is possible to obtain the absorbed-photon-to-current-efficiency (APCE) spectra, that express the amount of net absorbed photon converted into photogenerated charge. The 20-μm-thick hyperbranched photoanode displays an APCE peak value of 86%, to further restate the optimal performance of the optimized morphology in terms of charge generation and injection (Figure 4.9).
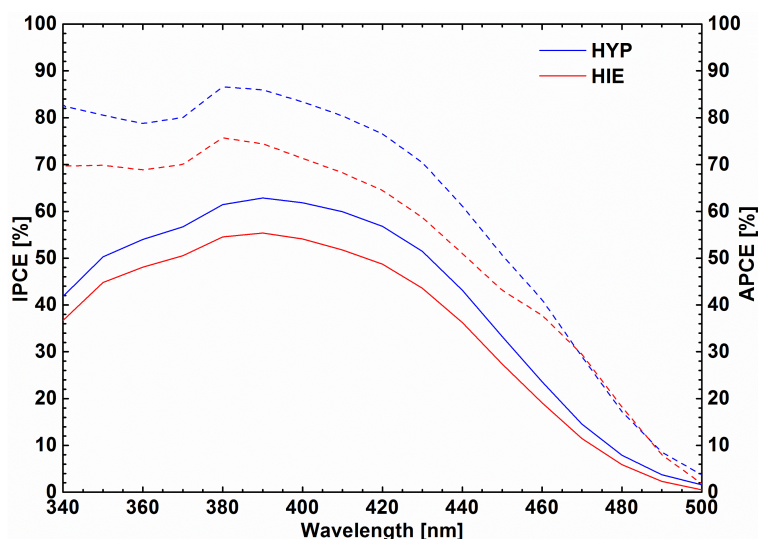
Figure 4.9 - IPCE (solid) and APCE (dashed) spectra of the 20-μm-thick samples of both the HYP and HIE morphology, measured with an applied bias of 1 V_{RHE}.

As the saturation photocurrent yield is related to the conversion efficiency at high potential, the early onset potential and overall low-voltage current profile of the HYP samples is related to the charge transport, charge recombination and charge accumulation properties of the optimized morphology. These properties are extracted from the electrochemical impedance spectroscopy (EIS) measurements, performed on both HIE and HYP samples of different thickness, to better understand the benefits of thick, hyperbranched nanostructured films.
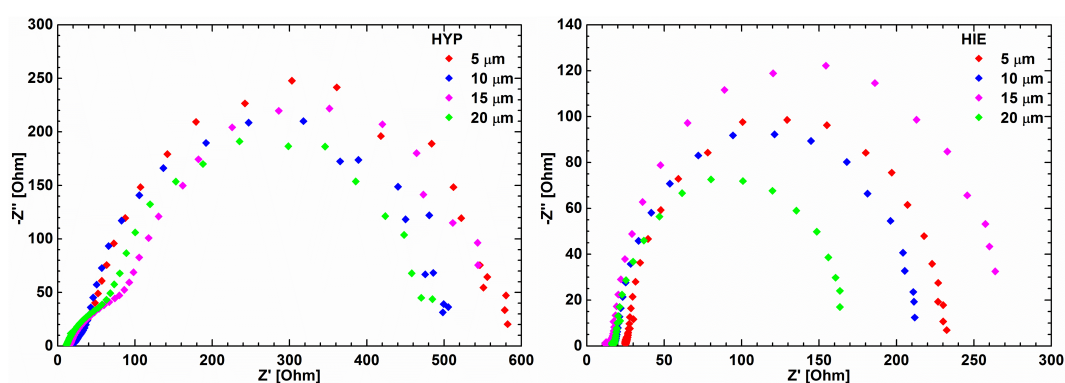
Figure 4.10 – Nyquist plots gathered from the EIS measurements of the HYP (left) and HIE (right) samples as a function of film thickness, performed with an applied potential of 0.7 V_{RHE}.

To extract the electrochemical parameter used in the following discussion, the Nyquist plots (Figure 4.10) obtained via EIS need to be fitted with a theoretical model that correctly describes the electrical behavior of the working device, called equivalent electrical circuit. The equivalent electrical circuit (Figure 4.11a) employed to model the WO_3 nanostructures is based on previous studies by Bisquert group on mesoporous transition metal-oxide photoanodes working in aqueous electrolytes. [83–91]
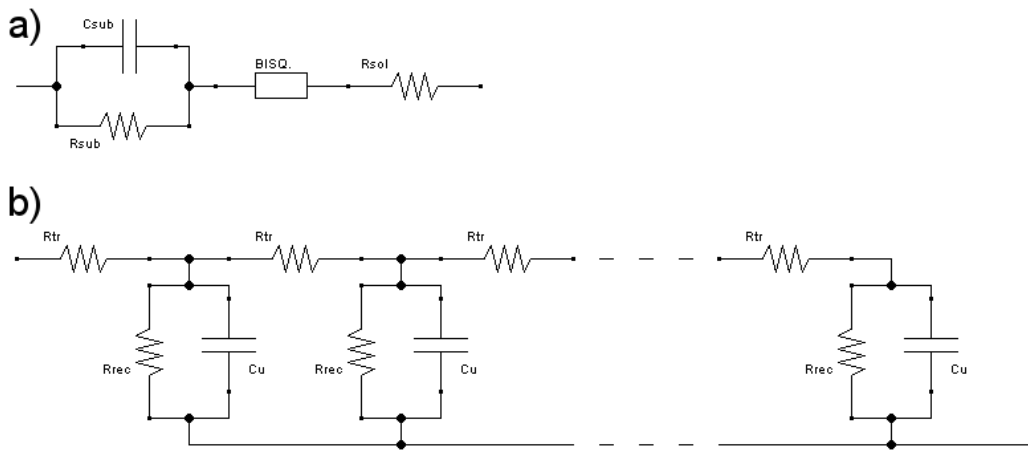
Figure 4.11 – Diagram of the electrical equivalent circuit (a) employed for EIS data fitting with a detailed exploded view (b) of the "Bisquert transmission line".

The electrochemical parameters that describes the WO_3 nanostructure are all condensed in the "Bisquert transmission line" (Figure 4.11b) and are the charge transport resistance R_{tr}, the charge recombination resistance R_{rec} and the chemical capacitance C_μ.
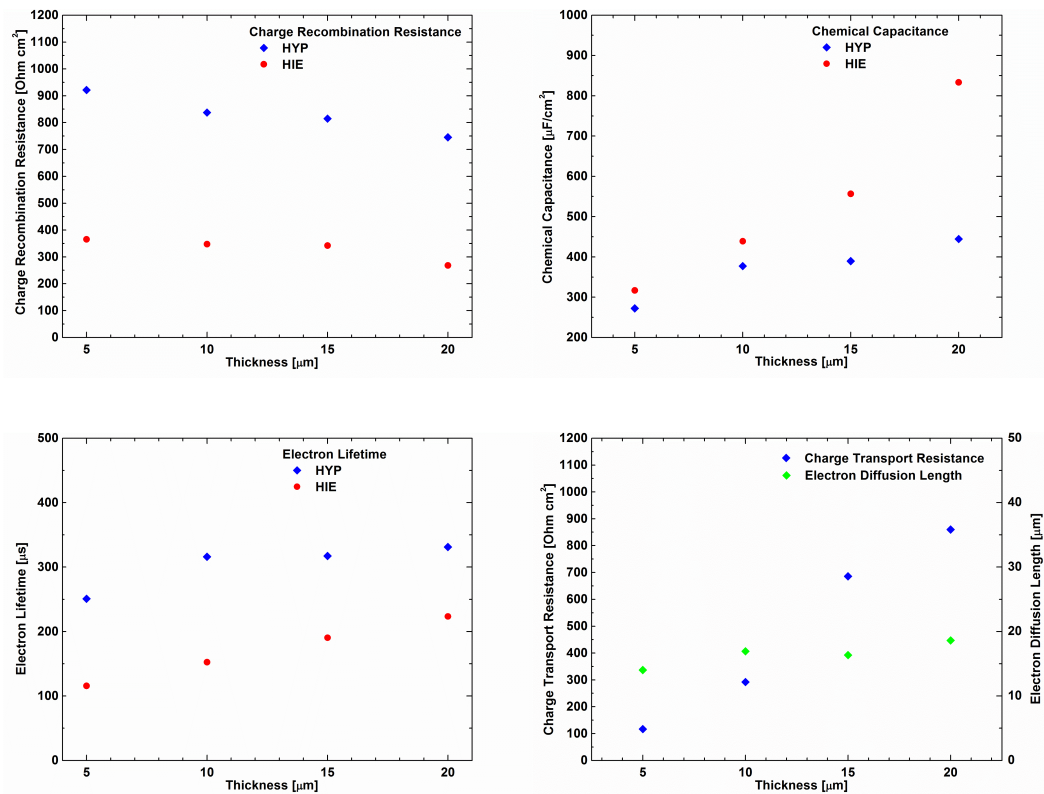
Figure 4.12 – Electrochemical parameters extracted from EIS measurements for HYP and HIE samples as a function of thickness: charge recombination resistance (top-left), chemical capacitance (top-right) and electron lifetime (bottom-left). Charge transport resistance and electron diffusion length (bottom-right) are shown only for the HYP samples.

Charge recombination resistance R_{rec} describes the kinetics of the charge-transfer process in which photogenerated electrons recombines with surface states at the photoanode/electrolyte surface. The high charge recombination resistance in the HYP samples (Figure 4.12 top-left) indicates that this process is hindered by the reduced amounts of photoanode/electrolyte interfaces and by the increased recombination path length due to the increased crystallites size. Since the average crystallite size does not change with the height of the nano-trees they compose, charge recombination resistance is almost constant with the film thickness, regardless of morphology. The second parameter in the analysis, chemical capacitance C_μ is related to the amount of trap states below the conduction band. Both morphologies display a quasi-linear trend of the chemical capacitance value versus the film thickness (Figure 4.12 top-right), with a higher slope for the HIE

samples. The density of trap states for a given type of material is fixed and the amount of trap states is proportional to the volume of the film: since a thickness increment in mesoporous film does not imply a proportional increment in volume, the chemical capacitance trend is quasi-linear and sub-proportional with thickness. Between the two morphology, the higher values of the HIE samples suggest a more defective crystal lattice of the nano- branches due to a less crystalline structure compared with the HYP samples. Electron lifetime τ_n is a derived parameter calculated as the product of charge recombination resistance R_{rec} and chemical capacitance C_μ and it describes the persistence of photogenerated electrons in the conduction band (Figure 4.12 bottom-left).

$$\tau_n = R_{rec} \cdot C_\mu$$

The extent of this persistence is governed by two distinct phenomena: the process of trapping and de-trapping, where electrons movement is delayed and their presence in the conduction band is prolonged (process associated to chemical capacitance C_μ parameter) and the recombination process, where electrons travel toward recombination centers at the photoanode/electrolyte interface (process associated to chemical capacitance R_{rec} parameter). Since electron lifetime τ_n is the product of two experimental parameters with opposing effects on the charge transport properties, its interpretation can be somehow misleading without the correct premises. High charge recombination resistance is desirable as it hinders the electron diffusion towards recombination centers, actual increasing the electron lifetime in the conduction band. On the other hand, high chemical capacitance means more trap states where electrons can undergo the trapping–detrapping process, effectively prolonging the electron lifetime in the conduction band, but actually just delaying electron movements and thus reducing the charge transport efficiency in the structure. In the end, electrons photogenerated in the HYP samples benefit from a longer lifetime than those in the HIE samples, but the

actual difference in transport efficiency is even greater as the hyperbranched morphology benefit from both low recombination and low trapping-detrapping chances. Charge transport resistance R_{tr} represents the resistance felt by the electrons that have to travel through the entire height of the nano-tree and – in first approximation – it increases with film thickness (Figure 4.12 bottom-right). This parameter has been extrapolated only for the HYP samples since the Nyquist plots of the HIE samples present artifacts in the high frequency region. Electron diffusion length L_n for the HYP samples is calculated using the two resistance parameters and the film thickness L.

$$L_n = L \sqrt{\frac{R_{rec}}{R_{tr}}}$$

The obtained values for electron diffusion length are constant with the film thickness, as expected for an intrinsic material property, only related to the type of morphology in analysis. The average value is 17 μm, in good agreement with the experimental data gathered with the LSV measurements, where the maximum photocurrent values starts to saturate for a comparable film thickness. Overall, the nanostructure with higher crystallinity and improved long-range order benefits from efficient electron and hole transport and extraction, thus achieving higher photocurrent with lower applied biases. The amount of grain boundaries and defects in the crystal lattice plays a key role in the photoelectrochemical performances of the overall device, especially in the low-voltage range. Reducing the voltage required to extract a photocurrent is one of the main way to improve the ratiometric power-saved ϕ_{saved} (Figure 4.13).
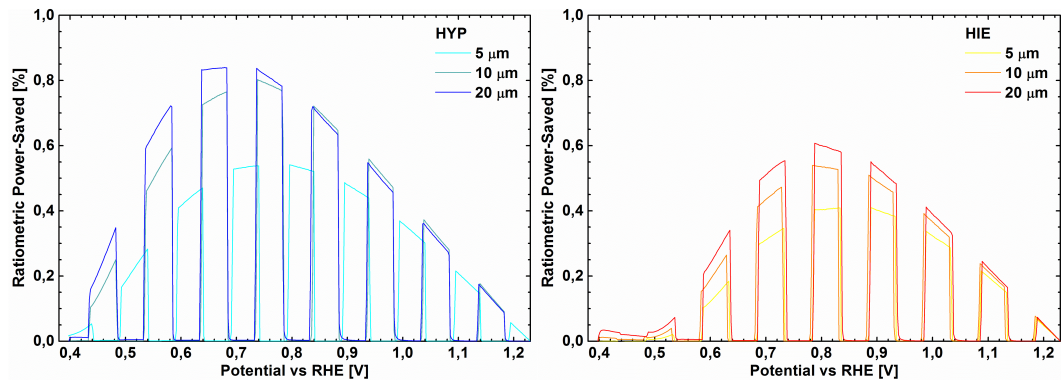
Figure 4.13 – Ratiometric power-saved curves of the HYP (left) and HIE (right) samples as a function of thickness, showing the peak of the maximum power point.

A possible synergistic mechanism that contributes in lowering the voltage of the photocurrent profile is the improved catalytic behavior of the lateral facets of the WO_3 monoclinic crystallites that form the nano-trees.[92] The [200] and [002] crystalline surfaces have an overpotential towards water oxidation that is 50-60 mV lower the overpotential of the [020] surface and directional growth of the HYP and HIE develops elongated crystallites along the crystalline *b* axis, thus resulting in a preferential exposure of these catalytic surfaces to the electrolytic environment.

4.1.4 Conclusions

In summary, quasi-1D hyperbranched WO_3 nanostructures are obtained via pulsed laser deposition by optimizing the deposition parameters and are thence compared to a non-optimized hierarchical morphology. Both nano-trees structures present efficient light absorption in the visible range and high internal scattering that is exploited to enhanced photon collection near the band-edge cutoff. Morphological analyses highlight a high degree of crystallinity and an improved long-range order for the hyperbranched morphology. The benefits from

these features and the difference between the two configurations becomes more evident in the photoelectrochemical characterization: the best-performing samples of each morphology have a similar saturation photocurrent (1.77 mA·cm^{-2} for the HIE sample and 1.85 mA·cm^{-2} for the HYP sample), but the optimized hyperbranched structure has a photocurrent profile shifted by 100 – 150 mV towards lower biases, with an onset potential of 0.4 V$_{RHE}$ and a saturation potential of 0.8 V$_{RHE}$ (the hierarchical structure achieves an onset potential of 0.5 V$_{RHE}$ and 1.1 V$_{RHE}$ respectively).
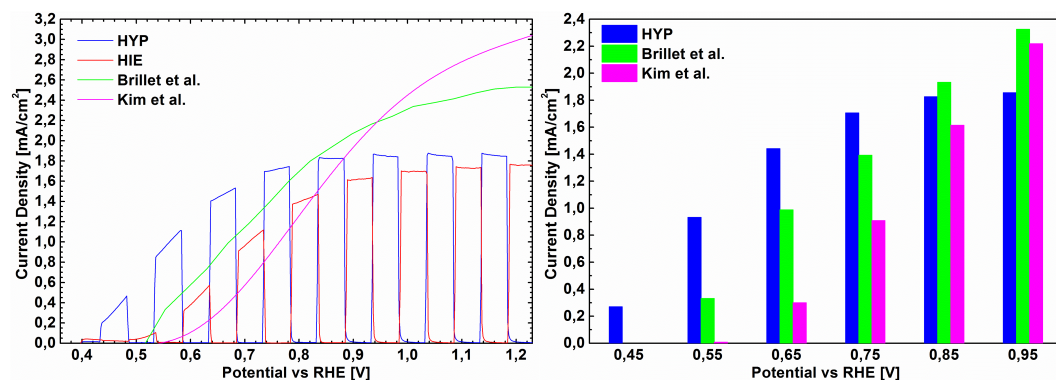
Figure 4.14 – LSV curves (left) of the HYP and HIE 20 mm-thick samples compared with the best devices from Brillet et al.[19] and Kim et al.[20] performed under similar experimental conditions. Histogram (right) of the photocurrent values at different applied voltages.

Comparison with state-of-the-art photoanodes in literature (Figure 4.14 left) shows that the photocurrent yield of quasi-1D mesoporous nanostructures is significantly lower than the record value at saturation, but the hyperbranched morphology gains a net performance advantage in the low-potential region (Figure 4.14 right). This feature is attributed to the crystallinity and long-range order of the morphology, with directional growth three times more pronounced than the reference monoclinic WO_3 powder. The elongated crystallites comprising the nano-trees have an average longitudinal size around 100 nm, resulting in a less defective nanostructure with fewer grain boundaries. Consequently, photogenerated electrons have a severely reduced recombination rate and can

efficiently travel toward the FTO contact along the film growth axis. At the same time, photogenerated holes need only to travel along the transversal size of the crystallites to reach the electrolytic interface, a path that is one order of magnitude shorter than their estimated diffusion length of 150 nm. Moreover, the preferential exposure of the [200] and [002] crystalline surfaces supposedly helps reducing the overpotential for water oxidation thanks to an improved catalytic effect.

4.2 Amorphous WO$_3$ Layer for Hybrid Organic Photocathodes

The use of polymers as photoactive material for solar generation of energy has been widely studied and demonstrated in the field of organic photovoltaics (OPV), suggesting that better performances can be achieved by coupling the organic semiconductor with interfacial layers to efficiently extract charges. The same concept applies for hybrid organic photoelectrochemical (HOPEC) applications, with the selective contacts (hole-selective layer and electron-selective layer) that need to satisfy the optoelectronic requirements identified for OPV as well as the additional set of electrochemical and photoelectrochemical constrains shared by the standard PEC devices. The correct energy level alignment between the conduction and valence bands of the selective contacts with the HOMO and LUMO levels of the organic active material is fundamental to build a barrier-free potential that can separate and inject the photogenerated charges.[93] The capability to selectively inject only the correct type of charge, defined by the relative band position of both the p-type (CB > LUMO) or the n-type (VB < HOMO) interfacial layers in contact with the organic semiconducting polymer, is prime to reduce charge recombination and parasitic leaking currents.[94,95] Furthermore, selective

contacts need to be nearly transparent in the spectral range of absorption of the organic photoactive material, in order to avoid losses in the incident photonic flux and thus maximize photogeneration. Lastly, strong (photo)electrochemical stability is mandatory to perform efficiently and durably in the electrolytic environment where the devices operate.

As they adequately satisfy the aforementioned requirements, TiO_2 and its general sub-stoichiometric phase TiO_x are considered materials of choice in both PEC or HOPEC applications to cover the role of the ESL.[96,97] However, finding an appropriate material as HSL have been proven by research so far to be a much less straightforward task. In the following discussion, a compact layer of amorphous WO_3 deposited by reactive magnetron sputtering (rMS) is employed as an efficient HSL. The underlying idea, based on previous HOPEC photocathode architectures, is to exploit of the strong chemical stability of WO_3 to avoid degradation issues and achieve longer lifetimes under operation, while retaining adequate photoelectrochemical performances. A hybrid organic photocathode for photoelectrochemical water-splitting is herein fabricated employing a P3HT:PCBM blend as the photoactive material, positioned between an amorphous TiO_2 electron selective layer and an amorphous WO_3 hole selective layer in order to properly extract the photogenerated charges; a thin platinum layer covering the TiO_2 film at the interface with the electrolyte is deposited to improve the catalytic efficiency of the device. This photocathode architecture achieves a photocurrent density of 2.48 mA·cm^{-2} at 0 V_{RHE} and an onset potential of 0.56 V_{RHE}, together with a state-of-the-art operational activity of more than 10 hours, thanks to the improved stability of the amorphous WO_3 hole selective layer. These results open the perspective about photoelectrodes based on organic semiconductors and coupled with proper inorganic selective contacts as a sound new option for the efficient and durable photoelectrochemical conversion of solar energy into fuels.

4.2.1 Structural & Morphological Analysis

In the proposed photocathode architecture (Figure 4.15a), photon absorption occurs in the bulk heterojunction and the photogenerated excitons are separated in the blend at the interfaces between the donor polymer P3HT and the acceptor fullerene PCBM. The separated charges are thence driven towards the correct extraction interface thanks to the built-in potential provided by the selective contacts. Amorphous TiO_2 works as an electron selective layer (ESL) and drives electrons photogenerated in the bulk heterojunction towards the PCBM/TiO_2 interface, where they are selectively extracted. After travelling through the ESL thickness, they reach the TiO_2-Pt/electrolyte interface where they are consumed to reduce protons and perform the hydrogen evolution reaction. On the other side, amorphous WO_3 works as a hole selective layer (HSL), exploiting the hole-harvesting properties of the WO_3/P3HT bilayer, where an n-type semiconducting material with high work function (WF 5.0 eV) is coupled with a p-type conjugated polymer with lower ionization energy (IE 4.85 eV) in order to efficiently extract the hole carriers and repel the electron carrier, thus reducing the recombination process at the interface.[93]
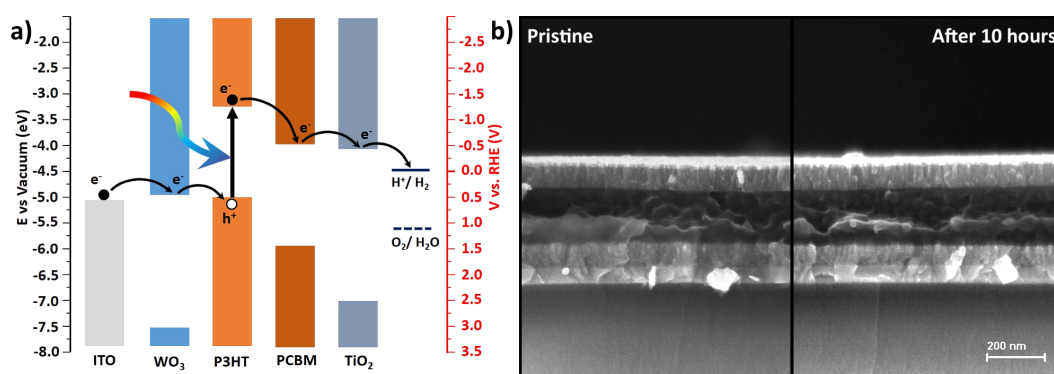
Figure 4.15 – Energy level diagram (a) of the hybrid organic photocathode with electron injection at the interfaces indicated with arrows. High resolution SEM cross-sectional images (b) of a hybrid organic photocathode collected before (right) and after (left) a 10-hour-long chronoamperometry measurement; in both images the individual layers composing the architecture are clearly recognizable, bottom to top: glass, ITO, a-WO_3 HSL, P3HT:PCBM BHJ, TiO_2 ESL and Pt.

The described architecture (Figure 4.15b) is realized coupling solution-processed fabrication techniques, such as spin coating of the organic photoactive P3HT:PCBM blend, and physical vapor deposition (PVD) techniques. Reactive magnetron sputtering is employed to deposit the amorphous WO_3 layer over the ITO-covered glass substrates, pulsed laser deposition (PLD) is used to fabricate the amorphous TiO_2 nanostructured layer over the polymer blend and pulsed DC magnetron sputtering covers the TiO_2 surface with a thin layer of catalytic platinum. Particular care is put in the PLD process, in order to achieve soft-landing regimes[98] during the deposition of the TiO_2 layer on top of the bulk heterojunction, in order to preserve the polymeric semiconductors functionalities and simultaneously maintain a good control over the stoichiometry[99] and nanostructuring of the oxide. Photocathodes with an increasing thickness of the amorphous WO_3 hole selective layer are fabricated, in order to probe the parametric effect on the overall device performances.
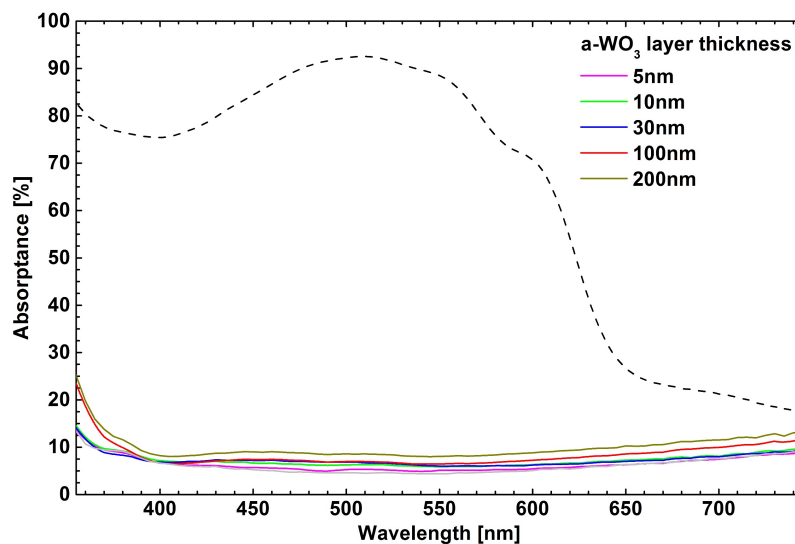
Figure 4.16 – Absorptance spectra of ITO-covered glass substrates with a different thickness of the amorphous WO_3 film. The absorptance spectrum of the P3HT:PCBM polymer blend (dashed line) is plotted for reference.

Since the device architecture is designed to be electrochemically measured with light illumination coming from the glass substrate side, the burden of transparency is held by the HSL. Spectrophotometer measurements are performed on ITO-covered glass substrates covered with a-WO_3 films of different thickness in order to assess to optical absorption of the composite layers beneath the photoactive polymer blend. The absorptance spectra (Figure 4.16) show that only 10% of the incident light in the spectral range of polymer absorption is collected by the underlying ITO/a-WO_3 layers and that there is no significant increase due to the thickness of the HSL. This suggests that the main absorption contribution is attributed to the ITO-covered glass substrate and thus confirms the high transparency of amorphous WO_3, even for a 200-nm-thick film. The high band-gap of amorphous WO_3 helps achieving the high transparency required, but also put an intrinsic drawback on the electronic properties of the material. In stoichiometric WO_3 the Fermi level is placed within the wide band-gap and far from the conduction band, resulting in an extremely low charge carrier density that severely hinders efficient electron injection from the hole selective layer into the bulk heterojunction. This drawback can be solved through an electrochemical intercalation process that induces protonated and partially reduced states within the WO_3 film. Since the material must remain electrically neutral, electrons are injected in the conduction band to compensate the protonated and partially reduced states, thus achieving an improvement in the charge carrier concentration by several orders of magnitude (approximately from 10^{18} cm^{-3} to 10^{21} cm^{-3}).[100]

4.2.2 Electrochemical Properties & PEC Performances

In order to precisely assess the electrochemical properties of the amorphous WO_3 film, a cyclic voltammetry measurement is performed on an ITO-covered glass substrate with a 100-nm-thick amorphous WO_3 film deposited on top. The cyclic voltammetry measurement is performed in the acidic electrolyte employed for the photoelectrochemical characterization of the full device and consists in 100 full cycles within the $0 - 1$ V_{RHE} potential range of photocathode operation. The resulting current profile (Figure 4.17a) shows neither peaks related to irreversible redox reactions, nor conspicuous drifts of the photocurrent values that might ascribe to a degradation or modification of the film, thus proofing the electrochemical stability of the material in the wide potential range of operational conditions.
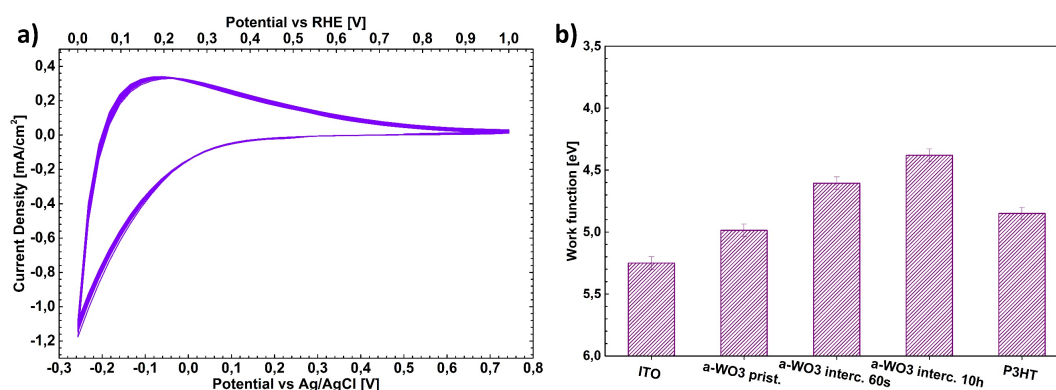
Figure 4.17 – Cyclic voltammogram (a) of the ITO/a-WO_3 (100 nm) sample, performed for 100 cycles with a scan rate of 20 mV·s^{-1} in a 0.1 M sulfuric acid solution at pH 1.37. Work functions (b) measured by kelvin probe force microscopy of the ITO/a-WO_3 (100 nm) sample, performed on the device before and after electrochemical intercalation (reversible process after 60 seconds and irreversible process after 10 hours); the measured work functions of the ITO film (after Oxygen Plasma Cleaning treatment) and of the P3HT polymer are shown for comparison. The value of the work function are referred to the vacuum energy.

The different values of current between the forward and backward scan in the cyclic voltammogram are attributed to the reversible process of protons intercalation and de-intercalation. During the forward scans from anodic to

cathodic potentials – corresponding to the lower branch of the current profile – amorphous WO₃ undergoes protonation, as H⁺ cations present in the acidic electrolyte are interstitially intercalated within its lattice and are electrically neutralized by a corresponding injection of electrons in the material. During the backward scans from cathodic to anodic potentials – corresponding to the upper branch of the current profile – said intercalated protons are extracted from material into the electrolytic solution and the neutralizing electrons are thence free to be injected back into the external circuit. During the cyclic voltammetry, this intercalation and de-intercalation process occurs reversibly and repeatedly, without causing any damage to the WO₃ film, thanks to its amorphous structure.[73] As shown by Zhao et al.,[100] electrochemical intercalation in WO₃ induces an increase in the majority carrier concentration, resulting in a higher conductivity and an improved electron charge transport. Kelvin probe force microscopy measurements (Figure 4.17b) show a reduction of the WO₃ work function as it undergoes the intercalation process. When protons get interstitially intercalated within the material lattice, electrons are injection in the conduction band to neutralize the additional positive charges and this strengthens the n-type nature of the material and shifts its work function towards the vacuum level. By keeping the sample at the maximum operative cathodic bias of 0 V$_{RHE}$ for several hours, the reversible intercalation process reaches saturation – all the available, low-energy interstitial sites filled with a proton – and the slow process of irreversible intercalation starts to display a substantial effect. Irreversible intercalation consists in the activation and occupation of deep, high-energy intercalated states, eventually leading to an effective reduction of the material, with the loss of an oxygen and the consequent formation of sub-band states. As per reversible intercalation, irreversible intercalation causes a further shift of the work function towards the vacuum level, increasing the barrier for electron injecting and thus

being ascribed as one of the reason behind the slow degradation of photocathode performances during prolonged measurements.

The photoelectrochemical performances of the hybrid organic photocathode device, fabricated with a 100-nm-thick amorphous WO_3 HSL, are probed through a chronoamperometry measurement (Figure 4.18a) with a fixed applied potential of 0.20 V_{RHE}, corresponding to the voltage of maximum power point for the device, as extrapolated from the linear sweep voltammetry curves. The resulting photocurrent is collected for a total of 10 uninterrupted hours, with the illumination being chopped for 2 minutes every hour in order to show the dark current of the device. The chronoamperometry shows that the dark current values are steady throughout the whole measurements and always in the negligible range of nanoamperes, proofing the absence of detrimental reduction processes not only for the amorphous WO_3 HSL – as previously shown by the cyclic voltammetry – but also for the complete photocathode architecture.
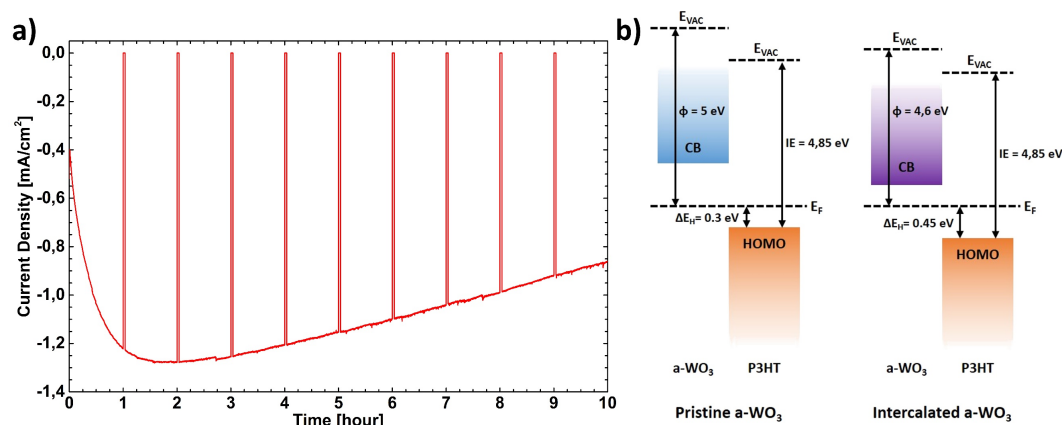
Figure 4.18 – Chronoamperometry measurement (a) of the hybrid organic photocathode fabricated with a 100-nm-thick HSL, performed under chopped AM1.5 solar light in a 0.1 M sulfuric acid solution at pH 1.37 with a fixed applied potential of 0.20 V_{RHE}. Energy level diagram (b) of the a-WO3/P3HT interface before (left) and after (right) the electrochemical intercalation process.

The temporal photocurrent profile follows a dynamic and non-monotonic trend, with a sharp rise from the starting value to the maximum occurring within the first two hours of operation, followed by a slow negative slope. A possible explanation

for this behavior is detailed in the following discussion. Before the measurement starts and any voltage is applied, the photocathode is at equilibrium in the electrolyte and is at its open circuit voltage. As reported by Greiner et al. analyzing the energetics at oxide/organic interfaces, the electron injection barrier ΔE_H at the HSL/BHJ interface is minimized when the work function of the semiconducting oxide is higher than the ionization energy of the facing polymer. Despite the required energetic inequality $\phi_{WO3} > IE_{P3HT}$ is satisfied (Figure 4.18b) and allows efficient charge injection through that interface, the density of majority carrier in pristine amorphous WO_3 is very low and thus fail to efficiently harvest the photogenerated holes coming from the P3HT. Consequently, in the first instants of the chronoamperometry, right after the device is polarized, a low photocurrent density of 0.4 mA·cm^{-2} is achieved, as the strong recombination of photogenerated charges within the BHJ layer dominates the device behavior. When the constant cathodic bias is applied to the photocathode, the amorphous WO_3 layer starts intercalating protons and continues until the process reaches saturation. Since the amorphous WO_3 layer is buried beneath the P3HT:PCBM bulk heterojunction and the platinum-decorated TiO_2 electron selective layer, proton diffusion towards the intercalation sites takes a longer time and saturation of the process is achieved after 2 hours of chronoamperometry, when the maximum photocurrent value of 1.28 mA·cm^{-2} is achieved. Concerning the energy level alignment, intercalated amorphous WO_3 has a work function lower than the ionization energy of P3HT (Figure 4.18b) and thus the electron injection barrier at the interface is higher compared to the situation with pristine, non-intercalated WO_3. However, this less favorable energetic alignment is compensated by the increased majority carrier density of the intercalated material, improving the pristine value by up to three orders of magnitude, approximately from 10^{18} cm^{-3} up to 10^{21} cm^{-3}. Previously reported by Fumagalli et al. for a similar architecture using another wide band-gap

n-type semiconductor such as MoO_3 for the role of HSL, during the intercalation process the Faradaic efficiency of the device is far below 100% since most of electron injected from the ITO contact into the WO_3 layer are used to neutralized the incoming hydrogen cations and thus the overall photocurrent yield of the device does not fully correspond to an effective production of hydrogen. When the intercalation process reaches saturation, the device resume its full Faradaic efficiency and can efficiently operate as a photocathode for hydrogen evolution. After the 2-hour-long activation period where the device intercalates and the photocurrent rises, the photocathodes operates uninterrupted under full Faradaic efficiency, showing a gradual performance degradation that results in a mere 30% loss of its maximum photocurrent value after 8 hours. The prolonged stability displayed by the device confirms the key importance of a durable HSL within the photocathode architecture. SEM cross-sectional images of the photocathode (Figure 4.15b) are collected before and after the 10-hour-long chronoamperometry and show no sign of degradation between the measured sample and the pristine one. As already suggested when discussing the intercalation process, the gradual degradation of the photocurrent is probably related to deep intercalation and reduction of the amorphous WO_3 film, that further increase the electron injection barrier, consequently hindering the overall performances. In a stacked layer architecture, every composing layer act as a series resistance when considering the charge transport, with its resistance value proportional to its thickness. The photocathode architecture employing a 100-nm-thick amorphous WO_3 film that has been described and characterized in the previous paragraphs is the final result of a parametric study on the HSL thickness aimed at optimizing the overall device in terms of operative parameters such as photocurrent density, onset potential and maximum power point.
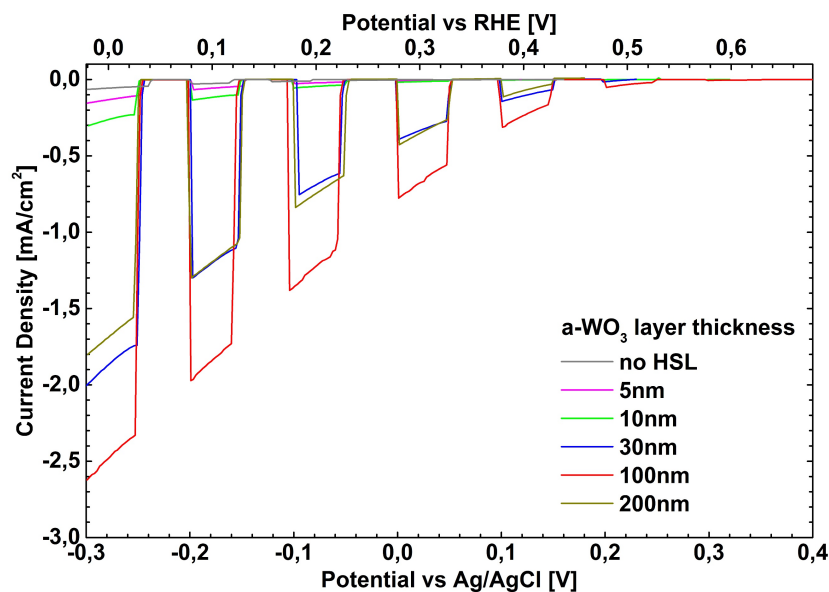
Figure 4.19 – LSV curves of hybrid organic photocathodes fabricated with a different thickness of the HSL, performed under chopped AM1.5 solar light in a 0.1 M sulfuric acid solution at pH 1.37.

To extract the electrochemical characteristics, linear sweep voltammetry measurements (Figure 4.19) are performed on photocathode fabricated with a different thickness of the HSL. The LSV curves of the devices show that both photocurrent density and onset potential increase with increasing thickness of the HSL, reaching a maximum for the photocathode with a 100-nm-thick layer of amorphous WO_3 that achieves a photocurrent density of 1.23 mA·cm^{-2} at the maximum power point voltage of 0.20 V_{RHE}. The ratiometric power-saved figure of merit for this best-performing device is equal to 0.25%. The values of J_{MPP}, V_{MPP} and ϕ_{saved} of all the photoanodes are presented tabulated for the sake of comparison (Table 4.1). The loss in performances for an HSL thickness above the optimal value of 100 nm is likely attributed the rapid increase in series resistance that affects the onset potential and shifts the photocurrent profile towards cathodic values. On the other hand, the performance losses that occurs for an HSL thickness below the optimal value of 100 nm are attributed to two different factors.

Thickness nm	$J_{@0V\ RHE}$ mA·cm^{-2}	V_{OP} V_{RHE}	J_{MPP} mA·cm^{-2}	V_{MPP} V_{RHE}	Φ_{saved} %
200	1.68	0.46	0.84	0.18	0.15
100	2.48	0.56	1.23	0.20	0.25
30	1.86	0.48	0.76	0.18	0.14
10	0.26	0.32	0.11	0.13	0.01
5	0.13	0.27	0.05	0.12	0.006
0 (no HSL)	0.06	0.19	0.02	0.11	0.002

Table 4.1 – Photoelectrochemical figures of merit of the hybrid organic photocathodes, extracted from the LSV curves of devices with a different thickness of the HSL. The table contains the photocurrent density at zero potential $J_{@0V\ RHE}$, the photocurrent onset potential V_{OP}, the photocurrent density at the maximum power point J_{MPP}, the maximum power point voltage V_{MPP} and the ratiometric power-saved figure of merit Φ_{saved}.

The first reason to explain the performance trend is related to the formation of a Schottky junction at the TCO/HSL interface, where a quasi-metallic material such as ITO is coupled with a n-type semiconductor such as amorphous WO$_3$. The depletion layer that occurs due to the Fermi level alignment and the consequent bending of the conduction band is completely located within the semiconductor film. Since the depleted region is void of majority carrier, this feature severely hinders electron charge transport when the depletion layer width is comparable with the thickness of the semiconductor. Using experimental values for the bilayer work functions and taking from literature the values of WO$_3$ carrier concentration and relative dielectric permittivity, the depletion layer width x_d is calculated with the following equation, derived from Poisson's equations for a metal/semiconductor junction under the full depletion approximation:

$$x_d = \sqrt{\frac{2\varepsilon_s(\varphi_m - \varphi_s)}{qN_d}}$$

where ε_s is the relative dielectric permittivity of the semiconductor, $\varphi_{m/s}$ is the work function of the metal and semiconductor respectively, q is the electron charge and N_d is the donor density of the semiconductor. The calculated value is approximately 10 nm and it is in good agreement with the experimental results, where the devices with an HSL thickness comparable to or lower than the estimated depletion layer width show poor photoelectrochemical performances, since the fully depleted hole selective layer cannot efficiently inject electrons in the adjacent P3HT layer (Figure 4.20). Accordingly, the device with a 30-nm-thick HSL delivers a significant amount of photocurrent as not all of the HSL thickness is depleted and a region with a high electron carrier density is still present at the polymer interface. Further increasing the HSL thickness results in a less prominent effect of the depletion layer on the device behavior and the performances peak for the device with a 100-nm-thick HSL.
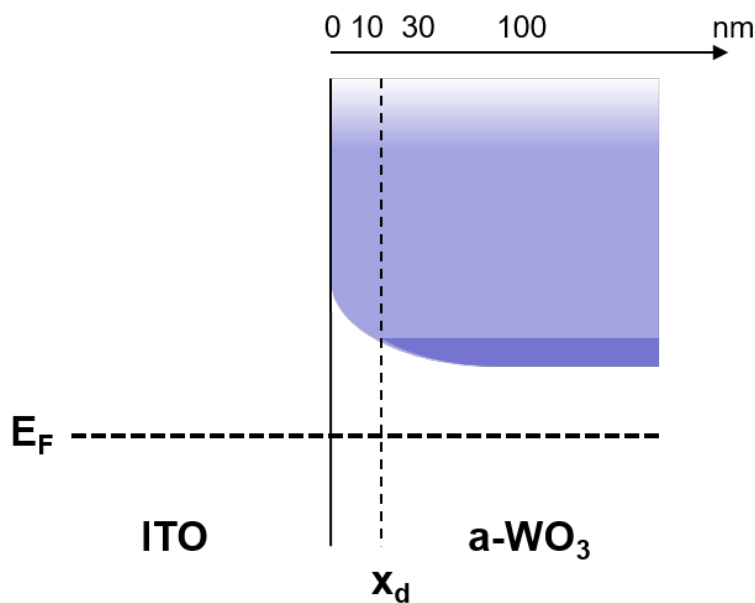
Figure 4.20 – Schematic representation of the depletion layer width at the ITO/a-WO₃ interface and the effect on the availability of majority carrier as a function of a-WO3 film thickness.

The second reason behind the performance loss for devices with thin HSL is speculated to be the presence of pinholes and defects in the amorphous WO₃ film

when its thickness goes below a critical value. When defects and pinholes are present, the polymer can percolate through the amorphous WO_3 film and reach the ITO contact beneath, thus locally preventing the HSL to perform its intended function. As widely reported in similar studies, removing any of the selective contacts from an organic photocathode architecture leads to a conspicuous loss in performances, orders of magnitude in terms of photocurrent and hundreds of millivolts in terms of onset potential. The conformal deposition of a continuous amorphous WO_3 film over the supporting ITO layer is confirmed by atomic force microscope images (Figure 4.21) that show the surface morphology signal of both pristine and deposited ITO surfaces, with different thicknesses of amorphous WO_3. From the morphology maps the substrate coverage is evident for the 100-nm- and 30-nm-thick film.
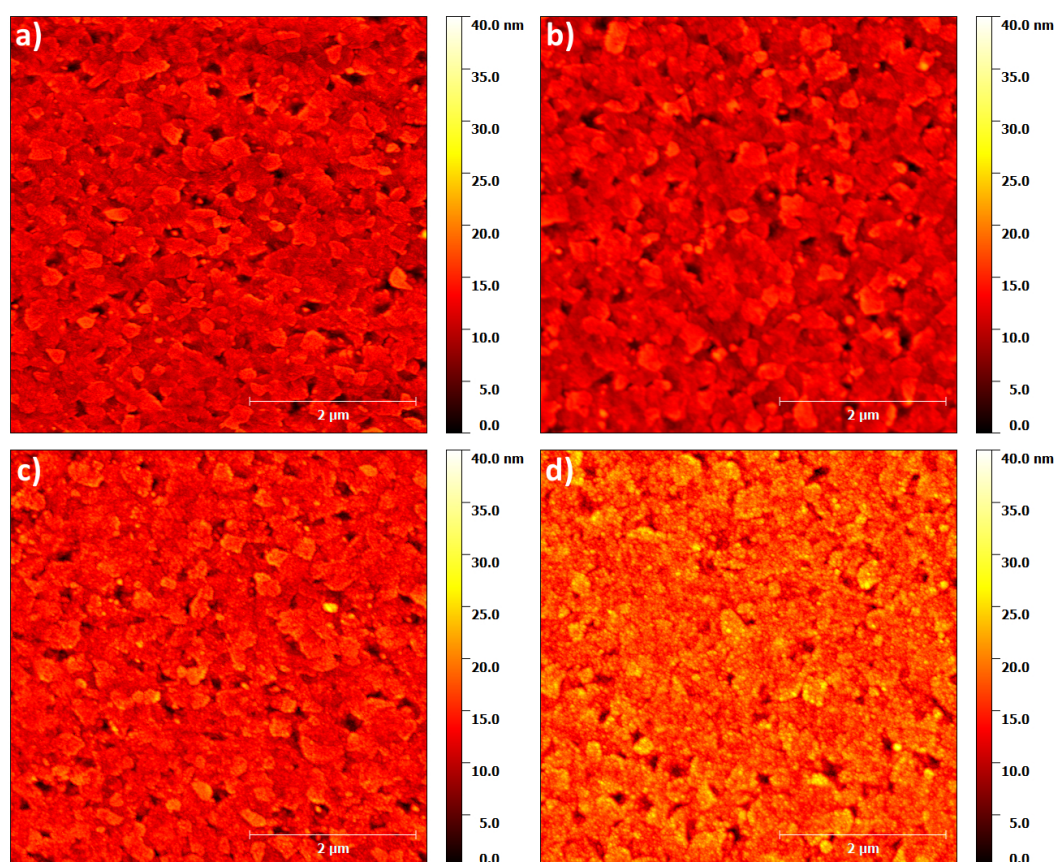
Figure 4.21 – Atomic force microscopy amplitude images showing surface morphology of bare ITO (a) and of ITO/a-WO3 samples with different HSL thickness: 5 nm (b), 30 nm (c) and 100 nm (d).

The 5-nm-thick film instead that only negligible changes in the surface morphology are induced by the HSL layer deposition when compared to the pristine ITO surface. As widely reported, thin films deposited via magnetron sputtering are not free from defects and pinholes, especially when the amorphous phase obtained at low temperatures does not undergo any thermal treatment after the deposition. Since no thermal annealing is performed after the deposition, the internal stresses and defects are not allowed to relax and reorganize. Consequently, amorphous films that do not undergo an annealing process need to exceed a certain thickness to drastically reduce the chance of pinholes cutting through their entire thickness. As the ITO supporting layer has an average roughness of 3 nm, amorphous WO_3 films with a comparable thickness have a high chance to suffer from non-conformal coating and thus present the issue of polymer short-circuiting with the ITO. These observations, supported by the discussion concerning the depletion layer, corroborate the poor performance of photocathodes fabricated with an HSL thickness below the optimal value of 100 nm.

4.2.3 Conclusions

In summary, this study demonstrates that proper material selection in terms of both photoactive materials (conjugated organic polymers as P3HT:PCBM) and contact layers (metal oxides as WO_3 and TiO_2) allows the fabrication of electrochemically stable hybrid organic photocathodes. The proposed architecture is capable of operating PEC hydrogen evolution under full Faradaic efficiency for several hours, suffering a performance loss of only 30% after 8 hours of uninterrupted operation. This result currently represents the state-of-the-art in terms of stability for unprotected hybrid organic photocathodes for PEC hydrogen evolution. The device exhibits a maximum photocurrent of 2.48 mA·cm^{-2} at 0 V_{RHE}

and an onset potential as high as 0.56 V_{RHE}, values in line with the best-performing organic photocathodes recently reported in literature. Increased devices stability is obtained exploiting the properties of amorphous WO_3 – a wide band-gap n-type semiconductor stable in a wide range of electrochemical environments – in order to obtain an efficient and resilient HSL for the photocathode architecture.

Chapter 5: Outlooks

Photoanodes based on bare WO_3 have been widely and intensively investigated throughout the last decade. Considering the maximum theoretical conversion efficiency around 4.8% – dictated by the material intrinsic properties – for a single junction WO_3 photoanode under standard working conditions, the results present in literature have come close to the material limit in its bare state. The major limiting factors are the wide optical band-gap of 2.6 eV and the incorrect position of the conduction band, more positive than the hydrogen evolution potential. In order to solve these problems, several studies have focused on the band-gap engineering of WO_3 through doping.[101–103] The idea behind doping is to modify the orbital configuration of the starting material and thus the resulting optoelectronic structure. The limit of this technique are the possible defects introduced within the pristine crystalline structure that results in a degradation of the charge transport properties due to the higher recombination rates occurring at defects. To improve the performances of photoelectrochemical photoanodes based on WO_3, composite materials have been used, developing heterojunctions with improved optical absorption and charge extraction properties. Furthermore, catalysts for the oxygen evolution reaction – from the traditional platinum and iridium oxide to the recent phosphorus- and cobalt-based materials – are employed to improve the extraction Currently, the most promising architecture for photoelectrochemical water-splitting photoanodes is the heterostructure that employs bismuth vanadate ($BiVO_4$) combined with tungsten trioxide (WO_3).[104–110] Concerning the record device, Abdi et al.[110] report a photoanode made with gradient doped $W:BiVO_4$ with Co-Pi as the oxygen evolution catalyst, which achieves carrier separation efficiencies above 80%, a solar-to-hydrogen efficiency

around 5% when coupled in tandem with a double-junction amorphous silicon solar cell and displays a decent photoelectrochemical stability under working conditions. The W:BiVO$_4$ heterostructure is fabricated using the sol-gel method and is formed by a mesoporous aggregate of nanoparticles. The quasi-1D hyperbranched WO$_3$ nanostructures reported in this work, fabricated using pulsed laser deposition under optimized conditions, outperform even the sol-gel stat-of-the-art devices in terms of charge transport properties and electrochemical performances in the low voltage range.[47] A promising future outlook for the reported work is to develop an hyperbranched nanostructure made of W:BiVO4, in order to obtain the enhanced performances of the heterostructure with less applied bias and thus improve the working point conditions of the eventual tandem devices. Optimization of catalytic material that do not employ noble metals[111–114] is also of prime importance in order to improving the conversion efficiencies without increasing the production costs.

Concerning the photocathode architectures and the field of hybrid organic photoelectrochemical devices for water-splitting, there are numerous possible research outlooks. Amorphous WO$_3$ has confirmed its chemical stability, acting as a durable hole selective layer in the proposed architecture. The overall device performances strongly depend on the electronic properties of the comprising materials, from the inorganic selective layers to the organic bulk heterojunction. Concerning the material for the hole selective layer, the knowledge acquired from this work[72] and the ones before it[68,71] has led to the preliminary development of a dual-material HSL, comprising a driving CuI layer deposited on the TCO substrate and a protective a-WO$_3$ layer deposited on top. The concept behind this preliminary work is to exploit the favorable energetic alignment of CuI while preserving its functionality with a thin a-WO$_3$ protective layer that prevents CuI dissolution without compromising the charge extraction efficiency. Moving

upward on the device architecture, an important optimization step involves the organic bulk heterojunction. New materials – both for the polymer donor and the acceptor – and combinations can be exploited in order to improve the absorption range of the photoactive material and increase the charge separation within the organic blend. Following the recent trends in the leading field of OPV provides for interesting research outlooks that might be adequately ported into HOPEC systems, like the recent development of non-fullerene acceptors.[115–117] Lastly, following the same discussion made for photoanodes, the development and optimization of cheap, noble-metal free catalytic material for hydrogen evolution is of prime importance in the path to reduce the device fabrication cost. Promising routes involves the study of inorganic catalytic complexes[118,119] and molecular catalysts.[120,121]

List of Figures

Bibliography

(1)   Bockris, J. O.; Reddy, A. K. N. *Modern Electrochemistry: an Introduction to an Interdisciplinary Area*; 1970.

(2)   Ogden, J. M. *Annu. Rev. Energy Environ.* **1999**, *24* (1), 227–279.

(3)   Fujishima, A.; Honda, K. *Nature* **1972**, *238* (5358), 37–38.

(4)   Reza Gholipour, M.; Dinh, C.-T.; Béland, F.; Do, T.-O. *Nanoscale* **2015**, *7* (18), 8187–8208.

(5)   Pinaud, B. a.; Benck, J. D.; Seitz, L. C.; Forman, A. J.; Chen, Z.; Deutsch, T. G.; James, B. D.; Baum, K. N.; Baum, G. N.; Ardo, S.; Wang, H.; Miller, E.; Jaramillo, T. F. *Energy Environ. Sci.* **2013**, *6* (7), 1983.

(6)   Prévot, M. S.; Sivula, K. *J. Phys. Chem. C* **2013**, *117* (35), 17879–17893.

(7)   Salje, E.; Viswanathan, K. *Acta Crystallogr. Sect. A* **1975**, *31* (3), 356–359.

(8)   Salje, E. K. H.; Rehmann, S.; Pobell, F.; Morris, D.; Knight, K. S.; Herrmannsdörfer, T.; Dove, M. T. *J. Phys. Condens. Matter* **1997**, *9* (31), 6563–6577.

(9)   Depero, L. E.; Groppelli, S.; Natali-Sora, I.; Sangaletti, L.; Sberveglieri, G.; Tondello, E. *J. Solid State Chem.* **1996**, *121* (2), 379–387.

(10)   Miller, U. *Inorganic Structural Chemistry*; John Wiley & Sons, Ltd: Chichester, UK, 2006.

(11)   Liu, X.; Wang, F.; Wang, Q. *Phys. Chem. Chem. Phys.* **2012**, *14* (22), 7894–7911.

(12)   Butler, M. A. *J. Appl. Phys.* **1977**, *48* (5), 1914–1920.

(13)   Desilvestro, J.; Grätzel, M. *J. Electroanal. Chem. Interfacial Electrochem.* **1987**, *238* (1–2), 129–150.

(14)   Enesca, A.; Duta, A.; Schoonman, J. *Thin Solid Films* **2007**, *515* (16), 6371–6374.

(15)   Patil, P. S.; Patil, P. R. *Bull. Mater. Sci.* **1996**, *19* (4), 651–656.

(16)   Rao, P. M.; Cho, I. S.; Zheng, X. *Proc. Combust. Inst.* **2013**, *34* (2), 2187–2195.

(17)   Sun, Y.; Murphy, C. J.; Reyes-Gil, K. R.; Reyes-Garcia, E. A.; Thornton, J. M.; Morris, N. A.; Raftery, D. *Int. J. Hydrogen Energy* **2009**, *34* (20), 8476–8484.

(18)   Bignozzi, C. A.; Caramori, S.; Cristino, V.; Argazzi, R.; Meda, L.; Tacca, A.

Chem. Soc. Rev. **2013**, *42* (6), 2228–2246.

(19)   Brillet, J.; Yum, J.; Cornuz, M.; Hisatomi, T.; Solarska, R.; Augustynski, J.; Graetzel, M.; Sivula, K. *Nat. Photonics* **2012**, *6* (12), 824–828.

(20)   Kim, J. K.; Shin, K.; Cho, S. M.; Lee, T.-W.; Park, J. H. *Energy Environ. Sci.* **2011**, *4* (4), 1465.

(21)   Li, W.; Li, J.; Wang, X.; Ma, J.; Chen, Q. *Int. J. Hydrogen Energy* **2010**, *35* (24), 13137–13145.

(22)   Radecka, M.; Sobas, P.; Wierzbicka, M.; Rekas, M. *Phys. B Condens. Matter* **2005**, *364* (1–4), 85–92.

(23)   Santato, C.; Ulmann, M.; Augustynski, J. *J. Phys. Chem. B* **2001**, *105* (5), 936–940.

(24)   Shi, X.; Zhang, K.; Shin, K.; Ma, M.; Kwon, J.; Choi, I. T.; Kim, J. K.; Kim, H. K.; Wang, D. H.; Park, J. H. *Nano Energy* **2015**, *13*, 182–191.

(25)   Solarska, R.; Alexander, B. D.; Augustynski, J. *Comptes Rendus Chim.* **2006**, *9* (2), 301–306.

(26)   Solarska, R.; Jurczakowski, R.; Augustynski, J. *Nanoscale* **2012**, *4* (5), 1553.

(27)   Wang, H.; Lindgren, T.; He, J.; Hagfeldt, A.; Lindquist, S. *J. Phys. Chem. B* **2000**, *104* (24), 5686–5696.

(28)   Amano, F.; Tian, M.; Wu, G.; Ohtani, B.; Chen, A. *ACS Appl. Mater. Interfaces* **2011**, *3* (10), 4047–4052.

(29)   Biswas, S. K.; Baeg, J.-O. *Int. J. Hydrogen Energy* **2013**, *38* (8), 3177–3188.

(30)   Hong, S. J.; Jun, H.; Borse, P. H.; Lee, J. S. *Int. J. Hydrogen Energy* **2009**, *34* (8), 3234–3242.

(31)   Qin, D.-D.; Tao, C.-L.; Friesen, S. a.; Wang, T.-H.; Varghese, O. K.; Bao, N.-Z.; Yang, Z.-Y.; Mallouk, T. E.; Grimes, C. a. *Chem. Commun.* **2012**, *48* (5), 729–731.

(32)   Su, J.; Feng, X.; Sloppy, J. D.; Guo, L.; Grimes, C. a. *Nano Lett.* **2011**, *11* (1), 203–208.

(33)   Wang, G.; Ling, Y.; Wang, H.; Yang, X.; Wang, C.; Zhang, J. Z.; Li, Y. *Energy Environ. Sci.* **2012**, *5* (3), 6180.

(34)   Cristino, V.; Caramori, S.; Argazzi, R.; Meda, L.; Marra, G. L.; Bignozzi, C. A. *Langmuir ACS J. Surfaces Colloids* **2011**, *27* (11), 7276–7284.

(35)   de Tacconi, N. R.; Chenthamarakshan, C. R.; Yogeeswaran, G.; Watcharenwong, A.; de Zoysa, R. S.; Basit, N. A.; Rajeshwar, K. *J. Phys. Chem. B* **2006**, *110* (50), 25347–25355.

(36)   Guo, Y.; Quan, X.; Lu, N. *Environ. Sci. Technol.* **2007**, *41* (12), 4422–4427.

(37)   Ng, C.; Ng, Y.; Iwase, A.; Amal, R. *ACS Appl. Mater. Interfaces* **2013**, *5* (11), 5269–5275.

(38)   Tacca, A.; Meda, L.; Marra, G.; Savoini, A.; Caramori, S.; Cristino, V.; Bignozzi, C. A.; Gonzalez Pedro, V.; Boix, P. P.; Gimenez, S.; Bisquert, J. *Chemphyschem* **2012**, *13* (12), 3025–3034.

(39)   Kwong, W. L.; Nakaruk, A.; Koshy, P.; Sorrell, C. C. *Thin Solid Films* **2013**, *544*, 191–196.

(40)   Mi, Q.; Coridan, R. H.; Brunschwig, B. S.; Gray, H. B.; Lewis, N. S. *Energy Environ. Sci.* **2013**, *6* (9), 2646.

(41)   Mi, Q.; Zhanaidarova, A.; Brunschwig, B. S.; Gray, H. B.; Lewis, N. S. *Energy Environ. Sci.* **2012**, *5* (2), 5694.

(42)   Chakrapani, V.; Thangala, J.; Sunkara, M. K. *Int. J. Hydrogen Energy* **2009**, *34* (22), 9050–9059.

(43)   Liu, R.; Lin, Y.; Chou, L.-Y.; Sheehan, S. W.; He, W.; Zhang, F.; Hou, H. J. M.; Wang, D. *Angew. Chemie Int. Ed.* **2011**, *50* (2), 499–502.

(44)   Sivula, K.; Formal, F. Le; Grätzel, M. *Chem. Mater.* **2009**, *21* (13), 2862–2867.

(45)   Zhang, X.; Lu, X.; Shen, Y.; Han, J.; Yuan, L.; Gong, L.; Xu, Z.; Bai, X.; Wei, M.; Tong, Y.; Gao, Y.; Chen, J.; Zhou, J.; Wang, Z. L. *Chem. Commun. (Camb).* **2011**, *47* (20), 5804–5806.

(46)   Baek, Y.; Song, Y.; Yong, K. *Adv. Mater.* **2006**, *18* (23), 3105–3110.

(47)   Balandeh, M.; Mezzetti, A.; Tacca, A.; Leonardi, S.; Marra, G.; Divitini, G.; Ducati, C.; Meda, L.; Di Fonzo, F. *J. Mater. Chem. A* **2015**, *3* (11), 6110–6117.

(48)   Marsen, B.; Miller, E. L.; Paluselli, D.; Rocheleau, R. E. *Int. J. Hydrogen Energy* **2007**, *32* (15), 3110–3115.

(49)   Shin, S.; Han, H. S.; Kim, J. S.; Park, I. J.; Lee, M. H.; Hong, K. S.; Cho, I. S. *J. Mater. Chem. A* **2015**, *3* (24), 12920–12926.

(50)   Abdou, M. S. a.; Holdcroft, S. *Macromolecules* **1993**, *26* (11), 2954–2962.

(51)   Lanzarini, E.; Antognazza, M. R.; Biso, M.; Ansaldo, A.; Laudato, L.; Bruno, P.; Metrangolo, P.; Resnati, G.; Ricci, D.; Lanzani, G. *J. Phys. Chem. C* **2012**, *116* (20), 10944–10949.

(52)   Scharber, M. C.; Mühlbacher, D.; Koppe, M.; Denk, P.; Waldauf, C.; Heeger, A. J.; Brabec, C. J. *Adv. Mater.* **2006**, *18* (6), 789–794.

(53)   Chen, S. N.; Heeger, A. J.; Kiss, Z.; MacDiarmid, A. G.; Gau, S. C.; Peebles, D. L. *Appl. Phys. Lett.* **1980**, *36* (1), 96–98.

(54)   Glenis, S.; Tourillon, G.; Garnier, F. *Thin Solid Films* **1984**, *122* (1), 9–17.

(55) Yanagida, S.; Kabumoto, A.; Mizumoto, K.; Pac, C.; Yoshino, K. *J. Chem. Soc. Chem. Commun.* **1985**, No. 8, 474.

(56) Kaneko, M.; Okuzumi, K.; Yamada, A. *J. Electroanal. Chem. Interfacial Electrochem.* **1985**, *183* (1–2), 407–410.

(57) McCullough, R. D.; Lowe, R. D. *J. Chem. Soc. Chem. Commun.* **1992**, No. 1, 70.

(58) McCullough, R. D.; Lowe, R. D.; Jayaraman, M.; Ewbank, P. C.; Anderson, D. L.; Tristram-Nagle, S. *Synth. Met.* **1993**, *55* (2–3), 1198–1203.

(59) El-Rashiedy, O. a; Holdcroft, S. *J. Phys. Chem.* **1996**, *100* (13), 5481–5484.

(60) Abe, T.; Tobinai, S.; Taira, N.; Chiba, J.; Itoh, T.; Nagai, K. *J. Phys. Chem. C* **2011**, *115* (15), 7701–7705.

(61) Abe, T.; Chiba, J.; Ishidoya, M.; Nagai, K. *RSC Adv.* **2012**, *2* (21), 7992.

(62) Suppes, G. Poly 3-Hexylthiophene as a Photocathode for Solar Water Splitting, 2015.

(63) Suppes, G. M.; Fortin, P. J.; Holdcroft, S. *J. Electrochem. Soc.* **2015**, *162* (8), H551–H556.

(64) Bourgeteau, T.; Tondelier, D.; Geffroy, B.; Brisse, R.; Laberty-Robert, C.; Campidelli, S.; de Bettignies, R.; Artero, V.; Palacin, S.; Jousselme, B. *Energy. Sustain. Soc.* **2013**, *6* (9), 2706–2713.

(65) Guerrero, A.; Haro, M.; Bellani, S.; Antognazza, M. R.; Meda, L.; Gimenez, S.; Bisquert, J. *Energy Environ. Sci.* **2014**, *7* (11), 3666–3673.

(66) Haro, M.; Solis, C.; Molina, G.; Otero, L.; Bisquert, J.; Gimenez, S.; Guerrero, A. *J. Phys. Chem. C* **2015**, *119* (12), 6488–6494.

(67) Bourgeteau, T.; Tondelier, D.; Geffroy, B.; Brisse, R.; Cornut, R.; Artero, V.; Jousselme, B. *ACS Appl. Mater. Interfaces* **2015**, *7* (30), 16395–16403.

(68) Fumagalli, F.; Bellani, S.; Schreier, M.; Leonardi, S.; Rojas, H. C.; Ghadirzadeh, A.; Tullii, G.; Savoini, A.; Marra, G.; Meda, L.; Grätzel, M.; Lanzani, G.; Mayer, M. T.; Antognazza, M. R.; Di Fonzo, F. *J. Mater. Chem. A* **2016**, *4* (6), 2178–2187.

(69) Bourgeteau, T.; Tondelier, D.; Geffroy, B.; Brisse, R.; Campidelli, S.; Cornut, R.; Jousselme, B. *J. Mater. Chem. A* **2016**, *4* (13), 4831–4839.

(70) Morozan, A.; Bourgeteau, T.; Tondelier, D.; Geffroy, B.; Jousselme, B.; Artero, V. *Nanotechnology* **2016**, *27* (35), 355401.

(71) Rojas, H. H. C.; Bellani, S.; Fumagalli, F.; Tullii, G.; Leonardi, S.; Mayer, M. T.; Schreier, M.; Grätzel, M.; Lanzani, G.; Di Fonzo, F.; Antognazza, M. R. *Energy Environ. Sci.* **2016**, *9*, 2–4.

(72) Mezzetti, A.; Fumagalli, F.; Alfano, A.; Iadicicco, D.; Antognazza, M. R.; Di

Fonzo, F. *Faraday Discuss.* **2016**, *157* (207890), 243.

(73) Giannuzzi, R.; Balandeh, M.; Mezzetti, A.; Meda, L.; Pattathil, P.; Gigli, G.; Di Fonzo, F.; Manca, M. *Adv. Opt. Mater.* **2015**, n/a-n/a.

(74) Chen, Z.; Dinh, H. N.; Miller, E. *Photoelectrochemical Water Splitting - Standards, Experimental Methods, and Protocols*; 2013.

(75) Bolton, J. R.; Strickler, S. J.; Connolly, J. S. *Nature* **1985**, *316* (6028), 495–500.

(76) Coridan, R. H.; Nielander, A. C.; Francis, S. a; McDowell, M. T.; Dix, V.; Chatman, S. M.; Lewis, N. S. *Energy Environ. Sci.* **2015**, *8* (10), 2886–2901.

(77) Passoni, L.; Criante, L.; Fumagalli, F.; Scotognella, F.; Lanzani, G.; Fonzo, F. Di; Science, N.; Polimi, T.; Italiano, I.; Pascoli, V. G.; Fisica, D. *ACS Nano* **2014**, No. 12, 12167–12174.

(78) Passoni, L.; Ghods, F.; Docampo, P. *ACS Nano* **2013**, No. 11, 10023–10031.

(79) Sauvage, F.; Di Fonzo, F.; Li Bassi, a; Casari, C. S.; Russo, V.; Divitini, G.; Ducati, C.; Bottani, C. E.; Comte, P.; Graetzel, M. *Nano Lett.* **2010**, *10* (7), 2562–2567.

(80) Di Fonzo, F.; Casari, C. S.; Russo, V.; Brunella, M. F.; Li Bassi, a; Bottani, C. E. *Nanotechnology* **2009**, *20* (1), 15604.

(81) Valentin, C. Di; Pacchioni, G.; Selloni, A. *Chem. Mater.* **2005**, No. d, 6656–6665.

(82) Di Fonzo, F.; Tonini, D.; Li Bassi, A.; Casari, C. S.; Beghi, M. G.; Bottani, C. E.; Gastaldi, D.; Vena, P.; Contro, R. *Appl. Phys. A* **2008**, *93* (3), 765–769.

(83) Mora-Seró, I.; Garcia-Belmonte, G.; Boix, P. P.; Vázquez, M. a.; Bisquert, J. *Energy Environ. Sci.* **2009**, *2* (6), 678.

(84) Martinson, A. B. F.; Góes, M. S.; Fabregat-Santiago, F.; Bisquert, J.; Pellin, M. J.; Hupp, J. T. *J. Phys. Chem. A* **2009**, *113* (16), 4015–4021.

(85) Gimenez, S.; Dunn, H. K.; Rodenas, P.; Fabregat-Santiago, F.; Miralles, S. G.; Barea, E. M.; Trevisan, R.; Guerrero, A.; Bisquert, J. *J. Electroanal. Chem.* **2012**, *668*, 119–125.

(86) Bisquert, J.; Garcia-Belmonte, G.; Fabregat-Santiago, F.; Ferriols, N. S.; Bogdanoff, P.; Pereira, E. C. *J. Phys. Chem. B* **2000**, *104* (10), 2287–2298.

(87) Bisquert, J. *J. Electroanal. Chem.* **2010**, *646* (1–2), 43–51.

(88) Bertoluzzi, L.; Bisquert, J. *J. Phys. Chem. Lett.* **2012**, *3* (17), 2517–2522.

(89) Bisquert, J.; Fabregat-Santiago, F.; Mora-Seró, I.; Garcia-Belmonte, G.; Giménez, S. *J. Phys. Chem. C* **2009**, *113*, 17278–17290.

(90) Bisquert, J. *Phys. Chem. Chem. Phys.* **2003**, *5* (24), 5360.

(91)   Bisquert, J. *J. Phys. Chem. B* **2002**, *106* (2), 325–333.

(92)   Valdés, A.; Kroes, G.-J. *J. Chem. Phys.* **2009**, *130* (11), 114701.

(93)   Greiner, M. T.; Helander, M. G.; Tang, W.-M.; Wang, Z.-B.; Qiu, J.; Lu, Z.-H. *Nat. Mater.* **2012**, *11* (1), 76–81.

(94)   Ratcliff, E. L.; Zacher, B.; Armstrong, N. R. *J. Phys. Chem. Lett.* **2011**, *2*, 1337–1350.

(95)   Yip, H.-L.; Jen, A. K.-Y. *Energy Environ. Sci.* **2012**, *5* (3), 5994.

(96)   Paracchino, A.; Laporte, V.; Sivula, K.; Grätzel, M.; Thimsen, E. *Nat. Mater.* **2011**, *10* (6), 456–461.

(97)   Paracchino, A.; Mathews, N.; Hisatomi, T.; Stefik, M.; Tilley, S. D.; Grätzel, M. *Energy Environ. Sci.* **2012**, *5* (9), 8673.

(98)   Fumagalli, F.; Martí-Rujas, J.; Di Fonzo, F. *Thin Solid Films* **2014**, *569* (C), 44–51.

(99)   Luzio, A.; Ferré, F. G.; Fonzo, F. Di; Caironi, M. *Adv. Funct. Mater.* **2014**, *24* (12), 1790–1798.

(100) Zhao, J.; Olide, E.; Osterloh, F. E. *J. Electrochem. Soc.* **2014**, *162* (1), H65–H71.

(101) Hameed, a.; Gondal, M. a.; Yamani, Z. H. *Catal. Commun.* **2004**, *5* (11), 715–719.

(102) Mi, Q.; Ping, Y.; Li, Y.; Cao, B.; Brunschwig, B. S.; Khalifah, P. G.; Galli, G. a; Gray, H. B.; Lewis, N. S. *J. Am. Chem. Soc.* **2012**, *134* (44), 18318–18324.

(103) Wang, F.; Valentin, C. Di; Pacchioni, G.; Di Valentin, C.; Pacchioni, G. *J. Phys. Chem. C* **2012**, *116*, 8901–8909.

(104) Kim, T. W.; Choi, K.-S. *Science (80-.).* **2014**, *343* (6174), 990–994.

(105) Saito, R.; Miseki, Y.; Sayama, K. *Chem. Commun.* **2012**, *48* (32), 3833.

(106) Pilli, S. K.; Janarthanan, R.; Deutsch, T. G.; Furtak, T. E.; Brown, L. D.; Turner, J. a; Herring, A. M. *Phys. Chem. Chem. Phys.* **2013**, *15* (35), 14723–14728.

(107) Su, J.; Guo, L.; Bao, N.; Grimes, C. A. *Nano Lett.* **2011**, *11* (5), 1928–1933.

(108) Rao, P. M.; Cai, L.; Liu, C.; Cho, I. S.; Lee, C. H.; Weisse, J. M.; Yang, P.; Zheng, X. *Nano Lett.* **2014**, *14* (2), 1099–1105.

(109) Hong, S. J.; Lee, S.; Jang, J. S.; Lee, J. S. *Energy Environ. Sci.* **2011**, *4* (5), 1781.

(110) Abdi, F. F.; Han, L.; Smets, A. H. M.; Zeman, M.; Dam, B.; van de Krol, R. *Nat. Commun.* **2013**, *4*, 2195.

(111) Lhermitte, C. R.; Garret Verwer, J.; Bartlett, B. M. *J. Mater. Chem. A* **2016**, *4* (8), 2960–2968.

(112) Seabold, J.; Choi, K. *Chem. Mater.* **2011**, 1105–1112.

(113) Zou, X.; Zhang, Y. *Chem. Soc. Rev.* **2015**, *44* (15), 5148–5180.

(114) Muresan, N. M.; Willkomm, J.; Mersch, D.; Vaynzof, Y.; Reisner, E. *Angew. Chemie - Int. Ed.* **2012**, *51* (51), 12749–12753.

(115) Holliday, S.; Ashraf, R. S.; Wadsworth, A.; Baran, D.; Yousaf, S. A.; Nielsen, C. B.; Tan, C.-H.; Dimitrov, S. D.; Shang, Z.; Gasparini, N.; Alamoudi, M.; Laquai, F.; Brabec, C. J.; Salleo, A.; Durrant, J. R.; McCulloch, I. *Nat. Commun.* **2016**, *7*, 11585.

(116) Nielsen, C. B.; Holliday, S.; Chen, H.-Y.; Cryer, S. J.; McCulloch, I. *Acc. Chem. Res.* **2015**, *48* (11), 2803–2812.

(117) Zhan, C.; Zhang, X.; Yao, J. *RSC Adv.* **2015**, *5* (113), 93002–93026.

(118) Seh, Z. W.; Fredrickson, K. D.; Anasori, B.; Kibsgaard, J.; Strickler, A. L.; Lukatskaya, M. R.; Gogotsi, Y.; Jaramillo, T. F.; Vojvodic, A. *ACS Energy Lett.* **2016**, *1*, 589–594.

(119) Britto, R. J.; Benck, J. D.; Young, J. L.; Hahn, C.; Deutsch, T. G.; Jaramillo, T. F. *J. Phys. Chem. Lett.* **2016**, *7* (11), 2044–2049.

(120) Rosser, T. E.; Gross, M. A.; Lai, Y.-H.; Reisner, E. *Chem. Sci.* **2016**, *7*, 4024–4035.

(121) Lee, C.-Y.; Park, H. S.; Fontecilla-Camps, J. C.; Reisner, E. *Angew. Chemie* **2016**, 1–5.